

**MODELING AND CONTROLLING THERMOCHEMICAL
NANOLITHOGRAPHY**

A Thesis
Presented to
The Academic Faculty

by

Keith M. Carroll

In Partial Fulfillment
of the Requirements for the Degree
Doctor of Philosophy in the
School of Physics

Georgia Institute of Technology
December 2013

MODELING AND CONTROLLING THERMOCHEMICAL NANOLITHOGRAPHY

Approved by:

Dr. Jennifer E. Curtis, Advisor
School of Physics
Georgia Institute of Technology

Dr. Lawrence A. Bottomley
School of Chemistry and Biochemistry
Georgia Institute of Technology

Dr. Elisa Riedo
School of Physics
Georgia Institute of Technology

Dr. Harold D. Kim
School of Physics
Georgia Institute of Technology

Dr. Seth R. Marder
School of Chemistry and Biochemistry
Georgia Institute of Technology

Date Approved: [Month dd, yyyy]

To my wife and family

ACKNOWLEDGEMENTS

I want to start out by thanking my wife and my family. Marrying my wife is the best decision I ever made, and this is as much my work as it is hers. She put up with a lot of long nights only to prove how supportive and loving she is. She is my best friend, and I cannot even begin to imagine how my life would be without her. Thank you so much Jess. I want to thank Mom and Dad; without their guidance and support I would not be where I am today. They have taught more than I can ever repay and I am eternally grateful. Thank you Mom and Dad. I want to thank Toni and Jerry for welcoming me into their family. I will never forget how wonderful and extraordinarily supportive they have been. Thank you Toni and Jerry. I want to thank all my siblings. They were inspirations even when they did not know it. They taught me to reach for the highest goals but kept me grounded the entire time. They taught me what family means, and have blessed me with three wonderful nieces who always make me smile. Kevin, Kelly, Dave, Nichol, Jenny, Ryan, Juliana, Annie, thank you all. I want to thank the rest of my family as well; they have always been supportive. Thank you.

I want to thank my adviser, Professor Jennifer E. Curtis. Without her advice, I would not be half the researcher I am today. She taught me how to think about science but not forget the perspective of everything else. Thank you Jennifer. I also want to thank my fellow lab members (past and present): Vamsi, Louis, Mauricio, Dan, Patrick, Maitri, Karl, and Wenbin; without them, I do not know if I would have survived. I also want to thank our former Post-Doc Jan; his successes were always an encouragement.

I want to thank Professor Elisa Riedo and Professor Seth R. Marder. They were always happy and willing to discuss problems and possible solutions. They were an incredible source of advice, and I consider myself lucky to have worked so closely with them. Thank you both so much. I also want to thank my other committee members, Professor Lawrence Bottomley and Professor Harold Kim. Your work and successes are an inspiration. Thank you.

I want to thank Anthony, without whom much of this work would not have happened. He is a good friend who, as I have said before, is as smart as his niece. Thank you.

I also want to thank everyone from the Riedo lab (past and present); they have been an inspiration. Debin, Deborah, Suenne, Lucy, Edoardo, Alex, and Gao, thank you all.

Finally, I want to thank all my friends, who have been supportive. They have taught me what it means to be a loyal friend. Thank you so much.

TABLE OF CONTENTS

| Page | | |
|------|--|-------|
| | ACKNOWLEDGEMENTS | iv |
| | LIST OF TABLES | x |
| | LIST OF FIGURES | xi |
| | SUMMARY | xviii |
| | <u>CHAPTER</u> | |
| 1 | INTRODUCTION | 1 |
| | 1.1 Introduction | 1 |
| | 1.2 Lithographic Technique | 2 |
| | 1.2.1 MicroContact Printing | 2 |
| | 1.2.2 Light Based Lithographies | 4 |
| | 1.2.3 Micro-Fluidics | 5 |
| | 1.2.4 Electron Beam Lithography | 6 |
| | 1.2.5 Nano-shaving/Nano-grafting | 7 |
| | 1.2.6 Electric and Conductive SPM Techniques | 8 |
| | 1.2.7 Dip-Pen Nanolithography | 9 |
| | 1.2.8 Thermal/Thermomechanical Lithography | 10 |
| | 1.2.9 Thermal Dip-Pen Nanolithography | 11 |
| | 1.2.10 ThermoChemical NanoLithography | 12 |
| | 1.3 Chemical and Topographic Gradients | 15 |
| | 1.3.1 ThermoChemical NanoLithography: Evidence of Chemical Gradients | 15 |
| 2 | CHEMICAL KINETICS MODEL | 19 |

| | | |
|-------|--|----|
| 2.1 | Introduction/Motivation | 19 |
| 2.2 | Chemical Kinetics Model | 20 |
| 2.2.1 | Static Tip Solution | 22 |
| | Time Variation | 23 |
| | Temperature Variation | 24 |
| | Decay Length | 26 |
| 2.2.2 | Effects of Multiple Points | 27 |
| 2.2.3 | Extension to a Moving Tip | 29 |
| | Effects of Speed | 31 |
| 2.3 | Expanding to Surface and 3-D | 33 |
| 2.4 | Discussion of the Assumed Temperature Profile | 35 |
| 2.5 | Final Word | 36 |
| 3 | EXPERIMENTAL MODELING OF SURFACE REACTIONS WITH TCNL | 37 |
| 3.1 | Introduction | 37 |
| 3.2 | Review of Thermal Cantilevers | 38 |
| 3.2.1 | Thermal Cantilevers: Fabrication and Design | 38 |
| 3.2.2 | Electronic Properties | 39 |
| 3.3 | ThermoChemical NanoLithography: Temperature Dependence | 40 |
| 3.3.1 | Methods and Description of Experiments | 41 |
| 3.3.2 | ThermoChemical NanoLithography: Speed Dependence | 48 |
| 3.3.3 | Controlling Chemical Reactions with Temperature | 51 |
| 3.3.4 | Resolution Measurements | 56 |
| 3.3.5 | Controlling Chemical Reactions with Speed | 57 |
| 3.3.6 | Comparison of Temperature and Speed | 60 |
| 3.4 | Final Word | 61 |

| | | |
|---|---|-----|
| 4 | EXTENSION OF TCNL TO 3D | 63 |
| | 4.1 Introduction | 63 |
| | 4.2 Simulations of Chemical Kinetics in 3-D | 65 |
| | 4.3 Conversion of PXT to PPV | 73 |
| | 4.3.1 Chemical Transformation and Properties of PPV | 73 |
| | 4.3.2 Film Preparation | 76 |
| | 4.4 Measurements of PXT/PPV Transformation | 76 |
| | 4.5 Using Topography to Demonstrate Extensions of TCNL | 83 |
| | 4.5.1 Nano-Scale Control | 84 |
| | 4.5.2 Z-Dependence | 88 |
| | 4.6 Final Word | 91 |
| 5 | PARALLELIZATION OF TCNL | 93 |
| | 5.1 Introduction | 93 |
| | 5.2 Description of Thermal Arrays | 94 |
| | 5.3 Leveling | 95 |
| | 5.3.1 Interaction between a Thermal Tip and a Substrate | 95 |
| | 5.3.2 Array Leveling | 97 |
| | 5.4 Thermal Patterning with Arrays | 98 |
| | 5.5 Thermal Imaging | 100 |
| | 5.5.1 Thermal Imaging with a Single Tip | 101 |
| | 5.5.2 Thermal Imaging with Arrays | 102 |
| | 5.6 Complications with Arrays | 103 |
| | 5.7 Final Word | 104 |
| 6 | CONCLUSIONS AND FUTURE WORKS | 105 |
| | 6.1 Introduction | 105 |

| | |
|---|-----|
| 6.2 Review | 105 |
| 6.3 Future Works and Improvements | 106 |
| 6.4 Applications of Chemical Gradients | 108 |
| 6.4.1 Surface Energy Gradients | 108 |
| 6.4.2 Biophysical Applications | 109 |
| 6.5 Applications of Topographic Gradients | 109 |
| 6.5.1 Transfer of PPV Patterns to PDMS | 110 |
| 6.5.2 Colloidal Patterning | 112 |
| 6.5.3 Nano-Fluidics | 112 |
| 6.6 Final Word | 113 |
| APPENDIX A: DERIVATION OF EQ. 4.2.11 | 114 |
| REFERENCES | 116 |

LIST OF TABLES

Page

Table 1.2.1: Comparison of Lithographic Techniques

14

LIST OF FIGURES

| Page | |
|------|--|
| | Figure 1.2.1: (a) Schematic for μ CP. Reprinted with permission from [17] ©2000 John Wiley and Sons. (b) Example of DNA patterned with μ CP. Reprinted with permission from [18] ©2007 John Wiley and Sons. 3 |
| | Figure 1.2.2: (a) Schematic showing photo-activated chemical reactions in LAPAP. Reprinted with permission from [29]©2003 American Chemical Society. (b) Example of a photo-chemical pattern (scale bar 500 μ m). Reprinted with permission from [30] ©2012 John Wiley and Sons. 5 |
| | Figure 1.2.3: (a) Schematic showing microfluidic setup to generate spatial gradients (b) and (c) Two examples of spatial gradients. Reprinted with permission from [31] ©2001 American Chemical Society. 6 |
| | Figure 1.2.4: (a) Schematic of nanoshaving lithography. Reprinted with permission from [39] ©2008 American Chemical Society. (b) Example of bound nano-graft patterned DNA. Reprinted with permission from [40] ©2002 American Chemical Society. 8 |
| | Figure 1.2.5: Schematic showing electro-conduction based lithography. Reprinted with permission from [42] ©2004 American Chemical Society. 9 |
| | Figure 1.2.6: (a) Schematic of DPN. Reprinted with permission from [45] ©1999 AAAS. (b) Example of DPN pattern made. Reprinted with permission from [50] ©2006 John Wiley and Sons. 10 |
| | Figure 1.2.7: (a) Schematic showing thermomechanical lithography. Reprinted with permission from [52] ©2002 IEEE. (b) Example of 3-D patterning. Reprinted with permission from [55] © 2010 AAAS. 11 |
| | Figure 1.2.8: Schematic of tDPN. Reprinted with permission from [63] ©2009 American Chemical Society. 12 |
| | Figure 1.3.1: Schematic of a thermal cantilever inducing a local temperature profile. The profile spread (a) laterally and (b) into the substrate. 16 |

| | |
|---|----|
| Figure 1.3.2: (a) Experimental setup to verify the ability to create chemical gradients with TCNL. The left rectangle is written starting with a high temperature at the top and finishing with a low temperature at the bottom; the middle starts with a high temperature at the bottom and finishes with a low temperature on the top; the right rectangle is a superposition of the two. (b) Fluorescently labeled pattern corresponding to (a). (c) Plot of the intensity signal versus distance of the left rectangle. The direction is indicated by the arrow in (a), the change in the intensity signal is indicative that TCNL is capable of patterning chemical gradients. | 17 |
| Figure 2.2.1: Thermal reaction for the Cinnamate Polymer | 20 |
| Figure 2.2.2: Time Dependence of eq. 2.2.5 with eq. 2.2.6 | 24 |
| Figure 2.2.3: Temperature Dependence of eq. 2.2.5 with eq. 2.2.6 | 25 |
| Figure 2.2.4: Decay length dependence of eq. 2.2.5 with eq. 2.2.6 | 27 |
| Figure 2.2.5: Interaction between two contact points described in eq. 2.2.10 | 29 |
| Figure 2.2.6: Plot of 2.2.13 with decay length of 100 nm | 31 |
| Figure 2.2.7: Plot of eq. 2.2.15 and higher order variants; the reference speed is 10 $\mu\text{m/s}$ and the reference transformation percentage is 0.99 | 33 |
| Figure 2.3.1: Schematic for eq. 2.3.1 | 34 |
| Figure 2.3.2: Rastering image to pattern a substrate | 35 |
| Figure 3.2.1: (a) Graph of thermal cantilever resistance versus power dissipated across the cantilever; 90% of the power is dissipated in the heater region. (b) SEM image of a thermal cantilever. Image [104] reprinted with copyright permission © 2008 Taylor and Francis | 39 |
| Figure 3.3.1: Chemical structure of polymer | 41 |
| Figure 3.3.2: (a) Typical experiment to test the chemical kinetics model. The numbers indicate typical dissipated powers for these experiments. (b) AFM image of the polymer substrate prior to patterning. (c) AFM image of the pattern detailed in (a). | 42 |
| Figure 3.3.3: Fluorescent image from the experiment shown in Figure 3.3.2 | 44 |
| Figure 3.3.4: (a) Theoretical fluorescent image measured with an uneven illumination field. (b) Theoretical background image indicating the uneven illumination field. (c) Corrected fluorescent image resulting from dividing (a) by (b). The cyan square indicates an inscribed to measure a squares intensity level. | 46 |

- Figure 3.3.5: Comparison of the inset's measured intensity (eq. 3.3.2) (inset same as Figure 3.3.4) with the chemical kinetics model (eq. 3.3.3). There is good agreement between the experiment and the model. 47
- Figure 3.3.6: Comparison of the model with four different speeds (1 $\mu\text{m/s}$, 10 $\mu\text{m/s}$, 100 $\mu\text{m/s}$, 1 mm/s). The results show the curves shift to the right as predicted in chapter 2. 49
- Figure 3.3.7: (a) Experimental setup in which the temperature is fixed, but the speed is varied across 3 orders of magnitude. (b) Fluorescently labeled image corresponding to the experiment in (a). (c) Comparison of the measured fluorescent intensity to the chemical kinetics model with a fixed temperature and varying speed. 50
- Figure 3.3.8: Schematic explaining how to create controlled chemical concentration profiles with TCNL. 52
- Figure 3.3.9: (a) User-defined concentration profile. (b) Map describing the power distribution as a function of position. This is obtained by following the procedures displayed in Figure 3.3.8 (c) Fluorescent image corresponding to the pattern defined in (a) and (b). (d) Plots comparing the user-defined (intended) concentration profiles against the experimentally measured values seen in (c). 53
- Figure 3.3.10: (a) (Left) Original *Mona Lisa* image; (Right) $\sim 30 \times 40 \mu\text{m}^2$ reproduction of the *Mona Lisa* (commonly referred to as the *Mini Lisa*). (b) (Left) *Rose and Driftwood*, 1932, photograph by Ansel Adams, copyright 2012 The Ansel Adams Publishing Rights Trust. (Right) $44 \times 34 \mu\text{m}^2$ reproduction of *Rose and Driftwood*. 55
- Figure 3.3.11: (a) Friction measurement of consecutive TCNL patterned lines spaced by 125 nm. Cyan square indicates the average profile shown in (c); scale bar (red) is 1 μm . (b) FWHM measured with FFM for lines written at different powers. (c) Profile showing a smooth variation of the friction signal over a topographically flat area. The friction shows a measureable change over distance of 20 nm 56
- Figure 3.3.12: Experimental results showing controlled changes in chemical concentrations using variable speed. The plots indicate good agreement between the user-defined profiles and the experimentally measured values. 59
- Figure 3.3.13: Plots showing how errors can be amplified in eq. 3.3.6. See text for details. 60
- Figure 3.3.14: Comparison of fixed temperature versus fixed speed designed patterns. (a) Fluorescent image with fixed temperature on the left and fixed speed on the right. The normalization factor is not shown. (b) Plots of the intensity signals versus intended (solid line). 61

- Figure 4.2.1: (a) Simulation of the surface transformation for a decay length (λ) of 100 nm for four different speeds. Simulations at four different speed for the body transformation for three different z-decay lengths: (b) $\lambda = 50$ nm, (c) $\lambda = 100$ nm, (d) $\lambda = 25$ nm. The assumed film thickness is 50 nm. 68
- Figure 4.2.2: Simulation showing that at larger z-decay lengths ($\lambda = 400$ nm), the body transformation's temperature range starts to overlap with the surface's transformation temperature range. 69
- Figure 4.2.3: Simulation showing that at small z-decay lengths ($\lambda = 1$ nm), activation of individual layers can be observed. 70
- Figure 4.2.4: (a) Simulations (circles) and fits (lines) of $k_{eff}(z)$ based on eq. 4.26 and eq. 4.2.9 for six different z-decay lengths ($\lambda = 25$ nm, 50 nm, 100 nm, 150 nm, 200 nm, and 500 nm). (b) Comparisons of the z-decay length (λ) to the effective decay length (κ) for the same six λ decay lengths in (a). Inset shows how this ratio change for a fix λ of 100 nm and variable T_{peak} . 72
- Figure 4.3.1: (a) Chemical transformation of PXT to PPV. (b) Excitation (solid line) and Emission (dashed line) of PPV. 74
- Figure 4.3.2: (a) Raman measurements indicated an increase in the 1180 cm^{-1} and 1600 cm^{-1} peaks; this indicates the transformation from PXT to PPV. (b) Fluorescent image of PPV patterns before Raman measurements. (c) Fluorescent image of the same PPV pattern after Raman measurement. The circled region indicates the invasive nature of the Raman probing laser. 75
- Figure 4.4.1: (a) Experimental schematic for the measuring the change in the photoluminescence signal with changing heater temperature. Red squares indicate patterns written at $1\text{ }\mu\text{m/s}$, while blue squares are at $10\text{ }\mu\text{m/s}$. (b) Photoluminescent image of the pattern corresponding to the experiment in (a). (c) Semi-quantitative measurements of the signals in (b). (d) Zoomed in version of Figure 4.2.1 (d) to indicate that the at low peak temperatures, the data forms agree. ($\lambda = 25$ nm, film thickness = 50 nm). 77
- Figure 4.4.2: (a) Friction measurement for a series of squares written at heater temperatures of $\sim 150^\circ\text{C}$ up to $\sim 550^\circ\text{C}$. (b) Plots of the friction signal versus heater temperature seen in (a). Above 400°C the friction signal is seen to level off; this is indicative the surface transformation has completely taken place. (c) Plot of the fluorescence signal for the pattern in (a). The signal continues to increase pass the 400°C heater temperature; this suggests the body has not undergone the complete transformation, while the surface has. 80

- Figure 4.4.3: (a) AFM measurements of squares patterned into PPV. The heater temperature range is $T_1 \sim 160^\circ\text{C}$ (lower right) up to $T_{25} \sim 550^\circ\text{C}$ (upper left). (b) Fluorescence signal of the pattern in (a). (c) Comparison of the change in PPV height (depth) (a) versus the intensity signal in (b). The two are approximately linear. 82
- Figure 4.5.1: (a) Spatial distribution of applied voltage to create a $30\ \mu\text{m} \times 40\ \mu\text{m}$ reproduction of the *Mona Lisa*. (b) Fluorescent image of the patterned PPV. (c) AFM image of the patterned PXT/PPV film. Diffraction in (b) limits our ability to see the added details. (d) FFM measurements that qualitatively detail the reproduction. 86
- Figure 4.5.2: (a) AFM image showing $\sim 20\ \mu\text{m} \times 33\ \mu\text{m}$ reproduction of the *Mona Lisa* in PXT/PPV film (*Mona Lisa 2.0*). (b) Fluorescent image corresponding to the pattern in (a). Diffraction makes the image look blurry as compared with the high resolution AFM image. 87
- Figure 4.5.3: Measurements of FWHM of lines made in PXT/PPV film (a) AFM image of lines at different temperatures. (b) Measurements of the FWHM as a function of power and heater temperature. 88
- Figure 4.5.4: (a) Schematic showing an experiment in which the heater temperature is kept constant and the speed is varied as a function of position. (b) AFM image corresponding to the experiment in (a). (c) Plot of the fluorescent signal of the PXT/PPV pattern. (d) Fit of eq. 4.2.11 with experimental results in (b). The measured effective decay length is ~ 3.0 ; we approximate the temperature decay length as $\sim 40\ \text{nm}$. 90
- Figure 5.2.1: (a) Optical image of thermal cantilever array with numbering. (b) Schematic showing a thermal cantilever array inducing a temperature profile in a substrate. 95
- Figure 5.3.1: (a) Resistance measurement as a thermal tip is brought into contact with a surface; also shown in blue is the optical measured force displacement curve. (b) and (c) Schematics showing that at far distance from a substrate (a) the thermal cantilever transfers less heat than close to the surface (b). 97
- Figure 5.3.2: Resistance measurements of individual cantilever's in an array versus distance. (a) Measurement and schematic showing misalignment between the thermal cantilever array and the substrate. (b) Measurement and schematic showing all five tips in contact with the substrate near simultaneously after indicated correction made (a). 98
- Figure 5.4.1: Thermal patterning in a PPV-precursor film made with thermal cantilever array. (a) Raman measurements indicating the transformation from precursor to PPV. (b) Fluorescent image of pentagon PPV patterns made with thermal array. (c) Zoom-in version of patterns from (b). 99

- Figure 5.4.2: Measurements of lines made in PPV-precursor film made with thermal cantilever array (a) Fluorescent image of patterns of lines made with thermal cantilever array. (b) AFM image of patterns imaged in (a). (c) Topography profile for Tip 1 (indicated in blue in (a)), inset indicates a resolution of about 68 nm 100
- Figure 5.5.1: (a) Thermal imaging of a z-calibration grating with a single tip (b) AFM image of the same area measured in (a). 102
- Figure 5.5.2: Thermal image obtained from a z-calibration grating with a thermal cantilever array. 103
- Figure 6.4.1: Schematic showing transfer of PPV topographic pattern to PDMS. 111
- Figure 6.4.2: Experimental evidence showing the transfer of (a) PXT/PPV topographic patterns to (b) PDMS. 112

SUMMARY

This thesis presents and develops a systematic approach to ThermoChemical NanoLithography (TCNL). TCNL is a scanning probe microscope based lithographic technique which uses a localized temperature profile to induce chemical transformations. The intent of this work is to extend our understanding of TCNL to be able to model and control chemical reactions taking place at the nano-scale.

We break this work up into four parts. The first part adapts a chemical kinetics model to predict and explain some of TCNL's features. By looking at different parameters, we gain insight into how TCNL can be used to control surface chemical reactions. The second part of this work focuses on studying only surface reactions. As part of this, we use fluorescent microscopy to quantify the chemical transformation, and after successfully verifying the adapted chemical kinetics model, we apply the model to control the chemical transformation process and demonstrate excellent precision down to the sub-micron length scales.

Having verified the chemical kinetics model for surface reactions, we look to extend the model beyond surface effects and study the penetration of the reaction into the substrate. We also develop analysis for using other TCNL induced material property changes to measure different aspects of the substrate's chemical transformation. Finally, the last part of this work focuses on parallelization of TCNL. We demonstrate nano-scale resolution can be extended to multiple tips simultaneously.

CHAPTER 1

INTRODUCTION

1.1 Introduction

Micro and nano-lithographic techniques are quintessential to everyday life and in many research fields. Lithographic techniques make possible circuits for computer and microchips[1], they make possible the parallelization of medical diagnoses[2], and they control the fundamental interactions between materials and the environment[3-4]. As research has tended towards nanotechnology[5], nano-lithographic techniques are becoming particularly important; nano-lithographic techniques have been used to introduced band gaps in graphene nano-ribbons[6] and for the development of protein nano-arrays[7]. A fundamental challenge to these micro and nano-scale applications is the need to strategically and intentionally position molecules in an organized fashion.

For the most part, lithographic techniques have been developed to fulfill a need or a particular requirement; soft lithography, for example, was developed as an alternative to photolithography for a variety of different materials and surfaces[8]. While many techniques have been developed, one of the characteristics that is lacking in many lithographic techniques is the ability to introduce different levels of molecular concentrations; many are binary in nature. There are already many research fields which would benefit from a systematic technique which can control surface concentrations. For example, controlled variations in concentration (hereto referred as gradients) of the protein laminin have directed axonal growth[9-10]; chemical gradients have also induced droplet motion against gravity because of the controlled variations in surface energy[11-12]. Controlled variations in a surface's topography alter how a surface interacts with the environment. Hydrophobic materials have shown transitions to super-hydrophobic regimes as a result of increased surface roughness[3, 13]. Electronic heat sinks are often

designed with corrugated ridges to allow for more cooling from the increased surface area[14]. This latter example would be particularly valuable to implement for nano-tronics since this would protect nano-scale devices from overheating, prolonging their lifetimes.

Surface design is essential to many nano and micro-scale applications because they control the foundations and in some cases the intrinsic properties of devices. Lithographic techniques fill these needs to alter both topography and chemistry[2, 15-16]. Lacking, however, is a technique capable of controlling these variations (hereto referred to as chemical and topographic gradients) down to the nano-scale. The focus of this thesis is to overcome these limitations using the promising technique Thermo-Chemical Nanolithography. In the rest of this chapter, we review many state-of-the-art lithographic techniques, and we focus on their advantages, disadvantages, and limitations as they relate to gradient patterning. The chapter concludes with an overview of TCNL's potential to create chemical gradients, and finally we outline how we will systematically go about doing this in the remainder of this thesis.

1.2 Lithographic techniques

1.2.1 Microcontact printing

Microcontact printing is a lithographic technique which uses a stamp to pattern areas[8]. Usually the stamp is formed out of an elastomeric material, such as Polydimethyl siloxane (PDMS)[17]; the standard procedures are shown in Figure 1.2.1, where first a mold is filled with un-cured elastomeric material. The uncured polymer fills the mold, and after the stamp is cured and released, the mold imprint remains in the solid elastomer. After incubating the stamp with chemical materials, such as proteins, DNA, or organic molecules, the stamp transfers the materials to a target surface. The key advantage to microcontact printing is the high-speed and high-throughput patterning[8]; there is also a vast amount of literature on the diverse materials that have been

transferred[18-21], as well as the number of substrates with which this technique has been used. One of the disadvantages is that micro-contact printing requires new molds and new stamps whenever different pattern sizes and shapes are needed.

Typically, this technique is used for micro-scale patterning, but there are modifications, such as using elastomeric materials with higher elastic coefficients[22-23], allowing for ~ 100 nm scale devices to be printed. The later is sometimes referred to as nano-contact printing.

For the most part, the technique is binary; however, there has been some research dedicated to making chemical gradients by using stamps with variable thickness[24]. These specialized stamps are infused with a chemical molecule (such as an alkanethiol). When the stamp is brought into contact with a surface (for example gold), molecules at the stamp-substrate interface covalently attach to the surface. As time elapses, the molecules in the stamp diffuse and attach to the substrate, and a chemical gradient forms analogous to the stamps variable thickness. Results with alkanethiols have shown variable chemical concentrations over distances of ~ 10 mm, but given the ratios between the length and heights, it would be difficult to extend this technique down to the micro-scales.

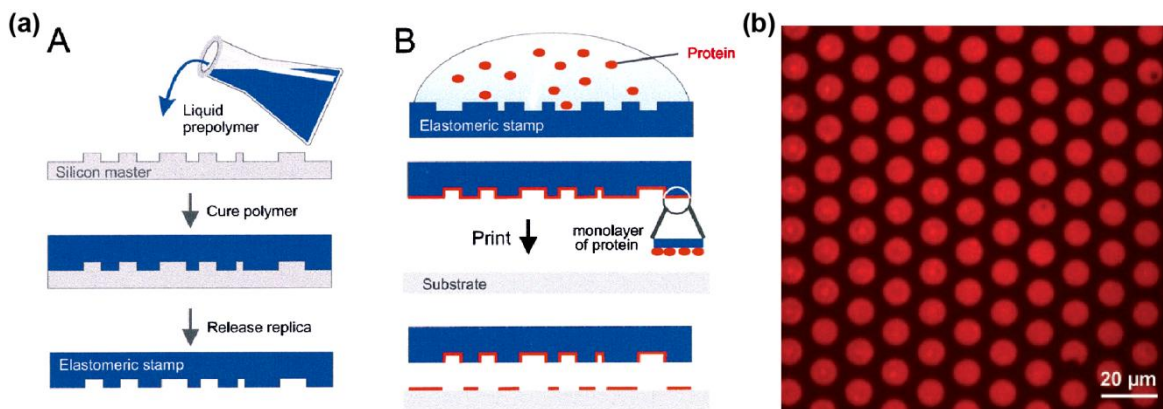


Figure 1.2.1 (a) Schematic for μ CP. Reprinted with permission from [17] ©2000 John Wiley and Sons. (b) Example of DNA patterned with μ CP. Reprinted with permission from [18] ©2007 John Wiley and Sons.

1.2.2 Light Based Lithographies

Light based lithographies are omni-present throughout research and industrial applications[25]. In particular, photolithographic techniques are generally robust, fast, and mass scalable, hence their ubiquity particularly in semi-conducting industries. Typically, they employ positive or negative resists to protect patterned areas from wet and dry etch based techniques. Despite being diffraction limited, resist based photolithographies have achieved nanometer scales by employing materials with high indices of refraction and two photon dependent materials to narrow the diffraction limit[26-27].

Other light based techniques are also available. Of particular note is a technique known as laser-assisted adsorption by photobleaching (LAPAP)[9, 28], which uses light to induce radical excited states which react with surface bound molecules[29]. This technique has demonstrated an impressive ability to pattern chemical gradients such as those seen in Figure 1.2.2. The technique is relatively easy to implement, but is limited by a combination of diffusion and the diffraction limit down to about a micron. The ability to introduce spatial light modulators and digitally controlled micro-mirror devices makes this technique attractive for high speed pattern production[30].

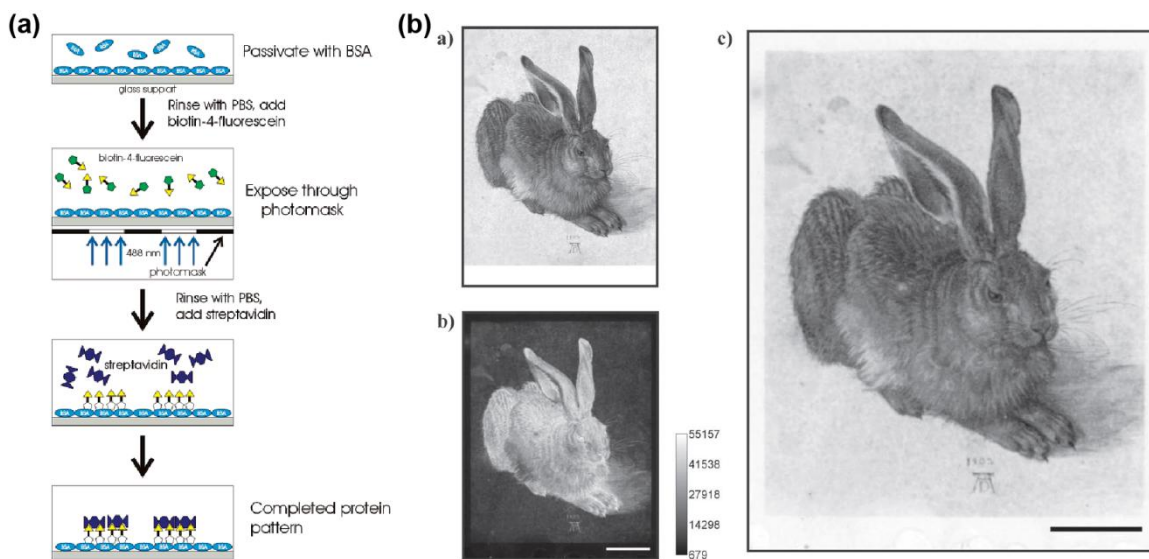


Figure 1.2.2 (a) Schematic showing photo-activated chemical reactions in LAPAP. Reprinted with permission from [29] ©2003 American Chemical Society. (b) Example of a photo-chemical pattern (scale bar 500 μm). Reprinted with permission from [30] ©2012 John Wiley and Sons.

1.2.3 Micro-Fluidics

Micro-fluidic devices are viable lithographic technique with the ability to create chemical gradients; usually micro-fluidic patterning is used to create spatial gradients[31], but the technique has been applied to produce surface gradients[10]. Usually different concentrations of intended molecules are flown through different connected configurations of “Y” shaped fluid devices, such as those shown in Figure 1.2.3, to create controlled spatial chemical concentrations. The diverse forms made, however, are on several hundred microns to millimeters wide, and the technique is limited in its ability to fabricate complex patterns since only 1-D patterns are currently available rather than 2-D.

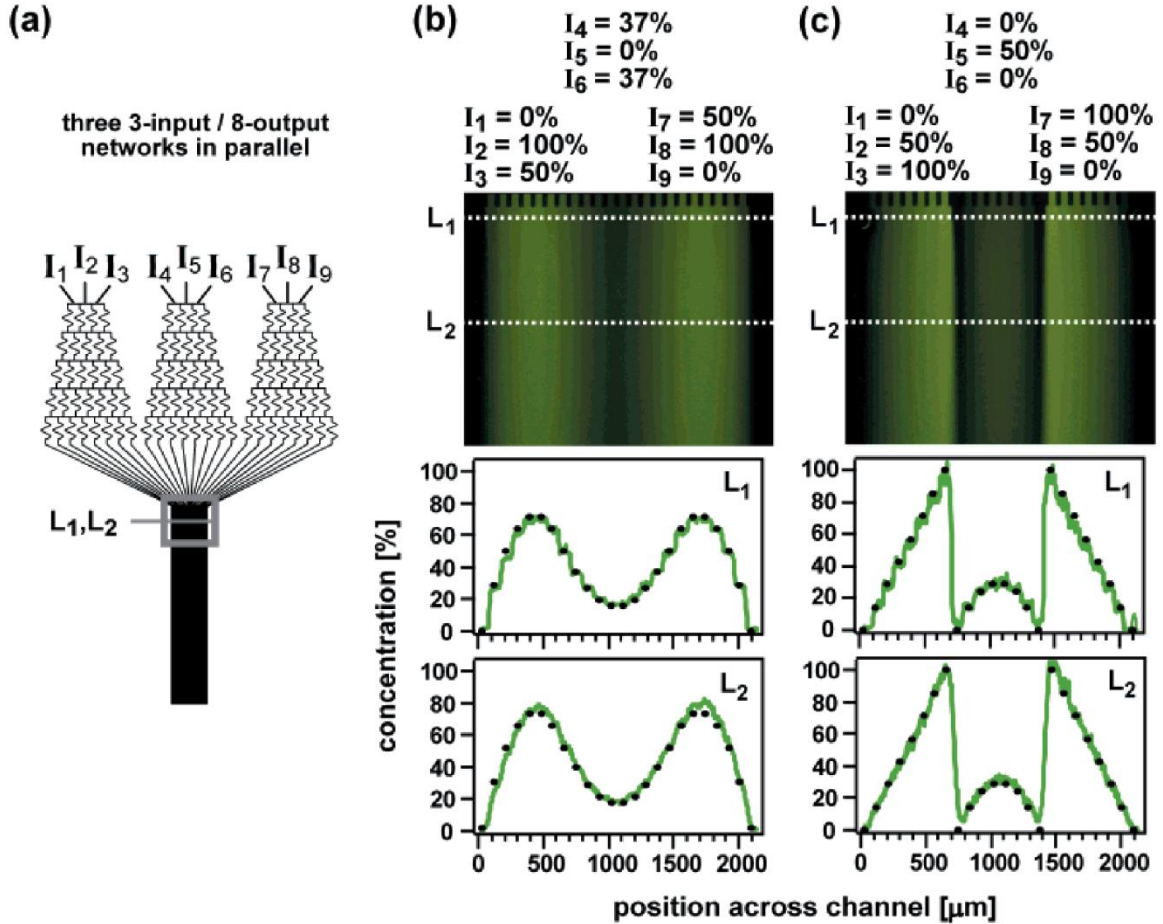


Figure 1.2.3 (a) Schematic showing microfluidic setup to generate spatial gradients (b) and (c) Two examples of spatial gradients. Reprinted with permission from [31] ©2001 American Chemical Society.

1.2.4 Electron Beam Lithography

Though primarily developed for the semi-conducting industry[2], Electron beam lithography (E-Beam) has also been used to pattern substrates[32-33] and is well known for its high resolution from the focused electron beam. The resolution is not determined by the electron beam, but rather by the interaction of the electrons with the material[2, 34]. Materials that scatter electrons more tend to have lower resolutions. Generally the resolutions are sub-100 nm, and in some cases have been shown to go down to 5-10nm[35-36]. Typically for nano-patterning, E-beam will use different forms of electron

sensitive resists and uses techniques similar to photolithography to pattern areas[37-38]. The disadvantage is the time, expense, and the high vacuum associated with e-beam[35].

1.2.5 Nano-shaving/Nano-grafting

Nano-grafting and nano-shaving are similar techniques, which use a stiff AFM cantilever to scratch molecules off a surface, which is usually a self assembled monolayer (SAM)[39-40]. Figure 1.2.4 shows a schematic and example. With the plowed area now exposing a different chemistry than the unscathed area, different molecule types can be site-specifically attached. This technique can be performed in a solution containing the secondary molecule (nano-grafting), or else molecules are attached serial to patterning (nano-shaving). The resolution varies slightly from about 100 nm to 5-10 nm depending on the radius of curvature of the tip and the interactions between the tip and surface[35, 40].

Both processes are rather aggressive in nature, and usually require a large loading force to chemically break bonds and remove molecules from the surface. One of the advantages to this technique is that because the removal force is so large, the same probe can image the sample with a lower contact load (or even in AC mode).

Other forms of this technique have used oscillating AFM tips to remove molecules from a surface[41]. By using actuated tips, different flexure modes can write or re-write patterned areas. This particular adaptation has been shown to have resolutions down to 50 nm.

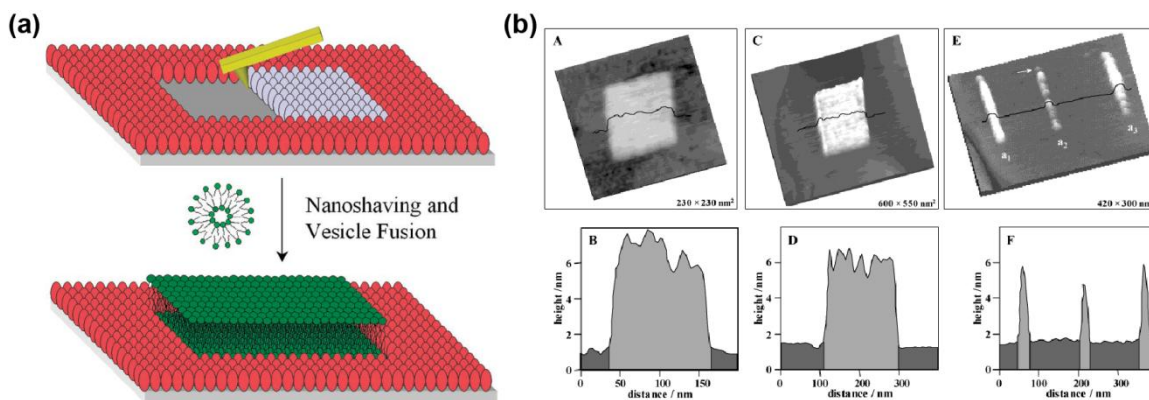


Figure 1.2.4 (a) Schematic of nanoshaving. Reprinted with permission from [39] ©2008 American Chemical Society. (b) Example of bound nano-graft patterned DNA patterns. Reprinted with permission from [40] ©2002 American Chemical Society.

1.2.6 Electric and Conductive SPM techniques

Some SPM based techniques use localized electric fields and currents to pattern substrates with a conductive SPM probe. Electro-oxidation techniques chemically reduce substrates to introduce chemically varying substrates such as those seen in Figure 1.2.5[42-43]. A similar technique[44] has demonstrated chemical gradients, but the speed (~ 50 nm/s) associated with this particular application is fairly slow. In general electro-chemical techniques are slow (~ 10 $\mu\text{m/s}$), and the resolutions are on the order of 25 nm.

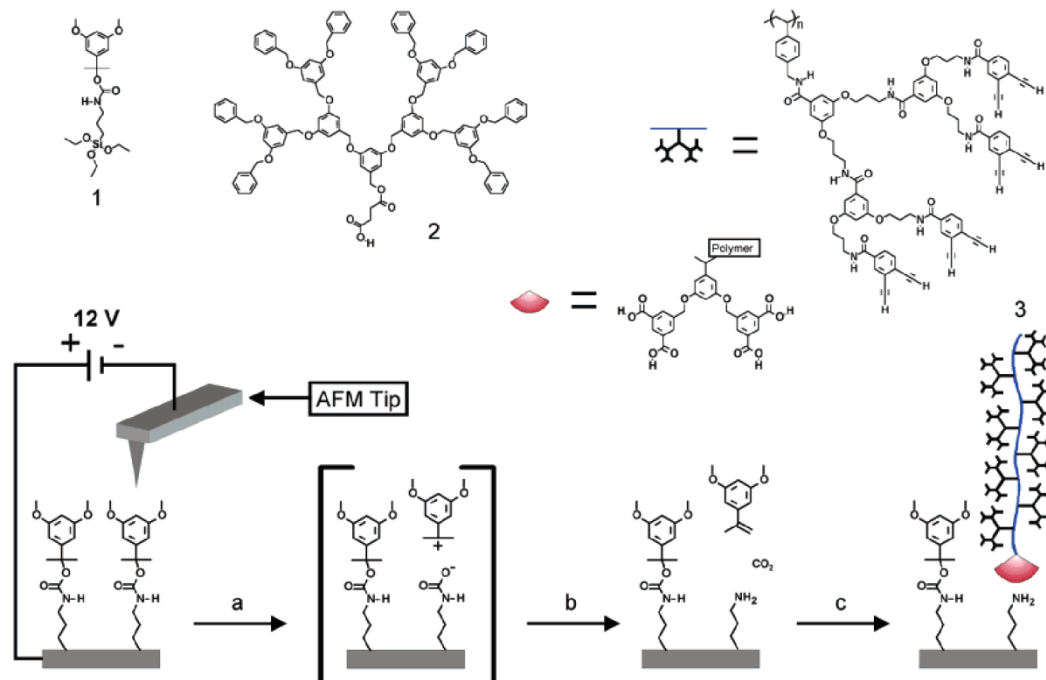


Figure 1.2.5 Schematic showing electro-conduction based lithography. Reprinted with permission from [42] ©2004 American Chemical Society.

1.2.7 Dip-Pen Nanolithography

Dip-Pen Nanolithography (DPN) is another SPM based technique, which uses an inked AFM tip to pattern dissolved “ink” molecules[45] (see Figure 1.2.6). Typically to insure that the ink stays on the tip, the SPM probe needs to be chemically modified. A number of diverse molecules have been patterned on a variety of surfaces[16, 46-47]; however, with each new molecule a new chemistry modification is required[48]. While the technique has been shown to achieve ~10 nm[49], typical resolutions are sub-100 nm[45]. The technique is limited by fluid transport rates and as a result it is a fairly slow SPM lithography (typical speeds are ~1 $\mu\text{m/s}$ or slower). By increasing dwell time (>1 min), different spot sizes can be reliably reproduced. One of the disadvantages to DPN is the inability to image the patterned areas without replacing the SPM tip; moreover, tip-surface contact needs to be broken in between patterned areas.

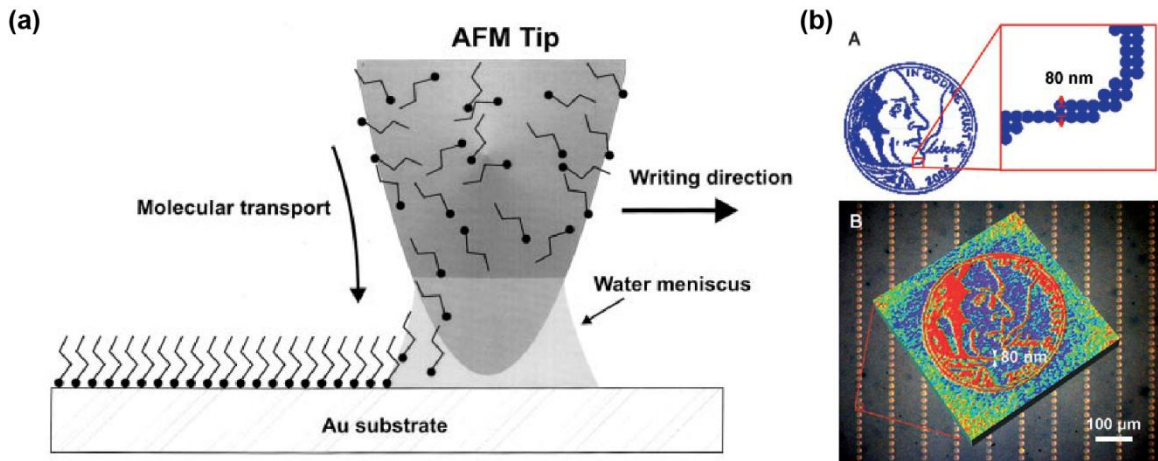


Figure 1.2.6 (a) Schematic of DPN. Reprinted with permission from [45] ©1999 AAAS. (b) Example of DPN pattern made. Reprinted with permission from [50] ©2006 John Wiley and Sons.

1.2.8 Thermal\Thermomechanical Lithography

Thermomechanical lithography uses a semi-conducting thermal cantilever to induce indents into a substrate. Thermal cantilevers are designed so that if biased with a voltage, the heat generated from the dissipated power raises the cantilever's temperature to several hundred degrees[51]. When brought into contact with a polymer substrate and heated, an indentation can form if the temperature exceeds the glass transition temperature (thermo) and a large enough load is applied (mechanical)[52]. Different loading forces and temperatures change the interaction and the resolution[53]. A schematic is shown in figure Figure 1.2.7 a.

Though initially the focus was on finding a new medium to increase data storage[54], the technique has grown to include patterning resists with extraordinary resolution (~10 nm) and extraordinary detail, such as the 3-D reproduction of Mount Matterhorn[55] (Figure 1.2.7 b). Thermal techniques can usually be run at high speeds (~1-10 mm/s)[56]. One of the main drawbacks to any thermal and thermomechanical lithography is the fact that the thermal tips are easily contaminated[57-59]. There are

several ways around this such as using diamond coated tips[60] and using a modified version of thermal lithography[56].

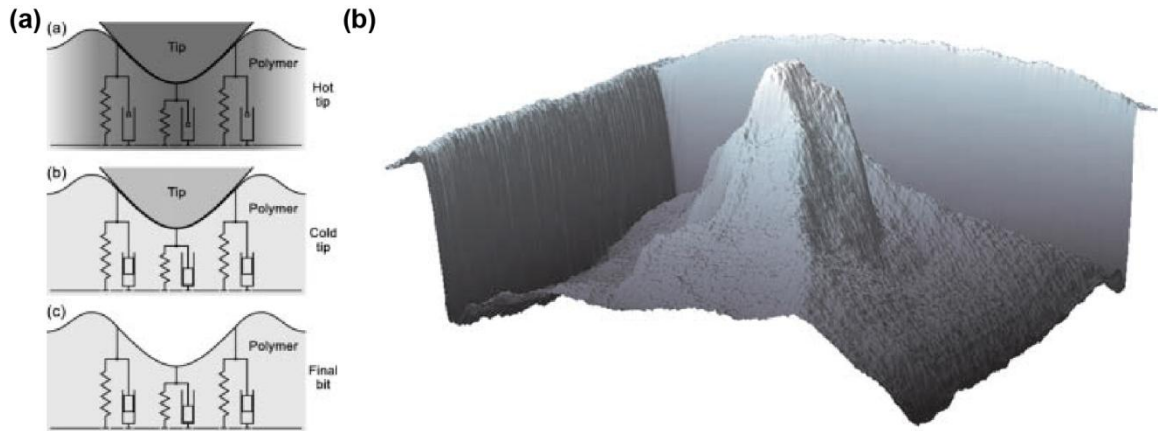


Figure 1.2.7 (a) Schematic showing thermomechanical lithography. Reprinted with permission from [52] ©2002 IEEE. (b) Example of 3-D patterning. Reprinted with permission from [55] © 2010 AAAS.

1.2.9 Thermal Dip-Pen Nanolithography

Thermal Dip-Pen Nanolithography (tDPN) combines thermal cantilevers with DPN; by coating a thermal cantilever with a solid ink, the thermal cantilever can be heated to melt the solid ink (thermal) and subsequently write the liquid ink (DPN)[61]. Cooling the tip solidifies the ink and this ability removes the continuous contact issue associated with DPN; however, one disadvantage is that depending on the substrate properties, the cooling can take several minutes[62]. The technique has been shown to achieve resolutions down to ~100 nm. If the ink is doped with nano-particles, the capillary forces result in nano-particle alignment as seen in Figure 1.2.8[63].

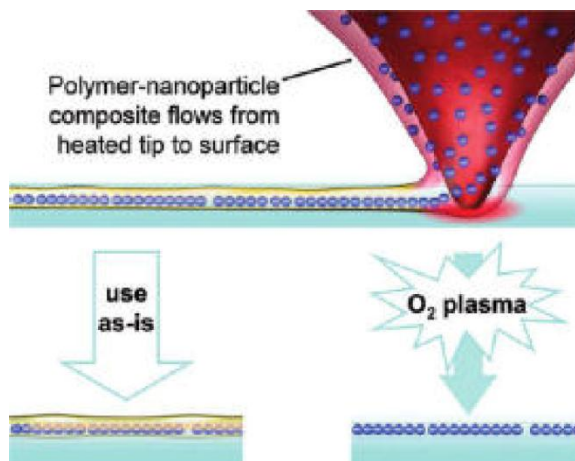


Figure 1.2.8 Schematic of tDPN. Reprinted with permission from [63] ©2009 American Chemical Society.

1.2.10 ThermoChemical Nanolithography

ThermoChemical Nanolithography (TCNL) uses a localized temperature profile to induce chemical transformation on a substrate. The technique has been used to functionalize substrates to attach proteins or convert to other functional groups[64], reduction of graphene oxide[65], reduction of graphene fluoride to graphene[66], crystallization of ceramic materials[67], changing hydrophobic materials to hydrophilic[68-69], and for the transformation of a precursor film into a semi-conducting organic polymer[70]. Other variants of the technique include using thermal cantilevers to induce retro-Diels-Alder[71] reactions and depolymerization[56, 72] of organic polymer films; these variants introduce changes to the surface's topographic structure. While typically TCNL employs the thermal cantilevers previously discussed, other forms have used small wires to produce the same effect[59]. The resolution is substrate dependent, but ranges from ~10 nm up to ~100 nm. Researchers have shown that TCNL can be done at high speeds (~ 1 mm/s)[64, 68]. Since TCNL is based on temperature dependent phenomenon, it is possible to control the relative amount of chemical transformation taking place by tuning the temperature[58].

All of the mentioned lithographic techniques are summarized in Table 1.2.1; the resolutions, some advantages and disadvantages are listed there as well. Though only a few are reviewed here, there are vast numbers of lithographic techniques[73-81].

Table 1.2.1 Comparison of Lithographic Techniques

| | Advantage | Disadvantage | Resolution |
|-------------------------------|-------------------------|----------------------|--|
| μ CP | Fast, Parallel | Rigid | \sim 100-1 μ m \sim 10 nm-1 μ m |
| Photolithography | Fast, Parallel, Tunable | Diffraction Limited | μ m |
| μ Fluidics | Fast, Parallel | Rigid | \sim 1mm |
| E-Beam | High Resolution | Cost, Time, Vacuum | \sim 5 nm |
| Nano-shaving/Nano-grafting | High Resolution | Aggressive technique | 5-100 nm |
| Electro-oxidation Lithography | High Resolution | Slow | 25 nm |
| DPN | High Resolution | Slow | 10 nm |
| Thermal Lithography | High Resolution, Speed | Tip Contamination | 10 nm |
| tDPN | Write/Read Capabilities | Slow | 100 nm |
| TCNL | High Resolution, Speed | Tip Contamination | \sim 10-100 nm |

1.3 Chemical and Topographic Gradients

While there is no direct answer or evidence as to which technique is the best, certain standards have been suggested. Many of the listed techniques fulfill some of these suggested niches, but most fail in some area or another. In practice, the best technique is the one that fits an applications needs. For example, nano-scale studies would probably avoid light based techniques, and focus more on a SPM based lithography or E-beam.

The challenge proposed in the introduction was to develop a technique capable of creating controlled chemical and topographic gradients on the nano-scale to the micro-scale. The only lithographic technique which has shown promise to design and control a surface's chemical and topographic morphology across these scales is ThermoChemical NanoLithography. There exists some preliminary evidence to suggest that TCNL can fabricate chemical gradients[64, 70], but until recently[58], a systematic approach was lacking. The next section gives direct experimental evidence to prove that TCNL is capable of creating chemical gradients; surface topographic gradients will be left to a later chapter.

1.3.1 ThermoChemical Nanolithography: Evidence of Chemical Gradients

As previously described, TCNL is a lithographic technique which uses a thermal cantilever to induce chemical transformations at a surface. The details of these thermal cantilevers are reviewed in chapter 3, but their most important feature is the ability to locally heat across several hundred degrees[51]. When brought into contact with a substrate, a heated cantilever induces a temperature profile in the substrate as depicted in Figure 1.3.1. The input of thermal energy causes a thermally driven chemical reaction.

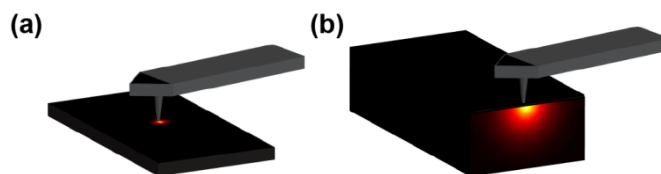


Figure 1.3.1 Schematic of a thermal cantilever inducing a local temperature profile. The profile spread (a) laterally and (b) into the substrate.

Although this technique has been used for a number of material substrates, the ability to create *continuous* chemical gradients is demonstrated on a thermally activated polymer substrate. The polymer, poly((tetrahydropyran-2-yl N-(2-methacryloxyethyl)carbamate)-co-(methyl 4-(3-methacryloxypropoxy)cinnamate))¹, has a protected functional amine group. When heated, the protection group dissociates from the surface, leaving an exposed reactive amine to which molecules with complimentary chemistries can be site-specifically bound. Proteins, DNA, and other biomolecules have been attached to these localized amine areas[64]. These amines have also been chemically transformed into other functional groups such as carboxyl or maleimides[64]. To test the ability to create gradients on this polymer substrate, a thermal cantilever is brought into contact with this polymer substrate and the cantilever's temperature is controlled as a function of position, such as the experiment shown in figure 1.3.2. When the sample is labeled with a fluorescent dye, areas with greater concentrations of amines result in a greater amount of fluorescent dye binding. The bright fluorescent signal seen in figure 1.3.2 at the high temperature areas corresponds to more bound amines, while the dimmer signal results from the low temperature areas. This pattern provides evidence that TCNL can make chemical gradients, but without a

¹ Synthesized by Professor Seth R. Marder's lab at Georgia Institute of Technology

systematic study, the need to control and extend this process to other materials and substrates remains unanswered.

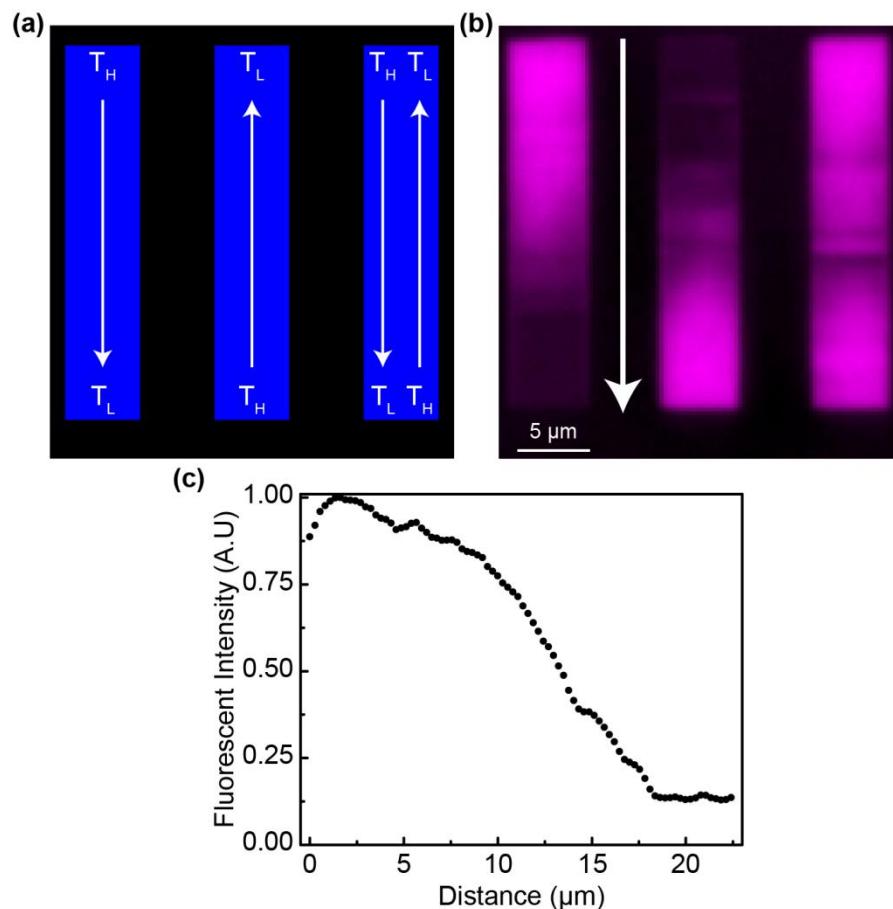


Figure 1.3.2 (a) Experimental setup to verify the ability to create chemical gradients with TCNL. The left rectangle is written starting with a high temperature at the top and finishing with a low temperature at the bottom; the middle starts with a high temperature at the bottom and finishes with a low temperature on the top; the right rectangle is a superposition of the two. (b) Fluorescently labeled pattern corresponding to (a). (c) Plot of the intensity signal versus distance of the left rectangle. The direction is indicated by the arrow in (a). The change in the intensity signal is indicative that TCNL is capable of patterning chemical gradients.

The goal of this thesis is to develop a systematic approach to create and design controlled chemical gradients with TCNL. While so far, we have only discussed

preliminary evidence with chemical gradients, we exploit TCNL to create topographic gradients with precisions down to the nano-scale. A chemical kinetics model is employed to predict the transformation taking place at a substrate. Once an approach has been established, systematic protocols will be developed to produce desired chemical gradients and topographic gradients. Finally with the goal of making the technique high throughput and fast, some of this work will be dedicated to discussing parallelization of TCNL using arrays of thermal cantilevers. The long term impact of this work is ability to generalize the methods and techniques discussed to apply to other materials and substrates.

The remainder of this study is broken down into five chapters. Chapter two reviews and discusses the mathematics of coupling chemical kinetics with TCNL. Chapter three experimentally verifies the results derived in chapter two, and applies these results to controllably varying chemical concentrations. While chapter three focuses on surface effects, chapter four shifts this focus to how the chemical kinetics penetrates into the sample. Chapter 5 discusses parallelization, and finally chapter 6 concludes with a discussion of areas of ongoing research and possible applications for the works developed in this work.

CHAPTER 2

CHEMICAL KINETICS MODEL

2. 1 Introduction/Motivation

Modern fabrication processes have paved the way for advancements in technology and in research. These advancements have been particularly apparent in semi-conducting and electronic device manufacturing and miniaturization. Prevalent among the fabrication methods are photolithographic techniques, which as the name suggests uses light (photo) to crosslink photo-resists site-specifically (lithography)[26, 82]. Since photolithography is light based, it is diffraction limited, but interestingly, this limitation has not prevented fabrication engineers from extending photolithography to nano-scale sized devices[83]. It is not so much that these scientists and engineers have broken the laws of optics, but rather have used the laws to their advantage. For example, in photolithography, material scientists have developed high-dielectric materials to allow fabrication engineers to tune the diffraction limit to meet their needs[27]. The added value of high dielectric constants comes from understanding and deriving the limitations from the wave theory of light. Other improvements, such as studying which materials enhance two photon-absorption, have aided in micromachining 3-D objects with light[84]. Much as wave theory provided the fundamental principles to allow researchers and engineers to push the limits of photo-patterning to near any size[85], it stands to reason that any technique will be open to substantial improvement once the fundamental principles have been derived and validated. This chapter is dedicated to writing and deriving the principles governing ThermoChemical Nanolithography (TCNL) with the motivation of understanding TCNL to develop a novel approach for patterning controlled chemical concentrations with high resolution.

2.2 Chemical Kinetics Model

Understanding that TCNL induces a localized chemical transformation at a substrate, it is reasonable to view this technique through the lens of chemical kinetics, the study of chemical reactions. While TCNL has been performed on a multitude of substrates, we focus on a model surface, which will be used to measure a relative chemical concentration with the help of fluorescent microscopy as explained in chapter 3. Our choice for this study is a spin casted organic polymer film (poly((tetrahydropyran-2-yl N-(2-methacryloxyethyl)carbamate)-co-(methyl 4-(3-methacryloyloxypropoxy)cinnamate))); the synthesis and surface preparation protocols are well described elsewhere[58, 64]. The polymer and polymer substrate were synthesized in Professor Seth R. Marder's lab at Georgia Institute of Technology. Briefly, it has been synthesized to have a protected functional group, and when thermally activated, the protection group dissociates from the polymer, leaving behind an exposed functional group. The reaction dynamics are shown in Figure 2.2.1, where the left hand side shows the protected polymer and the right hand side shows the thermally activated deprotected polymer with exposed, reactive amines[64].

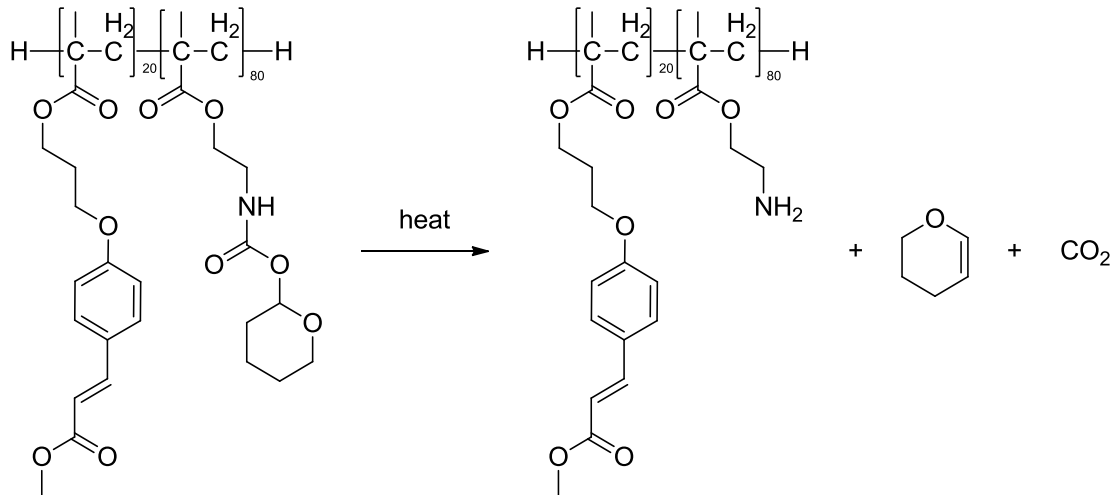


Figure 2.2.1 Thermal reaction for the Cinnamate Polymer

This transformation from the protected, nonfunctional group to an exposed, active functional amine is described as a chemical reaction:



where R is the reactant, the protected polymer, and P is the final product, the deprotected polymer. Based on the likely deprotection mechanism[64], this reaction should act similarly to a first order chemical kinetics reaction. The rate equation for this polymer goes as:

$$\frac{d[P]}{dt} = k[R] = k([P_{tot}] - [P]) \quad (2.2.2)$$

where $[P]$ is the product concentration, $[R]$ is the reactant concentration, $[P_{tot}]$ is the maximal product concentration (in this case the maximal density of deprotected amines), and k is the reaction rate. The reaction rate, k , is defined using the Arrhenius formula:

$$k = A e^{\frac{-E_a}{R \cdot T}} \quad (2.2.3)$$

where A is the temperature independent Arrhenius constant, E_a is the activation energy, R is the gas constant, and T is the temperature. Chemically, E_a is the energy barrier to cause the chemical transformation; more specifically, the activation energy has been associated with the energy difference between the reactant and an intermediate species[86-87]. A represents the maximal rate of reaction, The literature suggests that there are other variants k , such as the Arrhenius coefficient having a $T^{1/2}$ dependence[88]. Often, these other forms for A are intended for bimolecular reactions[89], collision based reactions[86], or reactions spanning a large temperature range[88]. Moreover, for narrow temperature range consistent with this work, there are very minor differences in the final values, and simulations, in which temperature dependent Arrhenius values were used, show negligible differences. It suffices for the

intent of this work to use a temperature independent Arrhenius constant. The values for E_a and A come from ThermoGravometric Analysis (TGA)² and are given by 134 ± 32 kJ/mol[58] and $1.7 \times 10^{16} \text{ s}^{-1}$ [90] respectively. Note that since A is so large, the correct order of magnitude is sufficient (for more details, see SI of reference[58])

The solution to eq. 2 at a constant temperature is:

$$\frac{[P]}{[P_{tot}]} = 1 - e^{-k \cdot t} = 1 - e^{-A \cdot t \cdot e^{-\frac{E_a}{R \cdot T}}} \quad (2.2.4)$$

This equation applies to instances in which the temperature is time independent (not changing in time).

2.2.1 Static Tip Solution

When a thermal tip is brought into contact with the substrate and heated, the surface locally heats until it reaches a static temperature profile, $T(\bar{r}, \bar{r}_o)$, where $\bar{r} = (x, y, z)$ is the spatial coordinate, and $\bar{r}_o = (x, y, z)$ is the coordinate describing the tip position. The time scale for this heating has been suggested to be about 1 μs [91]. A quick calculation based on the time dependent heat equation computes a lower bound for the times scales. A typical organic polymer has a specific heat capacity $C \sim 1 \text{ kJ} \cdot \text{kg}^{-1} \cdot \text{K}^{-1}$ and a thermal conductivity, $k \sim 1 \text{ W} \cdot \text{m}^{-1} \cdot \text{K}^{-1}$; the length scale is $\sim 20 \text{ nm}$. For these values, the associated heat equation time scale goes as 10^{-13} s . The discrepancy between the literature values and this computed value probably arises from the fact that the reference[91] may be including cantilever heating time-scales, which are also about 1 μs [92], and that air conduction for the above calculations are ignored. The near instantaneous equilibrium time scale acts as a lower bound, since given the length scales

² Measurements performed in Professor Seth R. Marder's lab at Georgia Institute of Technology

and the calculated time scale, the hyperbolic heat equation[93] is more appropriate. For this work, since we focus mostly on effects taking place on time scales below both limitations, we ignore the time dependence of the temperature profile. Assuming the static profile is instantaneously reached, the static solution for a tip in contact with a substrate is:

$$\frac{[P]}{[P_{tot}]} = 1 - e^{-k \cdot t} = 1 - e^{-A \cdot t \cdot e^{\frac{-E_a}{RT(r-r_0)}}} \quad (2.2.5)$$

where t_d is the tip dwell time. Wanting to gain some insight into how eq. 2.2.5 evolves and changes with various parameters, we leave the discussion of the temperature profile form until a later section of this chapter, and we will work with a 1-D model temperature profile. To find a reasonable temperature profile, the surface temperature should approach room temperature and should attain a peak at the point of contact (here the point of contact is $x_o = 0$). Since our attempt is to learn how the reaction evolves, one reasonable temperature profile that meets these criteria is given by:

$$T = T_o + (T_{peak} - T_o) e^{-\frac{|x|}{\lambda}} \quad (2.2.6)$$

where T_{peak} is the peak temperature, and lambda is a decay length. Plugging this form into eq 2.2.5, there are three parameters to tune: dwell time (t_d), peak temperature (T_{peak}), and decay length (lambda). Each parameter is discussed separately, and all simulations were done in Matlab to couple eq. 2.2.5 with eq. 2.2.6. Only one parameter is varied for each simulation.

Time Variation

Figure 2.2.2 shows that for a fixed decay length (lambda = 100 nm) and peak temperature ($T_{peak} = 250^\circ\text{C}$), longer dwell times increase the concentration of the final product; as seen from the inset, the Full Width at Half Maximum (FWHM) also increases

with dwell time. Physically, as time elapses the chance of a reaction increases; this manifests in two different ways: the percent transformation increases everywhere up to a maximum and the FWHM continues to increase even beyond the max percent transformation.

Developing intuition with dwell time provides the background to understand how writing speed affects TCNL. As will be demonstrated in a subsequent section, there is not a perfect correspondence between the speed and inverse dwell time because of the increased complexity resulting from the tip motion; however, the analogy between inverse time and speed suffices to gain insight. For example Figure 2.2.2 also shows that to span from 0.01 to 0.99 percent transformation, the dwell time scales span from 15 μs to 6.9 ms; this is 3 orders of magnitude in time scales. Prematurely, we expect that in order to span from 0.01 to 0.99 percent transformation at a fixed temperature, the speed will span 3 orders of magnitude.

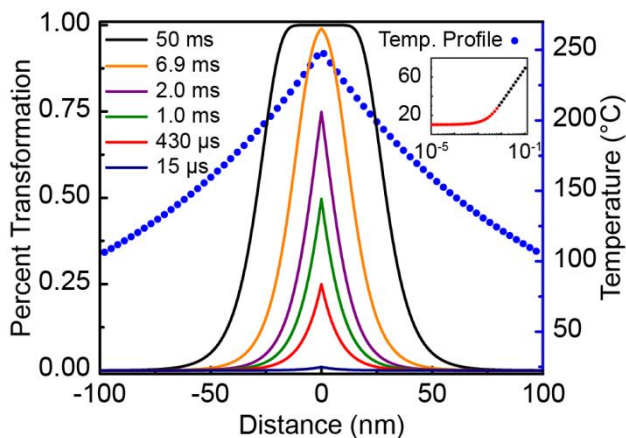


Figure 2.2.2 Time Dependence of eq. 2.2.5 with eq. 2.2.6

Temperature Variation

Figure 2.2.3 shows several different peak temperature profiles (543 K, 523 K, 503 K, 493 K, 468K, and 433 K) at a fixed dwell time of 6.9 ms and a fixed decay length of

100 nm. As the temperature increases, product concentration also increases; looking back at eq. 2.2.3, the reaction rate, k , has a temperature dependence akin to a Boltzmann factor, and it is indeed related to the probability that a reaction will occur[86]. Higher temperatures increase the probability of reaction, and this mathematically manifests as an increase in the reaction rate. The ability to tune the reaction rates with temperature is tantamount to controlling the extent of a localized reaction, and we exploit this dependence in chapter 3 to create controlled concentration profiles.

One of the key differences between time and temperature is the scale to achieve the same results. To span most of the product range (0.01-0.99), for temperature requires about 433 K-543K; whereas, for the same product range, time requires 3-4 orders of magnitude. The scale differences arise from the fact that time alters the reaction rate linearly, whereas temperature affects the reaction rate through a Boltzmann exponential factor. As the thermal energy approaches the activation energy, there is a rapid turnover in the reaction's probability; this leads to the short range over which the temperature activates the reaction.

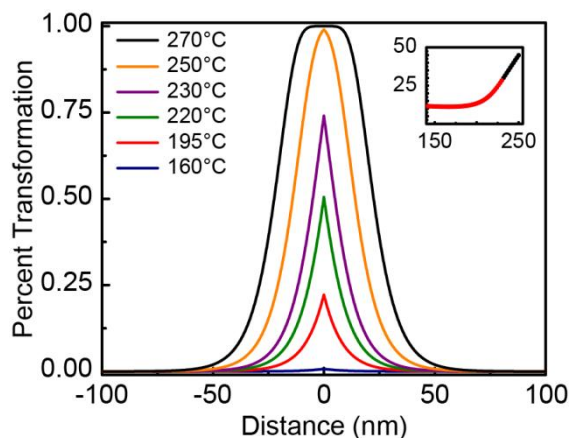


Figure 2.2.3 Temperature Dependence of eq. 2.2.5 with eq. 2.2.6

Decay Length

Figure 2.2.4 shows four different decay lengths (1 nm, 10 nm, 100 nm, and 1000 nm), along with the associated temperature decay profile. The solid lines represent the percent transformation, while the scatter plot is the temperature profile. The peak temperature and the dwell time are fixed (523 K and 6.9 ms). As expected, the maximum probability never changes. Figure 2.2.4 illustrates that as the temperature profile decays, the products concentration decays at a much faster rate than the original profile. The FWHM of the transformation is the intersection of the dashed (red) line with the solid lines; as can be seen, the FWHM values are significantly smaller than the associated decay lengths. This difference in FWHM and decay length arises from the final product concentration profile being the composition of a decaying function with a decaying profile. Assuming an exponentially decaying temperature, the percent transformation functional form shows an exponential of an exponential of an exponential. The first exponential is from the static solution to the first order chemical kinetics equation (eq 2.2.4); the second arises from the Arrhenius equation (eq. 2.2.3); the third arises from the temperature profile choice. Previously, it was hypothesized that the high resolution from TCNL results from the rapidly decaying temperature profile[68], but this is only part of the story. The sharp resolutions in TCNL result from the coupling between the chemical kinetics and the decaying profile.

The physical realization of variable decay lengths comes from the different ratios between the substrate and the silicon tips' thermal conductivities. For example, a greater substrate conductivity versus tip conductivity results in a greater decay length, whereas a greater tip conductivity results in a smaller decay length[94]. While there are no results about varying substrate conductivity in this thesis, this type of study offers ample potential for studying materials effects, especially when multi-layer films are considered since they can artificially cause smaller decay lengths.

While resolution is not one of the optimized components for this work, based on the discussion from these 3 sections, tuning resolution involves a hodgepodge of effects that include time, temperature, and the substrate's material properties. Despite these complexities, chemical kinetics plays a central role in determining the overall outcome.

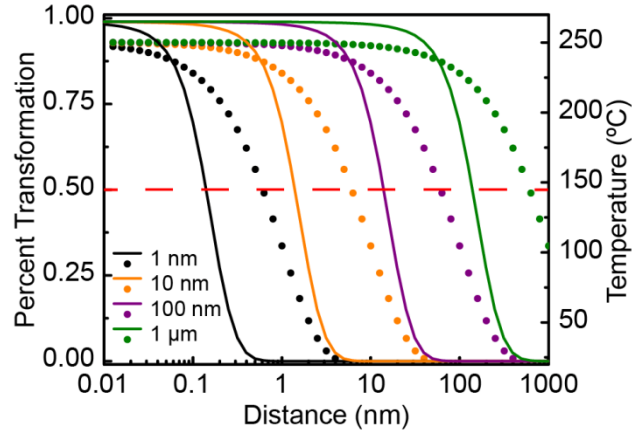


Figure 2.2.4 Decay length dependence of eq. 2.2.5 with eq. 2.2.6

2.2.2 Effects of Multiple Points

Having discussed the different tunable parameters, it is instructive to examine how multiple TCNL treated points interact with one another. It is clear from Figure 2.2.2 to 2.2.4, that if two points of contact are far enough apart, they have a negligible effect on each other. Bringing the two points closer until there is an overlap between the product profiles introduces secondary effects. Taking each point to be a separate event and using eq. 2.2.5, the first contact point introduces a product profile concentration as:

$$\frac{[P_1]}{[P_{tot}]} = 1 - e^{-A \cdot t_d \cdot s} \frac{R \cdot \left(T_0 + (T_{peak} - T_0) e^{-\frac{|x-x_1|}{\lambda}} \right)^{-\frac{E_a}{R}}}{R \cdot \left(T_0 + (T_{peak} - T_0) e^{-\frac{|x-x_1|}{\lambda}} \right)^{-\frac{E_a}{R}}}$$

(2.2.7)

where x_1 is the point of contact for the first event. The remaining percentage of unreacted substrate, $[R]$, is written as:

$$\frac{[R]}{[P_{tot}]} = e^{-A \cdot t_d \cdot \varepsilon} \frac{R \left(\frac{-E_a}{T_0 + (T_{peak} - T_0) \varepsilon^{-\frac{|x-x_1|}{\lambda}}} \right)}{\quad} \quad (2.2.8)$$

$[R]$ represents the substrate's spatial distribution with which the second contact event can interact. The product concentration from the second event is:

$$\frac{[P_2]}{[P_{tot}]} = e^{-A \cdot t_d \cdot \varepsilon} \frac{R \left(\frac{-E_a}{T_0 + (T_{peak} - T_0) \varepsilon^{-\frac{|x-x_1|}{\lambda}}} \right)}{\quad} \left(1 - e^{-A \cdot t_d \cdot \varepsilon} \frac{R \left(\frac{-E_a}{T_0 + (T_{peak} - T_0) \varepsilon^{-\frac{|x-x_2|}{\lambda}}} \right)}{\quad} \right) \quad (2.2.9)$$

where x_2 is the contact point of the second event. Combing eq. 2.2.7 and 2.2.9, the final product concentration for the substrate is:

$$\begin{aligned} \frac{[P_f]}{[P_{tot}]} &= \frac{[P_1]}{[P_{tot}]} + \frac{[P_2]}{[P_{tot}]} \\ &= 1 - e^{-A \cdot t_d \cdot \varepsilon} \frac{R \left(\frac{-E_a}{T_0 + (T_{peak} - T_0) \varepsilon^{-\frac{|x-x_1|}{\lambda}}} \right)}{\quad} - e^{-A \cdot t_d \cdot \varepsilon} \frac{R \left(\frac{-E_a}{T_0 + (T_{peak} - T_0) \varepsilon^{-\frac{|x-x_2|}{\lambda}}} \right)}{\quad} \end{aligned} \quad (2.2.10)$$

Eq. 2.2.10 demonstrates how two separate points of contact interact with each other. Figure 2.2.5 shows the interaction between two points of contact (decay length of 100 nm, T_{peak} of 523 K, t_d of 6.9 ms); the red and blue curves represent the product concentration for the individual events, and the black curve is the total interaction between both events occurring. There is an overlap region between the two events, corresponding to the interaction between the two events. While for any exponential decaying profile, there is always some overlap, the effects become negligible once the points are separated by a large distance. The inset shows the difference between the

interacting events and individual, non-interacting events; the fact that the difference is measurably non-zero demonstrates that the interaction between the tip and the substrate is *not* a convolution of events except at large distances. The true nature is akin to a Markov process.

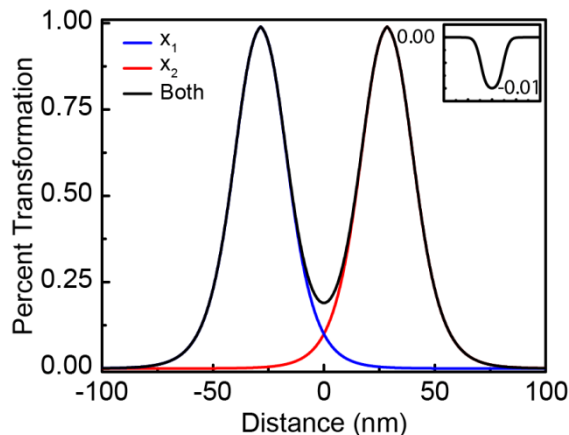


Figure 2.2.5 Interaction between two contact points described in eq. 2.2.10

2.2.3 Extension to a Moving Tip

The previous section showed that two nearby points of contact interact with each other. If a tip is in motion, there should be a compact mathematical relationship between the temperature profile and the product concentration. Assuming an instantaneous temperature profile, the temperature profile moves along the substrate simultaneously with the tip. As seen from the perspective of an individual point, the point is locally subjected to an initial temperature, T_0 ; after an infinitesimal time step later (Delta t_0), the same point is now subject to temperature T_1 for another infinitesimal time step (Delta t_1). Using the same approach developed in the previous section, the final percent product concentration after both time steps is:

$$\frac{[P_f]}{[P_{tot}]} = 1 - e^{-A \cdot \left(\Delta t_0 \cdot e^{\frac{-E_a}{R \cdot (T_0)}} + \Delta t_1 \cdot e^{\frac{-E_a}{R \cdot (T_1)}} \right)} \quad (2.2.11)$$

Continuing this process for time steps (Delta t_2 , Delta t_3 , ...) and the subsequent temperatures (T_2, T_3, \dots), the final product concentration is given by:

$$\frac{[P_f]}{[P_{tot}]} = 1 - e^{-A \cdot \sum_j \Delta t_j \cdot e^{\frac{-E_a}{R \cdot (T_j)}}} = 1 - e^{-A \cdot \int e^{\frac{-E_a}{R \cdot (T(t))}} dt} \quad (2.2.12)$$

where the final integral comes from assuming infinitesimal time steps. Finally, assuming a constant speed, eq. 2.2.12 can be re-written as:

$$\frac{[P_f]}{[P_{tot}]} = 1 - e^{-\frac{A}{v} \int e^{\frac{-E_a}{R \cdot (T(x_0, x))}} dx_0} \quad (2.2.13)$$

where v is the motion of the tip, x_0 represents the tip's position during translation, and x represents the point of interest.

While only 1-D expressions are examined here, similar results can be derived for 2 or 3-D. More complex formulas for different circumstances are derived from the analysis suggested in this and the previous section.

Eq. 2.2.13 is the starting point for understanding TCNL. As will be discussed in a subsequent section, there is great uncertainty in the determining the exact tip-induced temperature profile. Despite these difficulties, there is a lot to be gained however from assuming a temperature profile to learn how different parameters alter the technique. Using the same decaying exponential profile (eq. 2.2.6) with a decay length of 100 nm, eq. 2.2.13 is plotted in Figure 2.2.6 for four different speeds (1 $\mu\text{m/s}$, 10 $\mu\text{m/s}$, 100 $\mu\text{m/s}$, 1 mm/s). Looking at a fixed speed (10 $\mu\text{m/s}$), the functional dependence on the peak temperature is an S-shaped curve; this S-shape results from the increased reaction rate from an increased temperature. This simulation agrees with the previous sections

discussion of how temperature affects the static tip situation. At low (high) temperatures less (more) of the substrate undergoes the chemical transformation. While at higher temperatures there is a plateau in product concentration resulting from the finite reactant concentration, negligible amounts of the polymer transform at low enough temperatures.

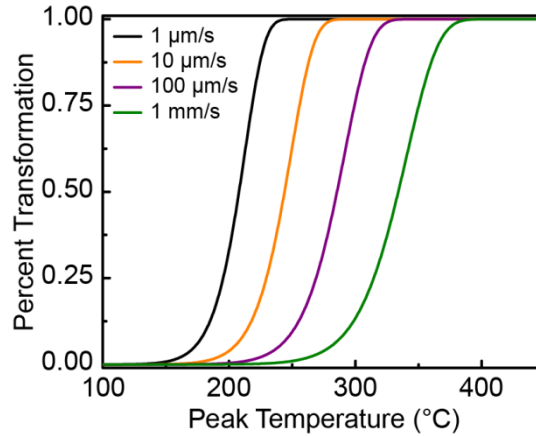


Figure 2.2.6 Plot of 2.2.13 with decay length of 100 nm

Effects of Speed on TCNL

Mirroring the discussion of varying dwell time, simulations of different speed conditions are shown in Figure 2.2.6. The signature S-curve typical to bounded growth equations is still present for all speeds, but the curves shift to the right with increasing speed. Comparing speed to inverse dwell time and mimicking the discussion in the dwell time section, allows us to conclude that for faster (slower) speeds, less (more) of the polymer undergoes the chemical transformation.

To see how speed evolves as a function of polymer transformation, eq. 2.2.13 can be re-written as:

$$v = \frac{A \cdot C}{\ln(1 - Pr)} \sim \frac{1}{\ln(1 - Pr)}$$

(2.2.14)

where $C = \int e^{\frac{-E_a}{R(T(x_0, x))}} dx_0$ and $Pr = [P]/[P_{tot}]$ is the percent transformation. Eq. 2.2.14 still maintains the temperature dependence through the C variable, but using a reference Pr_{ref} at reference speed, v_{ref} , different speeds can be computed as a function of percent transformation:

$$v = v_{ref} \frac{\ln(1 - Pr_{ref})}{\ln(1 - Pr)} \quad (2.2.15)$$

The interesting thing about eq. 2.2.15 is that it removes the complications of knowing an exact temperature profile, and replaces it with an experimentally determined reference percent transformation. We leave it to chapter three to discuss the limitations and difficulties in determining an exact Pr_{ref} .

Eq. 2.2.15 is plotted for a reference speed (10 $\mu\text{m/s}$) with a reference percent transformation (0.99) in Figure 2.2.7. The variants of eq. 2.2.15 for higher order reactions (2nd and 3rd order) are also shown in Figure 2.2.7. Interestingly, to span the percent transformation of 0.01 to 0.99, a first order reaction requires about 3 orders of magnitude for speed, whereas a second order and a third order reaction requires about 5 and 7 orders of magnitude respectively. The differences in the speed range provide a nice physical basis for determining whether a substrate patterned with TCNL is a first, second, or third order reaction.

There is also a rather esoteric relationship between speed and the order of reaction; taking a $Pr_{ref}=0.9$, the computed speed for a $Pr=0.99$ follows the relationship:

$$v = \frac{v_{ref}}{10^{n-1} + 1} \quad (2.2.16)$$

where n is the order of reaction. Figure 2.2.7 and eq. 2.2.16 tell us that as the substrate's order of reaction increases, the corresponding reaction becomes more immune to changes in speed. Therefore, higher order reactions are therefore better candidates for reliable high-speed TCNL patterning, since they are less affected by speed.

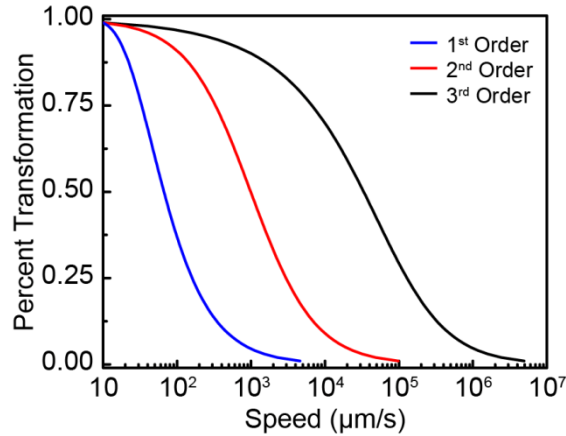


Figure 2.2.7 Plot of eq. 2.2.15 and higher order variants; the reference speed is 10 $\mu\text{m/s}$ and the reference transformation percentage is 0.99

2.3 Expanding to the Surface and 3-D

Eq. 2.2.13 provides the probability for the chemical transformation for a single point in space. To expand this equation to a surface or 3-D space, consider a volume of space which has been discretized into small pockets (see Figure 2.3.1 for a 2-D schematic). Eq. 2.2.13 describes the probability for each point, and a sum over the probability in the space of interest computes the number of sites undergoing the entire reaction:

$$N = \sum_i Pr_i \tag{2.3.1}$$

Where N is the number of sites that have undergone the reaction, Pr_i is the probability of transformation at site i , and the summation is over available sites in the volume of interest.

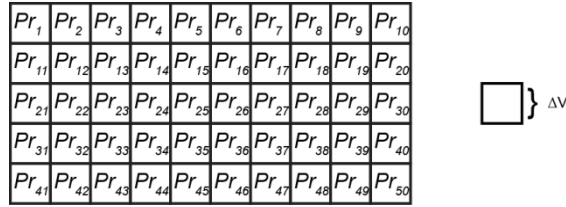


Figure 2.3.1 Schematic for eq. 2.3.1

Dividing N by the total number of available reactive sites gives:

$$\frac{N}{N_{tot}} = \frac{\sum_i Pr_i}{N_{tot}} = \frac{\sum_i Pr_i}{\sum_i 1} \quad (2.3.2)$$

Where N_{tot} is the total number of available sites. Finally, since each site occupies a fixed volume, delta V , the above can be re-written as:

$$\frac{N}{N_{tot}} = \frac{\sum_i Pr_i \cdot \Delta V}{N_{tot} \cdot \Delta V} = \frac{\sum_i Pr_i \cdot \Delta V}{\sum_i \Delta V} = \frac{\int \int \int Pr \, dx \, dy \, dz}{\int \int \int dx \, dy \, dz} \quad (2.3.3)$$

Where the integral comes from assuming a continuous distribution of reactive sites. Here x and y are in the plane of the surface and z is normal to the surface. To compute the effect on a local region of a surface, the z integration can be ignored:

$$\frac{N}{N_{tot}} = \frac{\int \int Pr \, dx \, dy}{\int \int dx \, dy} \quad (2.3.4)$$

For this work, we ignore the y -integration since our patterning technique (see Figure 2.3.2), places consecutive zig-zag lines close to one another ($<125/2$ nm~FWHM for the polymer substrate). This allows us to proceed with using equations 2.2.15.

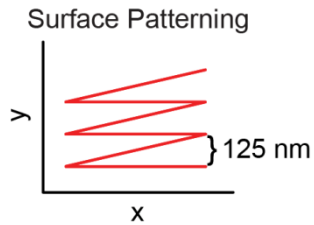


Figure 2.3.2 Rastering image to pattern a substrate

For 3-D body effects, the z -dependence *cannot* be ignored, and it will be further discussed in chapter 4.

2. 4 Discussion of the Assumed Temperature Profile

The exact form for the temperature profile is incredibly difficult to compute. There is limited evidence to suggest that the heat equation holds down to these length scales[95]. There are some works which assume the heat equation holds, but often boundary conditions are ignored, such as convective cooling[96], calling into question whether the results show the validity of the heat equation. Solutions to the heat equation are boundary condition dependent and because of sub-continuum effects in the tip, these conditions are a feat to compute. Given the length scales, the Boltzmann Transport equation for the phonon distribution provides a more accurate solution[97]. Moreover, the literature agrees the main form of conduction is through the air[98], and while this is undoubtedly true, computing this effect on the temperature profile is also difficult and mostly done with Monte Carlo simulations[99] . There are also other effects to consider here, such as the glass transition temperature and visco-elastic behaviors[52].

Since there is uncertainty in the temperature profile, we make an approximation based on some previously attained results. The assumed profile will be the same one used throughout this chapter, specifically the form in eq. 2.2.6. The motivation for this profile comes from the fact that if the static heat equation holds, the Laplacian form demands an exponential decay. Previous results suggest that it is possible to attain a 12 nm resolution moving at 2 mm/s on a similar polymer substrate[68], and we use this result to determine the decay length. Assuming the tip's radius of curvature is 20 nm, the time scales associated with this speed is $20 \text{ nm}/(2 \text{ mm/s}) \sim 10 \text{ } \mu\text{s}$. Plugging this into eq. 2.2.4, the computed temperature is about 650 K to attain 99% conversion. Using this as the peak temperature in eq 2.2.6 and substituting this temperature profile into eq 2.2.13, comparisons of different decay lengths (1 nm, 10nm, 50 nm, 100nm, 1000nm) shows that a decay length of 100 nm was closest to the 12 nm resolution at 1 mm/s. We use this form for our temperature profile throughout this work.

2.5 Final Word

The intent of this chapter was to help develop the intuition and some of the basic math, chemistry, and physics for TCNL's governing mechanisms. Using a chemical kinetics model and working with a temperature profiles, it was shown how different parameters (decay lengths, peak temperature, and time scales) affect the mechanisms. The analytical methods necessary for predicting how more complicated situations will react were demonstrated. The model and results discussed in this section will be used for the remaining chapters.

CHAPTER 3

EXPERIMENTAL MODELING OF SURFACE REACTIONS WITH TCNL

3.1 Introduction

ThermoChemical NanoLithography is a nano-scale lithographic technique that combines thermally activated chemical transformations with a spatially localized temperature profile induced by a thermal cantilever. Researchers have patterned with TCNL to site specifically attach proteins and other biomolecules[64], reduce graphene oxide to graphene[65], convert hydrophobic materials to hydrophilic[69], crystallize ceramic materials[67], and to pattern semi-conducting organic polymers[70]. While these works have demonstrated the impressive range of materials suitable for TCNL, there has been little attempt to quantify and model the technique. Even though there is much to gain from describing TCNL with a chemical kinetics model, it is equally important to verify and prove the assumptions and equations experimentally.

Chapter 2 was dedicated to developing the chemical kinetics model describing the transformation taking place at the tip-surface interface; the next two chapters are dedicated to experimental verification of the equations derived in chapter 2. The key differences between this chapter and the next is that here we focus on surface effects, ignoring the heat penetration into the sample. To study only surface effects, we couple the previously described thermally activated polymer with a fluorophore and fluorescent microscopy; because of the polymer substrate is crosslinked, the fluorophore should only attach at or very near the surface. Using this method, the basic principles derived in chapter 2 will be verified, and then we apply the model to design patterns with controlled chemical concentration variations. We start with a brief review of the electric and mechanical properties of the thermal cantilevers.

3.2 Review of Thermal Cantilevers

The thermal cantilevers used throughout this work have an integrated heater built above the tip; when biased with a voltage, these semi-conducting cantilevers heat due to resistive heating. While there is ample literature on the thermal and electric properties of thermal cantilevers[92, 100-102], the basic concepts, terms, and properties are reviewed in this section. All tips used in this work were fabricated by Professor William P. King's lab at University of Illinois at Urbana Champaign.

3.2.1 Thermal Cantilevers: Fabrication and Design

The cantilevers are fabricated with ion implantation methods to introduce contrasting doping levels. The cantilevers are etched from a silicon wafer; the wafer comes with a native doping concentration of about $10^{14} /\text{cm}^3$. The legs are ion implanted with high doping levels (Phosphorous, n-type $10^{20} /\text{cm}^3$) causing them to be highly conductive, and the integrated heater region above the tip is doped with low levels (10^{17} - $10^{18}/\text{cm}^3$) (see Figure 3.2.1)[100]. While the doped legs are highly conductive, the heater region is more resistive, and as a result of this doping contrast most of the electric power (~90%) is dissipated in the low doped region[51]. This influx of energy results in the localized heating of the low doped region; because of this localized heating, the low doped region is referred to as the heater. Finally, the tips are sharpened with an oxidation procedure, described in the literature[103].

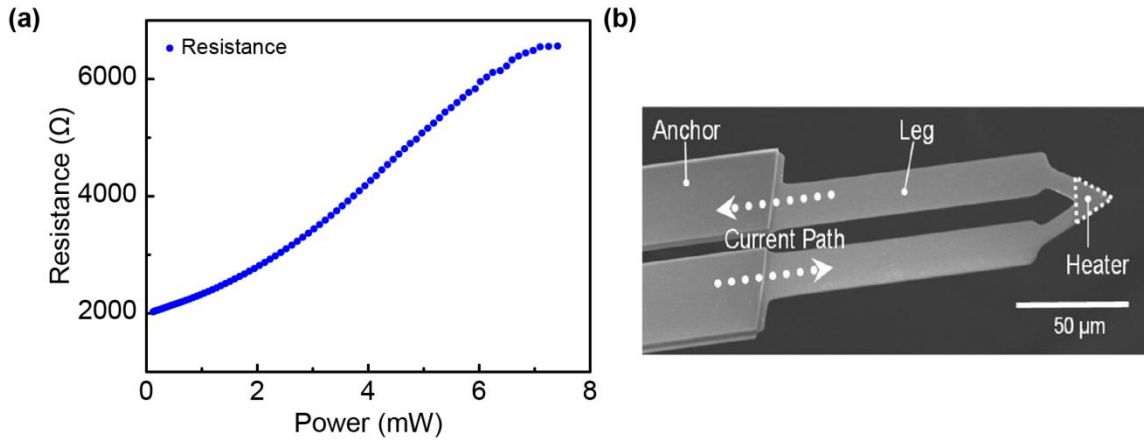


Figure 3.2.1 (a) Graph of thermal cantilever resistance versus power dissipated across the cantilever; 90% of the power is dissipated in the heater region. (b) SEM image of a thermal cantilever. Image[104] reprinted with copyright permission © 2008 Taylor and Francis.

The fabricated cantilevers have a reported stiffness of 0.1-1N/m. The resonant frequency is approximately 60-70 kHz; the length and thickness are $\sim 150 \mu\text{m}$ and 600 nm respectively[92, 105]. The tip height is $\sim 1.5 \mu\text{m}$, and the radius of curvature is $\sim 20 \text{ nm}$ [92]. The mechanical properties are important since they can tune different thermo-electrical properties, such as thermal constriction[101].

3.2.2 Electronic Properties

The heater region dissipates most of the power because of the doping contrast. As in most metals, the resistance in the silicon tip has a positive temperature coefficient[92] because of the increased scattering from phonons[106]. Above a certain temperature, the temperature coefficient switches to negative values because the increased temperature causes the intrinsic carriers to dominate conduction[107]; the temperature, at which this switch occurs, is commonly referred to as the thermal runaway. Measurements with Raman Spectroscopy reveal that the thermal runaway occurs at about $550\text{-}600 \text{ }^\circ\text{C}$ in the heater region[92]. Raman spectroscopy also shows that the integrated heater temperature is linear in both cantilever resistance and dissipated power and because of the consistency

of the thermal runaway temperature, both the resistance and power can be used to estimate the heater temperature to about 10% accuracy.

The temperature at the tip-surface interface is reported to be less than the heater region; this results from thermal transport down the tip and sub-continuum effects. Depending on the thermal properties of the substrate, the tip-substrate interface temperature is ~0.6-0.1 of the heater region's temperature; more thermally conductive surfaces typically have a lower efficiency (~0.1 for Graphene[90]), while substrates with a lower thermal conductivity have higher values (0.3-0.6 for organic substrates[69, 108]). This loss is referred to as the tip efficiency[108].

3.3 ThermoChemical NanoLithography: Temperature Dependence

The polymer substrate is the same one detailed in chapter 2. The chemical structure of the polymer, (poly((tetrahydropyran-2-yl N-(2-methacryloxyethyl)carbamate)-co-(methyl 4-(3-methacryloyloxypropoxy)cinnamate))) is shown again Figure 3.3.1; for convenience in this chapter, we refer to the spin case polymer substrate as the polymer or polymer substrate. The polymer was synthesized by Professor Seth R. Marder's lab at Georgia Institute of Technology. Synthesis and chemical preparation of the polymer is described elsewhere[64, 109], but some key features are discussed here.

The polymer has a protected functional amine group; when heated, the protection group dissociates, leaving behind an exposed functional group to which various complementary chemistries can be attached[64]. The dissociated groups (gaseous CO₂ and dihydropyran) are volatile enough that more than likely they diffuse away[58]. To ensure the polymer substrate structure remains intact, the polymer's glass transition temperature is increased with an increased UV induced cross-linking between the polymer's cinnamate side chains[64].

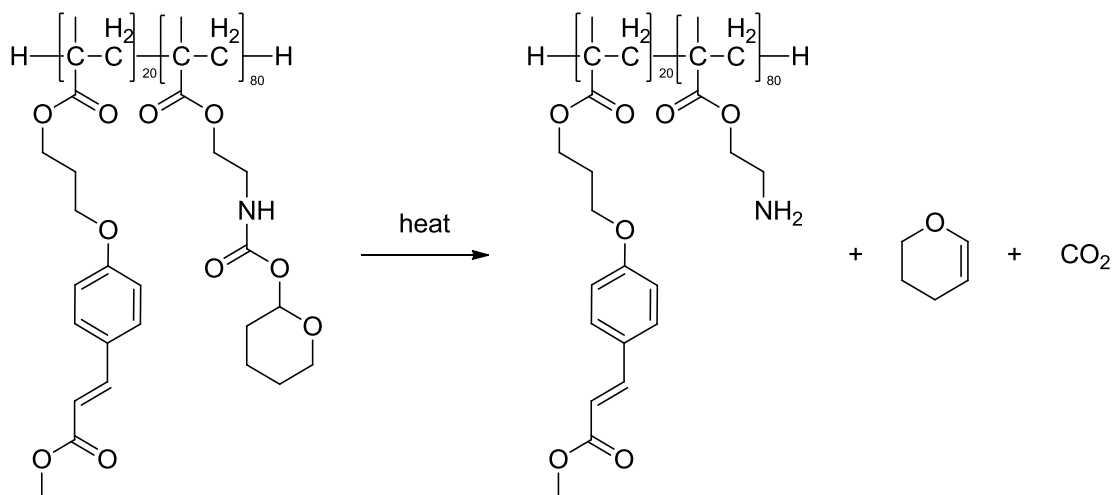


Figure 3.3.1 Chemical structure of polymer.

3.3.1 Methods and Description of Experiments

A typical experiment to test the model's validity is shown in Figure 3.3.2a, where an array of squares tests the validity of the chemical kinetics model; each square is written at a fixed heater temperature. The numbers indicate typical values for power dissipated across the cantilever. As explained in section 3.2.2, the power dissipated across the cantilever is approximately linear to the heater temperature, and so the heater temperature in each square is maintained through a computer feedback system which monitors and adjusts the power dissipated across the tip. The minimum change in power is limited by Johnson Shot noise[101, 110]. Figure 3.3.2b shows the polymer before it is patterned. Because of the spin-coating and thorough cleaning, the polymer surface is flat and smooth. After the patterning, noticeable changes in the topography can be seen in Figure 3.3.2c. At higher temperatures, the surface starts to show an enhanced topographic change, specifically a drop in the surface height caused by the material loss from the chemical transformation. At lower temperatures, there is less material loss since as we will discuss less of the polymer undergoes the chemical transformation. The correlation between the height and temperature is fairly difficult to accurately reproduce

for this polymer; as a result, we focus on surface effects. We take the change in topography as qualitative evidence that the polymer has undergone a transformation. Z-penetration and 3-D conversion are discussed in the next chapter.

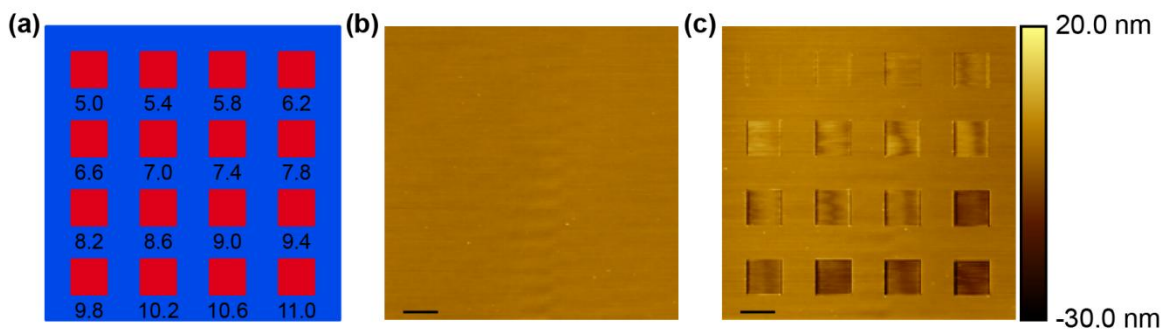


Figure 3.3.2 (a) Typical experiment to test the chemical kinetics model. The numbers indicate typical dissipated powers for these experiments. (b) AFM image of the polymer substrate prior to patterning. (c) AFM image of the pattern detailed in (a).

While AFM measurements are suggestive that TCNL has induced some form of change, fluorescent microscopy will semi-quantitatively verify the chemical nature of the transformation. By attaching an amine reactive fluorophore, the presence of a localized fluorescent signal both confirms the existence of exposed amines and provides a mechanism to analyze how temperature affects the TCNL process. Fluorescent microscopy is an effective method for semi-quantitatively analyzing chemical concentrations since the emission intensity is linearly proportional to the concentration³. Other methods, such as XPS or Friction Force Microscopy (FFM), allow for a similar analysis to be done, but each has its drawback. XPS, for example, is tedious and would

³ Special care needs to be taken to quantitatively use fluorescent microscopy because fluorescence can exhibit non-linearity in concentration, such as quenching.

be difficult to demonstrate designing patterns[111]; analysis of FFM signals would be difficult since there may not be a linear relationship between the friction measurement and the concentration (there is also the interaction between topography and the friction measurements which may alter the results)[112]. Fluorescent microscopy provides an efficient, straightforward method to quantifying chemical concentrations.

After the patterns are made, a fluorophore (here NHS-Dylight 633, 25 nM in DMSO), is used to label the patterned areas. The bound dye concentration relates to the exposed amine concentration. In areas with a greater concentration of exposed amines, more dye attaches. When imaged with fluorescent microscopy, areas with a more dye emit with a greater intensity and this produces a brighter signal. Dimmer signals correspond to less dye and lower concentrations of exposed amines.

The dye concentration is kept low to reduce effects from quenching resulting from closely packed dye molecules and to insure an approximately linear relationship between the bound molecules and the amine concentration. This former effect is a known phenomenon, variations of which are used in other microscopy techniques, such as FRET[113-114]. The latter comes from the fact that the concentration of exposed amines may be substantial enough that steric hindrance between dye molecules prevents proportional labeling of the amine concentration. Reducing the dye concentration alleviates this issue because the dye concentration will be proportional to the amine concentration at low concentrations. This last fact comes treating the reaction between the dye and the exposed amines as an equilibrium equation:

$$K_{eq} = \frac{[D] \cdot [SA]}{[D - SA]} \tag{3.3.1}$$

where $[D]$ is the fluorophore's solution concentration, $[SA]$ is the concentration of exposed surface amines, and $[D - SA]$ is the surface concentration of bound fluorophore. By maintaining a low dye concentration and assuming the amount of dye in the solution

is much greater than the bound dye concentration, the number of attached dyes should approximately be proportional to the amine concentration.

The fluorescently labeled and imaged pattern corresponding to the sample in Figure 3.3.2 is shown in Figure 3.3.3. The orientation is the same as the experimental setup in Figure 3.3.2. We observe that qualitatively there is agreement between the chemical kinetics model and the fluorescent signal. For higher temperatures, the intensity signal is brighter versus the lower temperature patterns; this increased signal results from a greater fluorescent dye presence which indicates a greater concentration of exposed amines. Lower temperatures have less dye, and therefore indicate a lower concentration of amines. The last row also shows the intensity levels start to level off and form the same plateau, consistent with the trend seen in Figure 2.2.6.

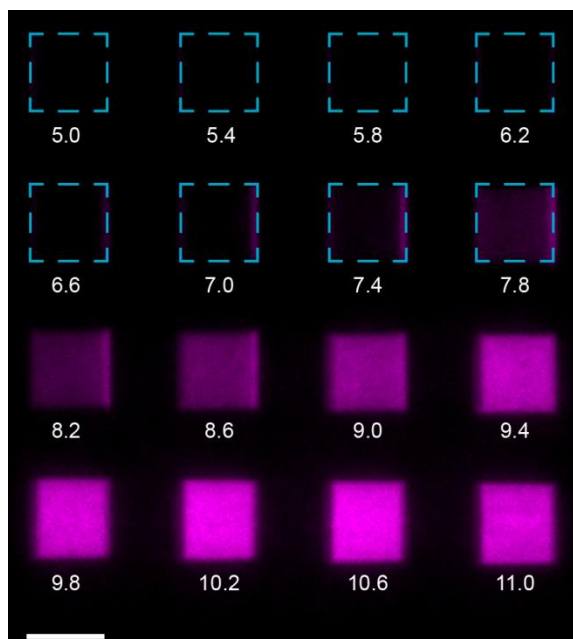


Figure 3.3.3 Fluorescent image from the experiment shown in Figure 3.3.2

To compare this result with the model, there is a standard procedure[115] to follow; Fig 3.3.4 shows the steps. Briefly, first a background image is taken to correct for any uneven illumination resulting from the fluorescent lamp source; this background divides the raw data image to produce an even illumination field. Next the intensity levels for each square are measured; in order to avoid edge issues, the measurements must be inscribed in each square. For example, for a 5 x 5 μm^2 square, a 3 x 3 μm^2 concentric square was used; this is portrayed in Figure 3.3.4c with the inscribed cyan square. To correct for non-specific binding and for standard noise from images, the intensity levels of unpatterned areas were measured. Finally the relative intensity levels were calculated using the following formula:

$$I_{rel} = \frac{I_{measured} - I_{background}}{I_{plateau} - I_{background}} \quad (3.3.2)$$

where I_{rel} is the relative intensity levels of the square intensity, $I_{measured}$ is the measured flattened intensity of the patterned square, $I_{background}$ is the average background intensity resulting from non-specific binding and noise in the camera, $I_{plateau}$ is the average intensity of the plateau region (for Figure 3.3.3 it is the average intensity of the squares in the bottom row).

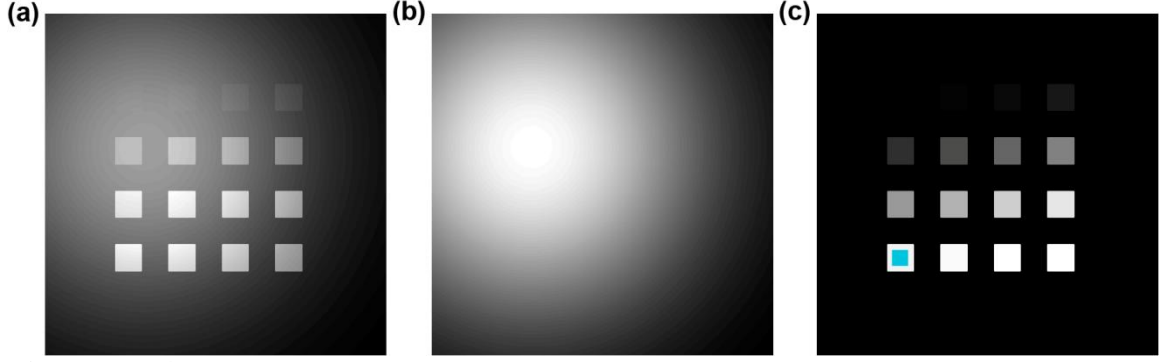


Figure 3.3.4 (a) Theoretical fluorescent image measured with an uneven illumination field. (b) Theoretical background image indicating the uneven illumination field. (c) Corrected fluorescent image resulting from dividing (a) by (b). The cyan square indicates an inscribed to measure a squares intensity level.

The relative intensity levels are compared against the corresponding relative version of eq. 2.2.13:

$$\frac{1 - e^{-\frac{A}{v} \int \epsilon R \left(T_o + (T_{psak} - T_o) e^{-\frac{|x|}{\lambda}} \right) dx}}{1 - e^{-\frac{A}{v} \int \epsilon R \left(T_o + (T_{max} - T_o) e^{-\frac{|x|}{\lambda}} \right) dx}} = \frac{-E_a}{-E_a} \quad (3.3.3)$$

where T_{psak} is the peak temperature (K), T_o is room temperature (K), lambda is the decay length (100 nm), T_{max} is the peak temperature (K) for the square with the maximum heater temperature in the plateau. The peak temperature is calculated through:

$$T_{psak} = T_o + \eta \cdot (T_{heater} - T_o) \quad (3.3.4)$$

where eta is the efficiency parameter discussed previously and T_{heater} is the heater temperature. A reliable method for computing T_{heater} is described in the literature[51, 92].

To fit the model with the relative intensity, eta and E_a are taken as fitting parameters. Eta is load dependent and varies from tip to tip depending on the size and

radius of curvature; the calculations[116-118] for E_a from TGA showed a significant range and TGA comparisons to data are fairly sensitive to small changes in E_a (see supplementary materials of reference[58]). Figure 3.3.5 shows good agreement between the model and the experiment. This result confirms that a chemical kinetics models the technique, and will provide the basis for spatially controlling chemical reactions with TCNL.

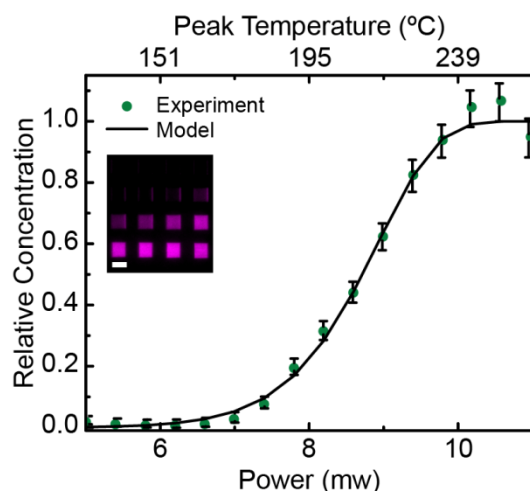


Figure 3.3.5 Comparison of the inset's measured intensity (eq. 3.3.2) (inset same as Figure 3.3.4) with the chemical kinetics model (eq. 3.3.3). There is good agreement between the experiment and the model.

Two key assumptions embedded in eq. 3.3.3 are the form of the temperature profile and neglecting the polymer motion resulting from heating. In chapter 2, the temperature profile choice is discussed at length, and the final profile choice comes from matching some previous experimental results with a given decay profile. The latter issue is justified because the glass transition temperature is increased through the enhanced cross-linking between polymer components. It is noteworthy, however, that research has suggested that organic thin films show a decreased glass transition temperature from bulk material[119-120]. The differences are often small.

This model works up to temperatures below the polymer glass transition and decomposition temperatures. If higher temperatures are applied, the labeled polymer starts to show a measured decreased in intensity signal, followed by a significant drop off in signal. The first effect is probably from a combination of the glass transition temperature effects and some polymer decomposition. The second drop off can be attributed solely to the polymer decomposition since AFM measurements indicate a height difference in the patterned areas consistent with the film thickness.

3.3.2 ThermoChemical NanoLithography: Speed Dependence

To test the dependence on speed, two experiments were designed. The first experiment follows the same procedures as in the previous section but with four versions of the patterns each at different speeds (1 $\mu\text{m/s}$, 10 $\mu\text{m/s}$, 100 $\mu\text{m/s}$, 1 mm/s). The labeling and quantification are the same, and the result is shown in Figure 3.3.6. The same S-shaped curve is seen for all four speeds, but there is a corresponding shift of the curve to the right for increased speeds. This shift comes from the fact that faster speeds expose the polymer to the temperature profile for less time, resulting in a decreased rate of reaction. This shift is also predicted and discussed in chapter 2 (Figure 2.2.6).

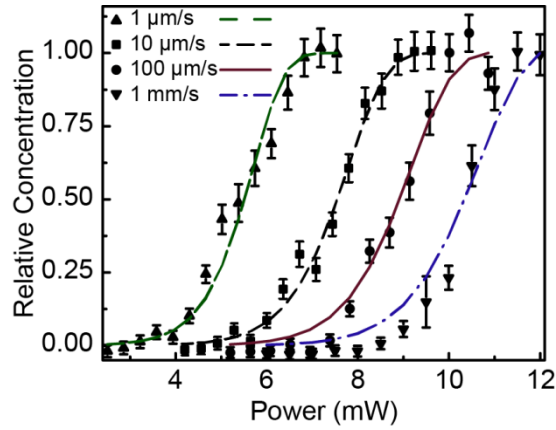


Figure 3.3.6 Comparison of the model with four different speeds (1 $\mu\text{m/s}$, 10 $\mu\text{m/s}$, 100 $\mu\text{m/s}$, 1 mm/s). The results show the curves shift to the right as predicted in chapter 2.

The second experiment fixes the heater temperature and varies the speed across approximately four orders of magnitude. The experiment and results are shown in Figure 3.3.7. As the speed increases, the relative percent of transformation decreases. The model predicts an exponential decay with respect to inverse velocity, and the measured data fits this prediction well.

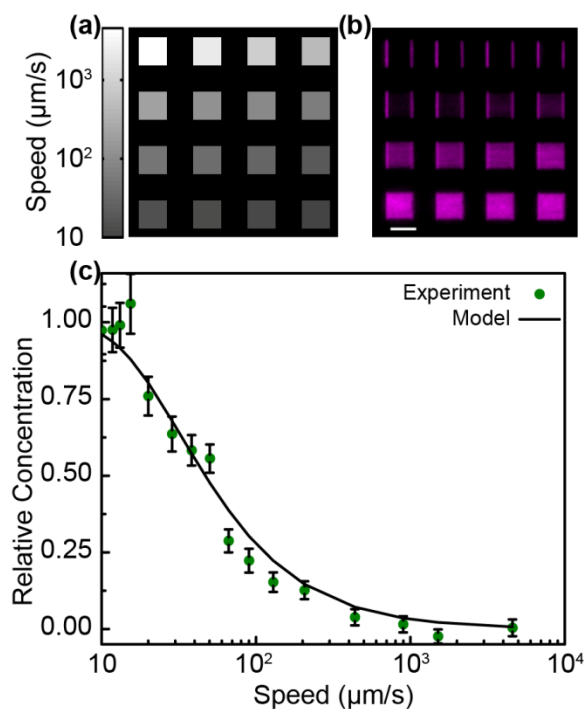


Figure 3.3.7 (a) Experimental setup in which the temperature is fixed, but the speed is varied across 3 orders of magnitude. (b) Fluorescently labeled image corresponding to the experiment in (a). (c) Comparison of the measured fluorescent intensity to the chemical kinetics model with a fixed temperature and varying speed.

Figure 3.3.7 shows that for a fixed temperature, in order for speed to span the chemical transformation's range, approximately 3.5 orders of magnitude of speed are needed. This agrees with the predictions made in chapter 2, and interestingly, this speed dependence provides more credence to a first order chemical kinetics model being applied to this chemical transformation. As discussed in chapter 2, the chemical kinetics model predicts that 2nd and 3rd order reactions require a greater range in the speed (5 orders of magnitude for 2nd, and more than 7 for 3rd order); if the polymer were not a first order reaction, it would exhibit a different range in speed than the observed range.

The key assumption for these experiments is that the temperature profile minimally changes at different speeds. We justified this with our own calculations in chapter 2, which showed the temperature profile should reach static equilibrium near

instantaneously; additionally, other temperature profile time scale calculations[91] are below the time scales associated with the tip radius and speeds up to ~10 mm/s.

The results shown in this section are the basis for using speed to control chemical reactions as will be discussed in a subsequent section.

3.3.3 Controlling Chemical Reactions with Temperature

In section 3.3.2, it was shown how to model TCNL with chemical kinetics assuming a fixed speed and variable temperature. In this section, the model is applied to control the relative chemical transformation and produce intended chemical concentration gradient profiles at fixed speeds. The basic procedures are outlined in Figure 3.3.8, where the starting point is a calibration curve to find the fitting parameters η and E_a ; these are measured through the methods suggested in section 3.3.2. The designed pattern (here a linear gradient) is translated into a grayscale, which relates each intensity value to a percent transformation (i.e. from about 0 to 1). Coupling eq. 3.3.3 with the measured E_a backs out the peak temperature field for a given relative concentration, and a new map detailing the peak temperature is drawn. Using eq. 3.3.4 with the measured η determines T_{heater} (step not shown), and using the methods described in the literature, T_{heater} translates into a power map. Spatial distribution of the power controls the chemical concentration profiles to produce the initial design. Other parameters, such as load and speed, should be the same as those used to measure E_a and η .

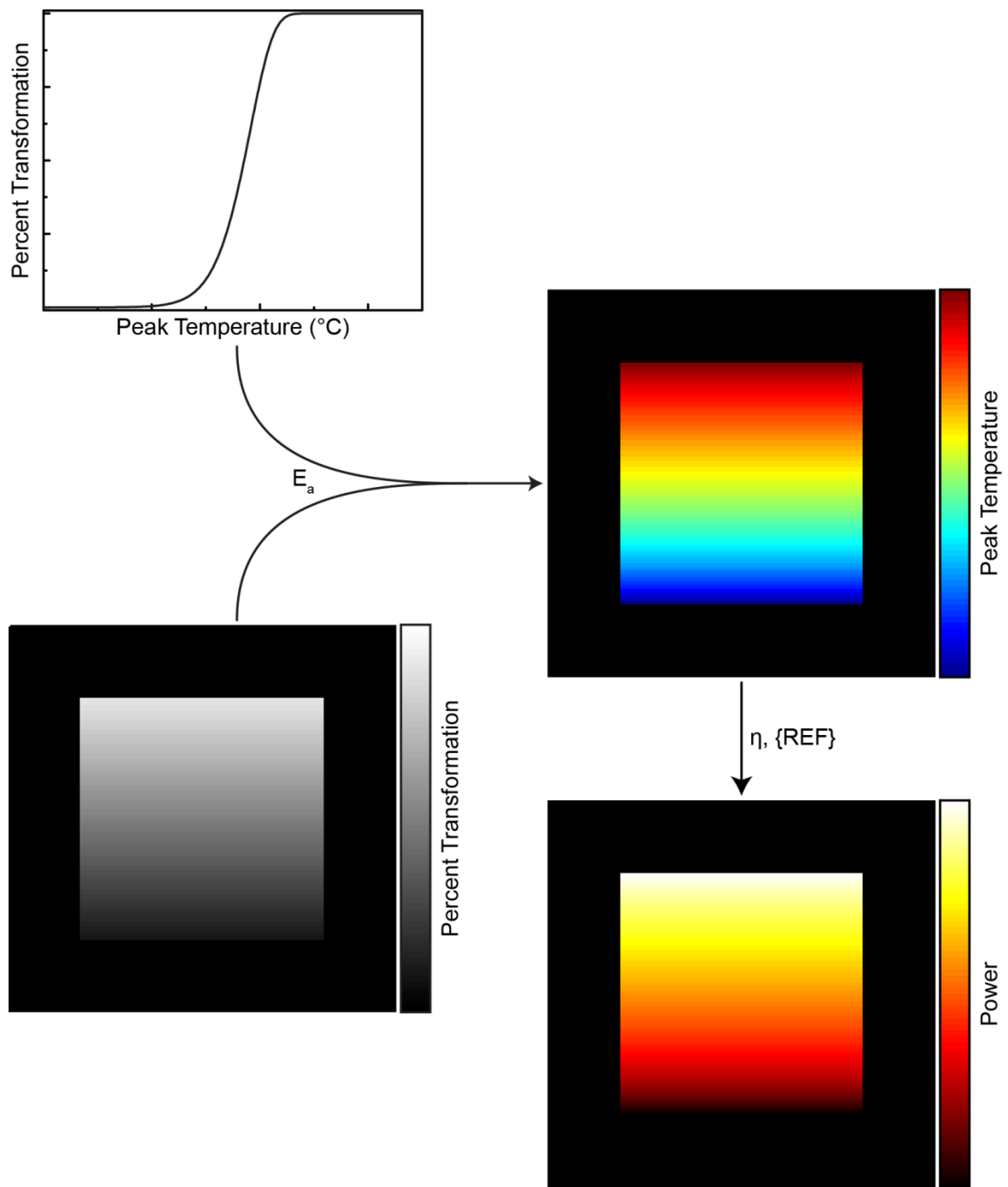


Figure 3.3.8 Schematic explaining how to create controlled chemical concentration profiles with TCNL.

An example of one set of designed patterns is shown in Figure 3.3.9. The three designed forms vary between 0.2 and 0.8 relative values, and they have three different forms: a sinusoid, a linear carrot-top, and a cubic carrot-top. There are also a set of squares written off to the side which act as a normalizing intensity value. After being patterned, the sample is labeled with a fluorescent dye and same procedures for flattening and computing the relative intensity values described previously are used to quantitatively compare the fluorescent results with the intended profile. The results, shown in Figure 3.3.9d, compare well with the intended profiles, and variations along the profiles are smooth and measureable. This result verifies that coupling TCNL with a chemical kinetics model can design and create controlled chemical concentration profiles.

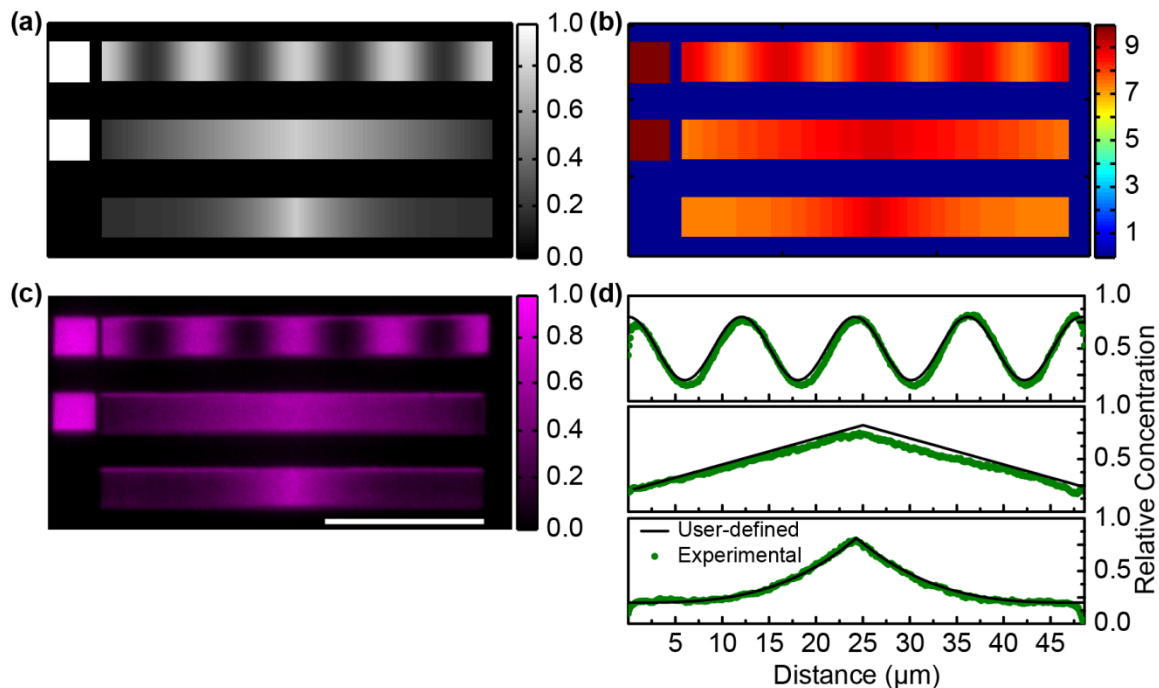


Figure 3.3.9 (a) User-defined concentration profile. (b) Map describing the power distribution as a function of position. This is obtained by following the procedures displayed in Figure 3.3.8 (c) Fluorescent image corresponding to the pattern defined in (a) and (b). (d) Plots comparing the user-defined (intended) concentration profiles against the experimentally measured values seen in (c).

Typical results show about a 5-10% percent deviation from the intended profiles; the reason for this deviation can be attributed to the fact that there may be some small difference in film thickness from the calibration step to the designed patterns. The film thickness affects the peak temperature (T_p) because the underlying substrates thermal properties (here silicon) start to manifest at thin films. The deviations can also be attributed to the normalization value; if this is off by a small amount it can affect the range of the relative concentration results. The deviations in the normalization values likely arise from slight variations in film thickness and shot noise in the thermal cantilevers.

The results shown in Figure 3.3.9 demonstrate the ability to control concentration profiles in 1-D. Figure 3.3.10 show the ability to extend this into 2-D concentration profiles. In these cases, two images are converted from a grey scale image to a 2-D spatial power map. Instead of having the tip move continuously across the substrate, the tip remains at a pixel for a fixed period of time with the power being set by the spatial power map. Instead of using eq. 3.3.3, a static version backs out the peak temperature:

$$Pr = 1 - e^{-A \cdot t_d \cdot e^{\frac{-E_a}{RT_{peak}}}} \quad (3.3.5)$$

where Pr is the grey scale value and t_d is the fixed dwell time (here 50 ms). There should be some difference between the two methods, but since the intent is to show approximate control in 2-D, this suffices. Figure 3.3.10 shows the results of two images, da Vinci's *Mona Lisa* scaled down to $\sim 30 \times 40 \mu\text{m}^2$ and a $44 \times 34 \mu\text{m}^2$ replica of Ansel Adams' *Rose and Driftwood*. The pixel spacing is about 125 nm which is optimal for fluorescent microscopy (otherwise diffraction would blur the image too much⁴) and this

⁴ An excellent example of this is given in chapter 4

125 nm spacing is also about the FWHM measured on this polymer substrate (see section 3.3.4).

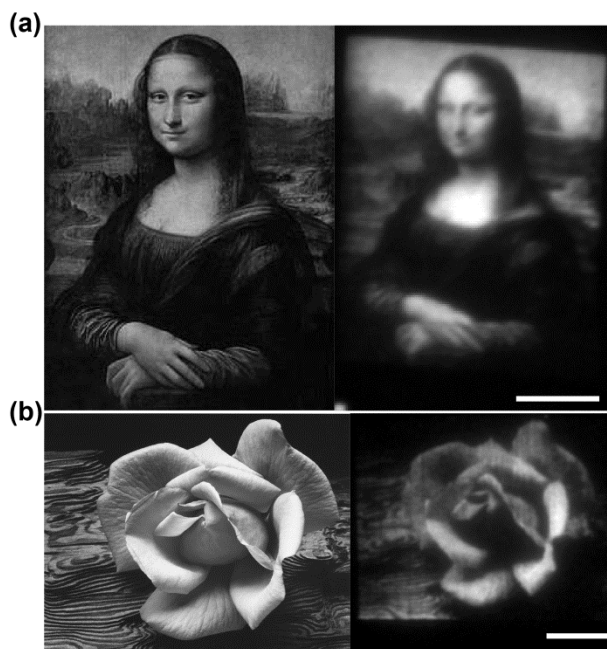


Figure 3.3.10 (a) (Left) Original *Mona Lisa* image; (Right) $\sim 30 \times 40 \mu\text{m}^2$ reproduction of the *Mona Lisa* (commonly referred to as the *Mini Lisa*). (b) (Left) *Rose and Driftwood*, 1932, photograph by Ansel Adams, copyright 2012 The Ansel Adams Publishing Rights Trust. (Right) $44 \times 34 \mu\text{m}^2$ reproduction of *Rose and Driftwood*.

The results shown in this section demonstrate the ability to use TCNL for designing and creating controlled variations in the chemical concentration by tuning temperature. The assumptions made for producing these patterns are the same as in section 3.3.1. Interestingly, the techniques and methods described in this section can be applied to other molecules, such as proteins or DNA; however, there are differences. For example, to account for differences in binding and packing densities, the first step calibration curve needs to be done with the final attached molecule.

3.3.4 Resolution Measurements

The Full Width at Half Maximum (FWHM) determines the length scales down to which control holds, and Figure 3.3.11 shows the FWHM measurements of several lines at different temperatures. The measurements were made with an AFM using Friction Force Microscopy (FFM); FFM is capable of detecting changes in surface chemistry because the capillary interactions between the tip and substrate are enhanced or diminished depending on the surface hydrophilicity[112, 121]. In particular, amine exposed areas are more hydrophilic than the protected polymer[109], and the corresponding FFM measurements show an increased interaction in the patterned areas.

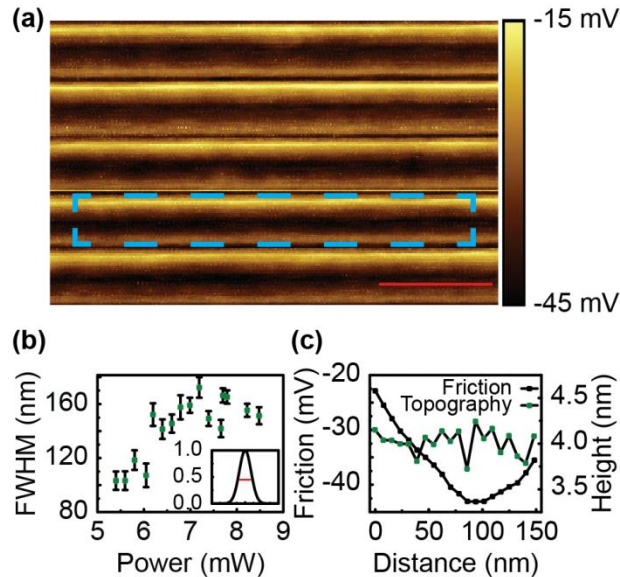


Figure 3.3.11 (a) Friction measurement of consecutive TCNL patterned lines spaced by 125 nm. Cyan square indicates the average profile shown in (c); scale bar (red) is 1 μm. (b) FWHM measured with FFM for lines written at different powers. (c) Profile showing a smooth variation of the friction signal over a topographically flat area. The friction shows a measureable change over distance of 20 nm.

The measured resolution is about 150 nm, which is larger than previously reported on the same substrate[64]. The difference may arise from the film thickness:

previously the films were up to 150 nm thick and the films used for this work were ~50-70 nm thick. The measurement styles were also different. Previously, bound proteins were used as the standard, but because of packing densities and efficiency loss from the multiple layers of chemistry to attach the protein, the resolution could artificially be increased⁵. FFM is a more intimate method that will exhibit a higher sensitivity.

Figure 3.3.11a shows an experiment in which the two different temperatures were written at a spacing of 125 nm. As can be seen in Figure 3.3.11c, the friction profile shows a measureable change over distances of ~20 nm. This represents the lowest bound down to which TCNL controlled reactions work. The flat region over which the friction is measured indicates that the measurements are done without having the friction convolve with the local topography.

3.3.5 Controlling Chemical Reactions with Speed

The previous section demonstrated how to control chemical concentrations by tuning temperature; this section is dedicated to showing controlled chemical concentrations realized using a spatially varying speed. The procedures for doing this are similar to those for temperature, and the main difference is the governing equation, which for speed is given by:

$$v = v_{ref} \frac{\ln(1 - Pr_{ref})}{\ln(1 - Pr)} \quad (3.3.6)$$

where v is the calculated speed, Pr_{ref} is a measured reference percent transformation done at fixed temperature and a reference speed, v_{ref} , and Pr is the variable percent transformation.

⁵ By resolution, we mean resolving power; increased resolution refers to smaller lengths.

The first step is to select values for Pr_{ref} and a v_{ref} . The optimal choice is a $Pr_{ref} \sim 0.50$, as will be explained later. The value for v_{ref} can be any reasonable value; the value used here is 10 $\mu\text{m/s}$. A calibration plot similar to the one discussed in section 3.3.1 with the selected v_{ref} determines the eta and E_α values. The power needed for the peak temperature for the selected Pr_{ref} is computed, and using the eq. 3.3.6, the spatial distribution of speed is computed as a function of Pr .

The results of one experiment are shown in Figure 3.3.12. The functional forms shown are a sinusoid, a line, and a step-function; the intensity normalization values are not shown. A quantitative comparison between the experimentally measured results and the intended profiles shows good agreement. The changes in the profile are both measureable and fairly smooth.

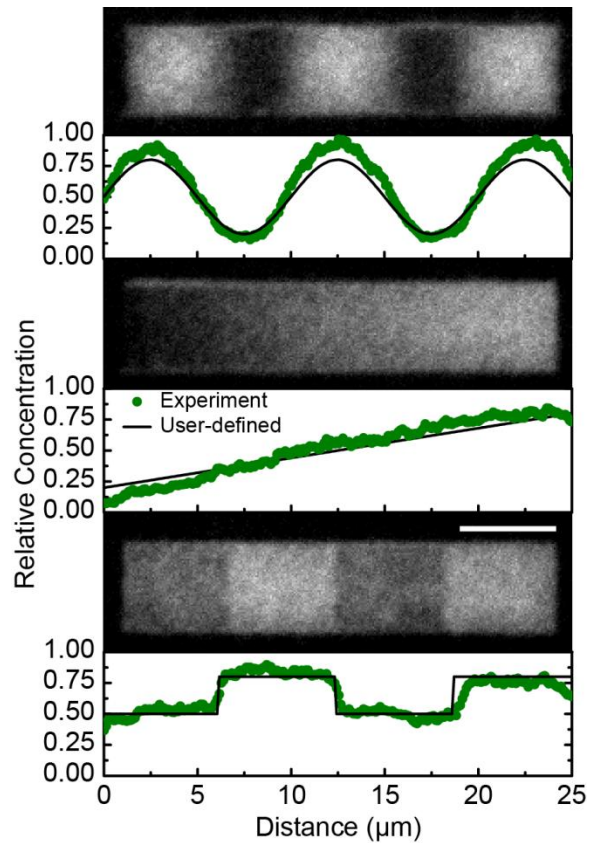


Figure 3.3.12 Experimental results showing controlled changes in chemical concentrations using variable speed. The plots indicate good agreement between the user-defined profiles and the experimentally measured values.

There are some differences between the intended and measured profiles. Some of these differences arise from the same difficulties discussed in the temperature control section, such as film thickness. Most of the differences, however, come from having an inexact Pr_{ref} value. Recalling that Pr_{ref} is a selected *measured* value, Figure 3.3.13 shows how a small deviation in the actual value for Pr_{ref} can ripple into deviations from the intended profile. For this reason, the optimal choice is a Pr_{ref} somewhere between 0.2-0.8; at too small Pr_{ref} values or a value too close to 1, errors are amplified because of the nature of eq. 3.3.6. The green scatter plot curve is the intended profile. The black indicates a theoretical curve where the measured Pr_{ref} is 0.5 but the actual Pr_{ref} is 0.55.

The blue curve is the theoretical output for situations in which the measured Pr_{ref} is 0.01 but the actual Pr_{ref} is 0.035. Finally the red curve is the theoretical output for situations in which the measured Pr_{ref} is 0.99 but the actual Pr_{ref} is 0.965. The results seen in Figure 3.3.13 show that the difference between the intended curve and the theoretical measured curve is minimized for a Pr_{ref} of 0.5.

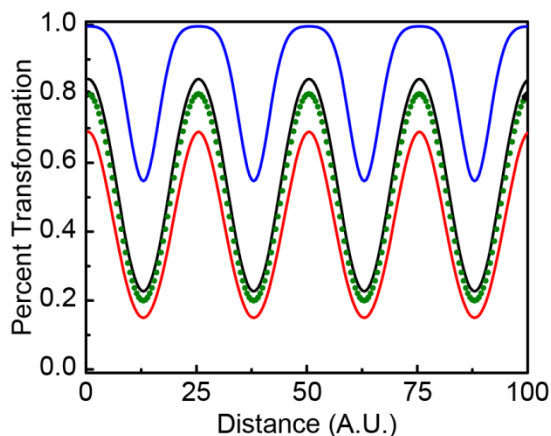


Figure 3.3.13 Plots showing how errors can be amplified in eq. 3.3.6. See text for details.

While Figure 3.3.12 shows variations in only 1-D, eq. 3.3.6 could be used to create 2-D profiles; however, this would be rather difficult, since secondary effects such as acceleration and timing would need to be taken into account. Another option would be to use a static form of the equation as done in the temperature case; however, the intent of this section is to show that speed can be used control the surface reactions, so Figure 3.3.12 suffices for this purpose.

3.3.6 Comparison of Temperature and Speed

Figure 3.3.9 and 3.3.12 show two different methods for controlling chemical reactions, and while it is instructive to ask which is better, there is no easy response to

this. Both have their advantages and disadvantages. Figure 3.3.14 shows the result of a comparison between temperature controlled patterns and speed controlled patterns. Because the results are so similar, there is little conclusion to draw about which is better. The key advantage to temperature, however, is that it is easier to implement 2-D complex patterning; the key advantage for speed is that the large working range for speed (3 order of magnitude) could lead to a reduction in error if the input speed is off.

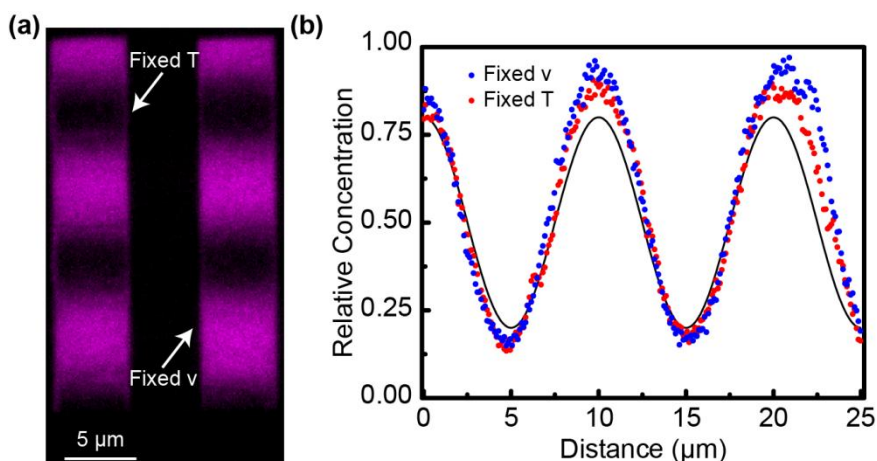


Figure 3.3.14 Comparison of fixed temperature versus fix speed designed patterns. (a) Fluorescent image with fixed temperature on the left and fixed speed on the right. The normalization factor is not shown. (b) Plots of the intensity signals versus intended (solid line).

3.4 Final Word

This chapter was dedicated to proving and verifying the model derived in chapter 2. In addition, the model was applied to control chemical reactions by varying temperature and speed. The results showed good agreement, and while some effects were ignored, this shows that the chemical kinetics model describes most of the observed and intended chemical changes taking place at the polymer substrate. The truly powerful aspect about the methods and techniques developed in this section is that they are not

limited to using fluorescent microscopy to measure a change in a substrate, but rather they can be generalized to other physical or chemical properties such as the change in conductivity of graphene oxide to reduced graphene[65]. Another example is described in chapter 4, where because of the chemical transformation taking place, there is a measureable physical change taking place as well.

CHAPTER 4

EXTENSION OF TCNL TO 3D

4.1 Introduction

Previous works have shown that TCNL induces chemical transformations on a substrate. In chapter 3, we showed that temperature and speed can tune the amount of reaction at the surface. The ability to tune surface reactions down to near nano-scale sizes and with such accuracy holds promise for a number of different research fields (see chapter 6 for examples). In reality, the chemical reactions driven by TCNL are not limited to the surface, but rather occur in 3-D because the temperature profile penetrates into the surface. The transformations from TCNL extend not only along the surface but also into the body of the substrate. The penetration of the TCNL reaction into the sample (hereto referred as the z-dependence) undoubtedly leaves behind a measurable and detectable effect. For example, TCNL has been used to reduce graphene derivatives[65-66]; the results have shown an increase in the conductivity of the patterned areas. This reduction conversion, however, measures not just the surface transformation, but also the z-dependence of TCNL (in graphene for example, there are a few layers of material).

Chapter 3 focuses on describing and modeling how TCNL can be used to control reactions; because we attached fluorescent molecules to exposed surface amines, our measurements were confined to the surfaces and we did not develop a systematic approach to detect body effects. In reality, an understanding the 3-D effects of TCNL is quintessential for other applications that extend beyond surface patterning to 3-D lithography[55-56] or controlling ferroelectric properties with TCNL[67, 122-123]. Chapter 3 was also limited in that we relied on quantitative fluorescent microscopy to analyze and verify the chemical kinetics model, but most materials that have been used in conjunction do not always exhibit physical or chemical manifestations of TCNL induced

transformations that are easily converted to fluorescent microscopy. It would be useful to develop a technique to extend the results from chapter 3 to other material transformations. The goal of this chapter is two-fold: 1) to go beyond surface only effects and examine the z-dependence of TCNL and 2) to develop a method to expand our analysis from relying on fluorescent microscopy. The first goal is motivated by the drive to understand and predict the effects of the TCNL process on substrates, such as graphene oxide/reduced graphene. The second goal expands the chemical kinetics model and predictions to other materials which exhibit different physical or chemical manifestations from TCNL induced reactions.

To accomplish these goals, a different organic polymer is introduced: a poly(*p*-phenylene vinylene) (PPV)-precursor, known as poly(*p*-xylene tetrahydrothiophenium chloride)(PXT). PPV is a semi-conducting polymer which was first introduced as an organic polymer alternative for light emitting diodes (LEDs)[124]. The conversion of PXT to PPV has been demonstrated down to about 70 nm[70] using TCNL, and processing the polymer substrate can reduce this even further down to about ~30 nm[59]. What makes the transformation process from the precursor film to PPV attractive as a candidate for studying 3-D effects is that the transformation leaves behind a measurable and quantitative change in the materials photoluminescence, and because the films have a certain thickness, the intensity of photoluminescence depends on how far the reaction penetrates into the sample.

This chapter is organized into four parts. The first part expands the chemical kinetics model developed in chapter 2 to compare surface effects with the z-dependence. The second part discusses the transformation of the precursor film to PPV. The third part semi-quantitatively shows how PPV changes as a function of heater temperature, and we show that one of the physical manifestations of the chemical transformation is a change in the surface topography. We exploit this relationship in the last section to produce

topographic gradients and to make a very rough approximation about the temperature profile's decay length into the sample.

4.2 Simulations of Chemical Kinetics in 3-D

In chapter 2, an equation for TCNL induced transformations was derived for the body transformation given as:

$$Pr_{body} = \frac{N}{N_{tot}} = \frac{\int \int \int Pr(x, y, z) dx dy dz}{\int \int \int dx dy dz} \quad (4.2.1)$$

where Pr_{body} is the probability that the volume of interest undergoes the chemical reaction, and Pr is the spatial probability a single point undergoes the reaction. Pr is given by:

$$Pr(x, y, z) = 1 - e^{-\frac{A}{v} \int_{\mathbf{x}_0} \frac{-E_a}{R(T(\mathbf{x}_0 | x, y, z))} d\mathbf{x}_0} \quad (4.2.2)$$

As explained in chapter 2, we ignore the y-direction dependence since the distance between consecutive lines is on the order of or smaller than the FWHM. We also ignore the x dependence because we avoid edge effects⁶. With these assumptions, eq. 4.2.1 reduces to:

$$Pr_{body} = \frac{N}{N_{tot}} = \frac{\int Pr dz}{\int dz} = \frac{\int Pr(z) dz}{L} \quad (4.2.3)$$

where L is the film thickness, and $Pr(z)$ is now given:

$$Pr(z) = 1 - e^{-\frac{A}{v} \int_{\mathbf{x}_0} \frac{-E_a}{R(T(\mathbf{x}_0 | z))} d\mathbf{x}_0} \quad (4.2.4)$$

⁶ This is not the same as ignoring the \mathbf{x}_0 integral. \mathbf{x}_0 is an integral over the tip's trajectory.

Eq. 4.2.3 is complicated since it relies heavily on knowing the temperature profile. As discussed in chapter 2, the temperature profile is difficult to compute; furthermore, even with an analytic form for the temperature profile, closed analytic forms for equation 4.2.3 are not easily computed. Instead computational forms are needed, and for simulations done below, we break the z -integral into uniform, discrete layers, and replace the above with:

$$Pr_{body} = \frac{\sum_i Pr_i(z)}{N} \quad (4.2.5)$$

where the summation is over the different layers, and N is the number of layers. To gain insight to how equation 4.2.5 depends on speed and z decay lengths, a temperature profile will be assumed:

$$T = (T_{peak} - T_o) e^{-\left|\frac{x_p}{\lambda}\right| - \left|\frac{z}{\Lambda}\right|} \quad (4.2.6)$$

where λ is the x decay length and Λ is the z -decay length.

There are three regimes to consider: Λ equal to the film thickness (L), Λ greater than the film thickness, and Λ less than the film thickness. For these simulations, the film thickness is 50 nanometers, and each layer is assumed to be a nanometer thick.

Figure 4.2.1 shows the simulations of the surface and body transformations for three different z -decay lengths (50 nm, 100 nm, and 25 nm) and a fixed λ (100 nm) for four different speeds (1 $\mu\text{m/s}$, 10 $\mu\text{m/s}$, 100 $\mu\text{m/s}$, 1 mm/s). The first thing to note is that universally across these simulations, faster speeds show the same shift in the curve to the right that was predicted and experimentally verified in chapters 2 and 3. To understand how the film's body transforms, we want to compare it against something familiar, and since we have developed intuition in chapter 2 and experimental evidence in chapter 3 for surface reactions, we use the surface transformation as a frame of reference.

Conceptually, there is a difference between the two because as is explicitly stated in eq. 4.2.5, body effects include not just a single layer, but multiple layers. But as we will show, we can think of the body transformation not as a continuous structure, but as a set of layers undergoing an effective “surface” transformation at different temperature ranges dependent on the z-decay length.

In all three cases, peak temperature required for any non-trivial percent transformation value is greater than the peak temperature for the same *surface* percent transformation. For example, at 10 $\mu\text{m/s}$, the peak temperature for a surface percent transformation of 0.50 is about 190°C, while the body transformation requires a peak temperature of about 480°C, 300°C, and 240°C for z-decay lengths of 25 nm, 50 nm, and 100 nm respectively. Physically this comes from the decay of the temperature profile through the 50 nm thick film, and in order for the chemical transformation to occur some distance into the film, the peak temperature must be increased to compensate for this decay.

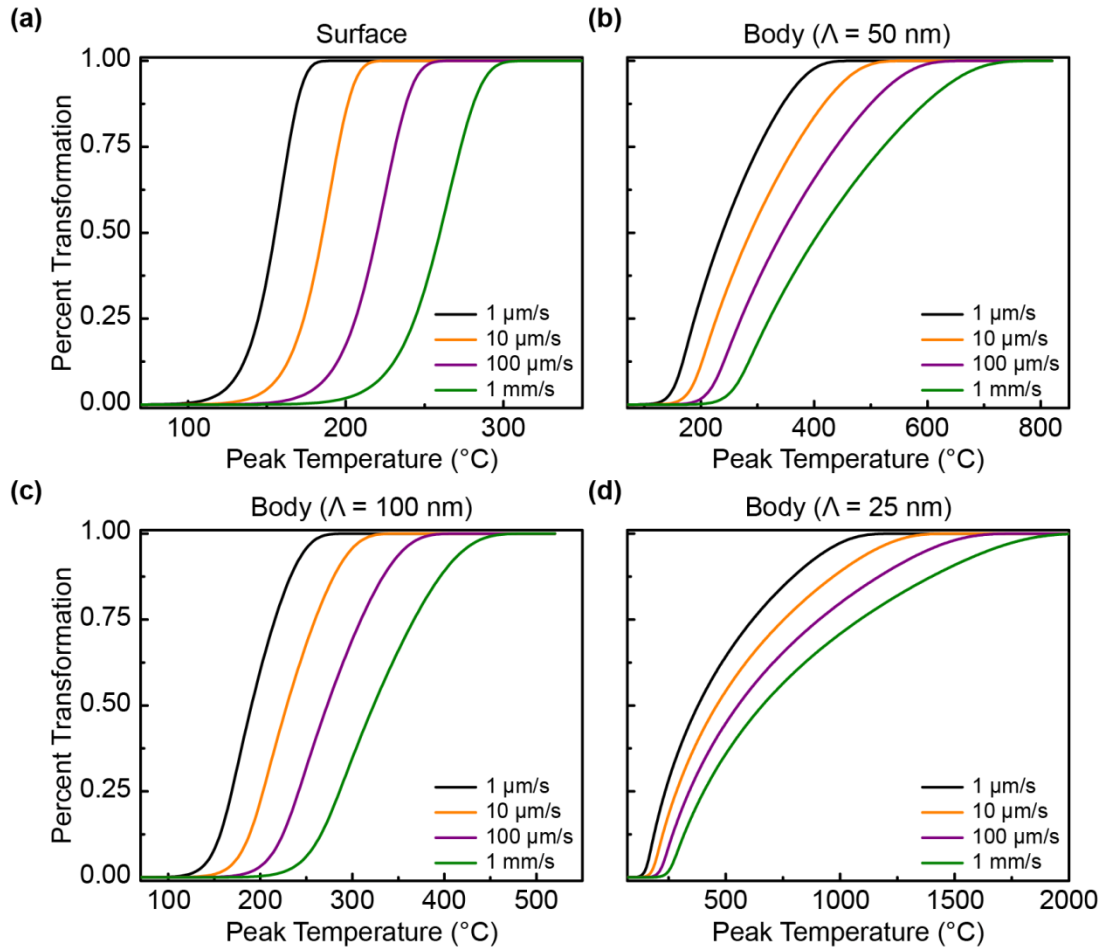


Figure 4.2.1 (a) Simulation of the surface transformation for a decay length (λ) of 100 nm for four different speeds. Simulations at four different speed for the body transformation for three different z-decay lengths: (b) $\lambda = 50$ nm, (c) $\lambda = 100$ nm, (d) $\lambda = 25$ nm. The assumed film thickness is 50 nm.

The discrepancies between the body and surface transformation temperatures start to dwindle as the z-decay length (λ) increases. This is demonstrated in Figure 4.2.2, where a simulated z-decay length of 400 nm is shown. The differences between in the temperature ranges are minimal in comparison to those for short decay lengths, such as those shown in Figure 4.2.1d.

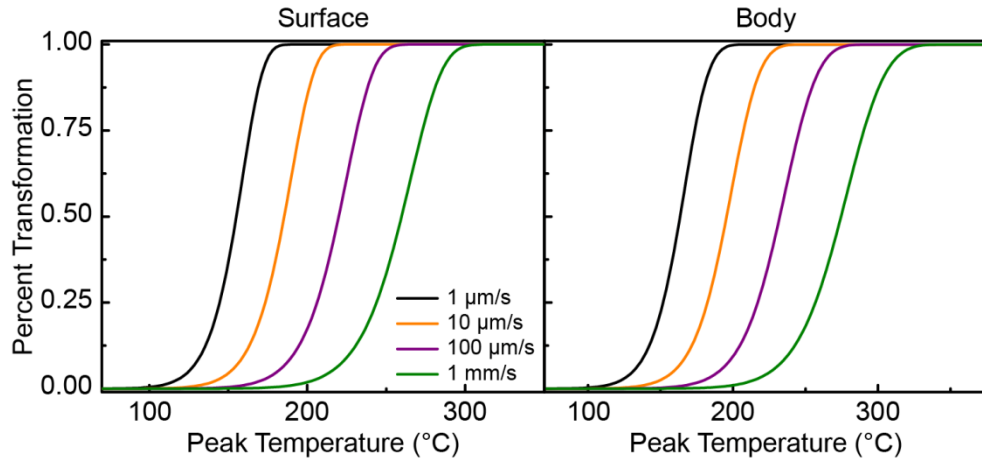


Figure 4.2.2 Simulation showing that at larger z -decay lengths ($\Lambda = 400$ nm), the body transformation's temperature range starts to overlap with the surface's transformation temperature range.

If Λ is decreased to the approximate spacing between layers, the conversion of individual layers can be observed. Figure 4.2.3 shows the simulation for a z -decay length of 1 nm; this decay length match the spacing between layers. The conversion of each layer is labeled in the figure; each layer follows an S-curve, but over different temperature ranges. The S-curve becomes exaggerated with increasing layer, the exaggerated forms account for why at short z -decay lengths (such as 25 nm in Figure 4.2.1d), the S-curve starts to skew from the sharp curves seen for larger z -decay lengths. We can approximate the required peak temperature for each layer by accounting for the decay of the temperature profile. For example, at 10 $\mu\text{m/s}$ a percent transformation of 0.50 occurs at about 190°C, or about 170°C above room temperature, for the surface. For the same percent transformation, the second layer requires a peak temperature of approximately:

$$T_{peak} \sim \frac{170^\circ\text{C}}{e^{-1}} \approx 460^\circ\text{C}$$

above room temperature (or 480°C), and the third layer needs about:

$$T_{peak} \sim \frac{170^\circ\text{C}}{e^{-2}} \approx 1250^\circ\text{C}$$

above room temperature.

The above calculations based on Figure 4.2.3 can be generalized to approximate any z-decay length to:

$$\frac{(T_{surface} - T_o)}{(T_{body} - T_o)} \sim e^{-\frac{L}{2\Lambda}} \quad (4.2.7)$$

where $T_{surface}$ is the approximate peak temperature at which the surface undergoes 0.50 percent transformation and T_{body} is the approximate peak temperature for which the body undergoes 0.50 percent transformation. Comparisons of eq. 4.3.7 with the discussion for Figure 4.2.1 show good agreement.

Figure 4.2.1-4.2.3 and eq. 4.2.7 tell us that what affects the conversion of the body is not the decay length, but the ratio between film thickness and the z-decay length. Eq. 4.2.7 could also be used in reverse to determine an approximate z-decay length associated with a given material.

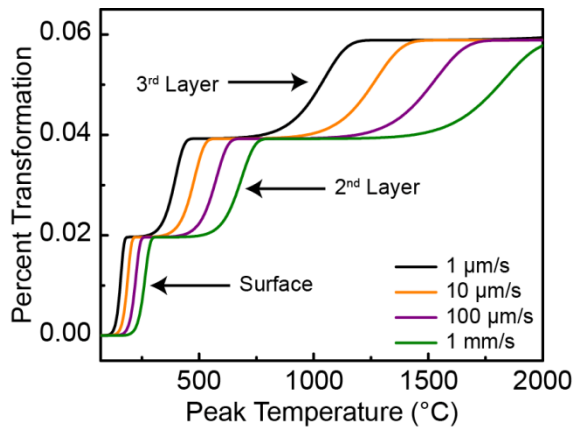


Figure 4.2.3 Simulation showing that at small z-decay lengths ($\Lambda = 1 \text{ nm}$), activation of individual layers can be observed.

Finally, there may arise situations in which the transformation of the entire film in z cannot occur; this happens because the peak temperature range is outside of the operating range of the thermal cantilever, or the material starts to undergo decomposition at the necessary peak temperatures. To overcome these limitations, varying speed continuously can provide a useful expression to estimate the decay length into the sample. If we continue to assume an exponentially decaying temperature profile, there we can make an approximation based on eq. 4.2.4. We show this by re-writing eq. 4.2.4 as:

$$Pr(z) = 1 - e^{-\frac{k_{eff}(z)}{v}} \quad (4.2.8)$$

where $k_{eff}(z)$ is given by:

$$k_{eff}(z) = \int e^{\frac{-E_a}{R \cdot (T(x_o | z))}} dx_o \quad (4.2.9)$$

Figure 4.2.4 shows plots of computed $k_{eff}(z)$ for different decay lengths ($k_{eff}(z)$ is represented as circles) and a fixed peak temperature of 220°C. $k_{eff}(z)$ seems to follow an exponential decay, approximated by:

$$k_{eff} \approx k_o \cdot e^{-\frac{z}{\kappa}} \quad (4.2.10)$$

where kappa is a new effective decay length, and k_o is related to the peak temperature through the Arrhenius equation. Fits using eq. 4.2.10 are shown also in Figure 4.2.4 as solid lines for different z -decay lengths.

The relationship in eq. 4.2.10 is significant for two reasons. The first is that for a given peak temperature, the ratio between the effective decay length and the z -decay length for different z -decay lengths is approximately constant (see Figure 4.2.4b). The ratio's value is dependent on the peak temperature, but for our working peak temperature

ranges of ~120-420°C, the ratio varies very little (as seen from the inset in Figure 4.2.4b, about 9-13). This narrow range for the ratio can give us an approximation for the z-decay length.

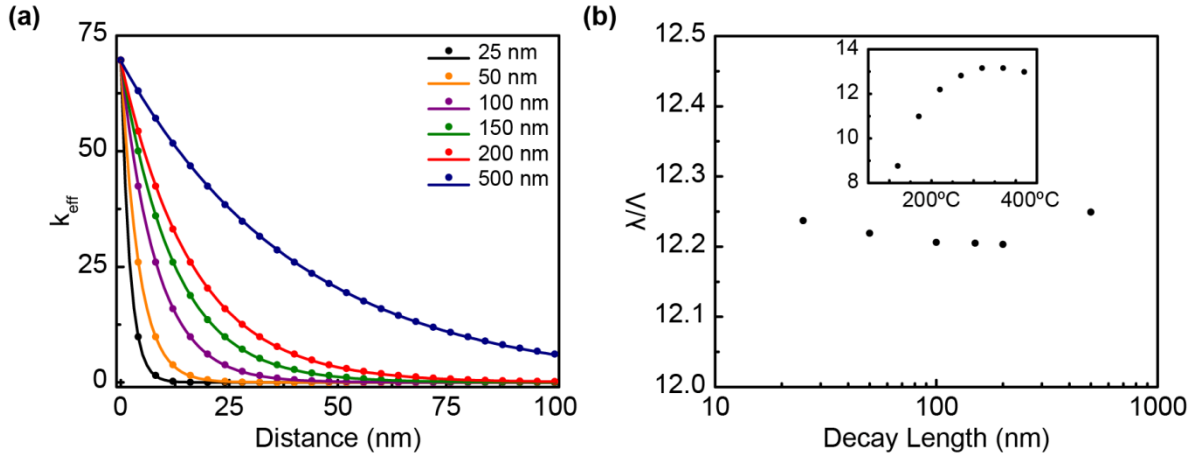


Figure 4.2.4 (a) Simulations (circles) and fits (lines) of $\kappa_{eff}(z)$ based on eq. 4.2.6 and eq. 4.2.9 for six different z-decay lengths ($\Lambda = 25$ nm, 50 nm, 100 nm, 150 nm, 200 nm, and 500 nm). (b) Comparisons of the z-decay length (Λ) to the effective decay length (κ) for the same six Λ decay lengths in (a). Inset shows how this ratio change for a fix Λ of 100 nm and variable T_{peak} .

The second reason that eq. 4.2.10 is important comes from combining eq. 4.2.3, eq. 4.2.8, and eq. 4.2.10. Appendix A shows the derivation, eq. 4.2.11 gives an analytic form for the probability:

$$Pr = \left(Ei\left(\frac{k_0}{v} e^{-\frac{L}{\kappa}}\right) + \ln\left(\frac{k_0}{v} e^{-\frac{L}{\kappa}}\right) - Ei\left(\frac{k_0}{v}\right) - \ln\left(\frac{k_0}{v}\right) \right) \cdot \frac{\kappa}{L} \quad (4.2.11)$$

Where $Ei(x)$ is the exponential integral[125-126], given by:

$$Ei(x) = \int_x^{\infty} \frac{e^{-x}}{x} dx$$

4.3 Conversion of PXT to PPV

We use the transformation of a PPV precursor film to PPV to demonstrate some of the predictions made in the previous section. Reviewed in this section are some of the properties of PPV; substrate preparation is also discussed.

4.3.1 Chemical Transformation and Properties of PPV

The chemical transformation for PXT to PPV has been used in a number of studies. The chemical transformation is shown in Figure 4.3.1a. PXT conversion to PPV has been demonstrated with near field UV lithography methods[127], but instead, we rely on the thermal cleavage of the tetrahydrothiophene (THT) to form the organic semi-conducting polymer. According to the literature, this material follows a first order reaction (see supplemental information of reference[59]). The Arrhenius constant, A, is given by $1.67 \cdot 10^{17}$ 1/s and the activation energy is measured to be 128 kJ/mol.⁷

⁷ These are also the values used in the simulations in section 4.2

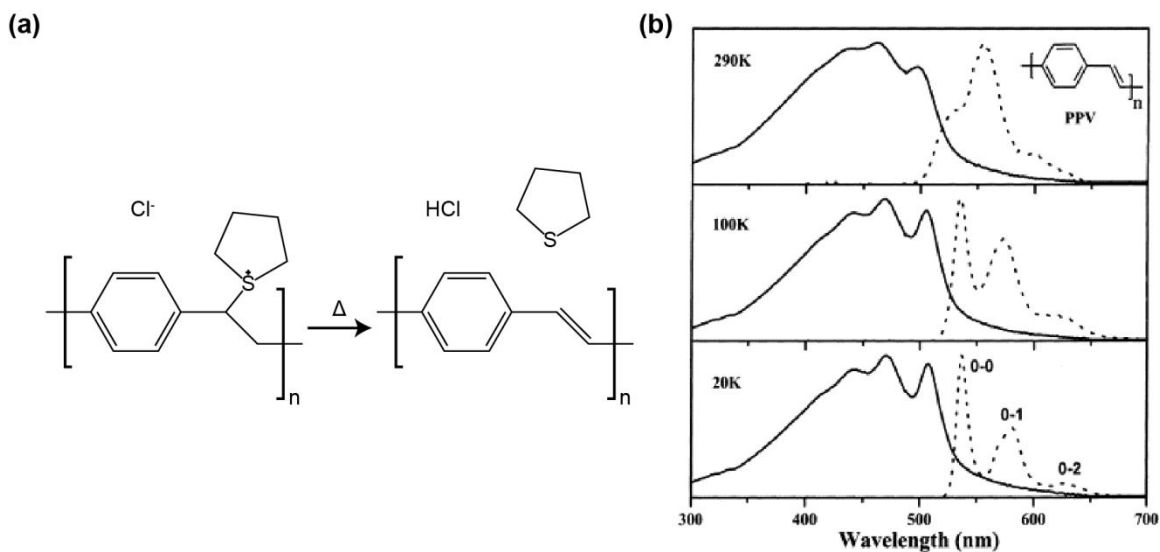


Figure 4.3.1 (a) Chemical transformation of PXT to PPV. (b) Excitation (solid line) and Emission (dashed line) of PPV⁸.

There are several ways to detect that the transformation has occurred. Since PPV is a photoluminescent material and PXT is not, we can use fluorescent microscopy to detect the transformation. The excitation/emission spectrum of PPV is shown in Figure 4.3.1b. For this work we use an excitation source centered around a wavelength of 480 nm and an emission filter centered around 535 nm.

Raman spectroscopy can also be used to detect the transformation of the precursor film to PPV. Measurement made in Figure 4.3.2a agree with previous observations: PPV patterns show an increased response at the 1600 cm^{-1} peak as well as in increase in the 1180 cm^{-1} peak[70]. There exist methods to quantitatively analyze Raman signals[128]; however, for this particular material, it is unclear whether these approaches apply. Figure

⁸ Reprinted from Chemical Physics Letter, Vol 342, Lim, S.H., Bjorklund, T.G., and Bardeen, C. J., Temperature-dependent exciton dynamics in poly(p-phenylene vinylene) measured by femtosecond transient spectroscopy, 555, Copyright (2001), with permission from Elsevier

4.3.2b shows the photoluminescent signal from a patterned PXT film; this image was taken before Raman measurements. Figure 4.3.2c shows the same pattern after Raman measurements. There is a noticeable change in the pattern, and based on these results, we observe that Raman measurements are potentially invasive and need further analysis. Careful treatment should make quantitative measurements possible, but these are beyond the scope and intention of this thesis. Instead, we rely on photoluminescent measurements and make the assumption that the fluorescent signal is linearly proportional to the concentration of PPV. We justify this assumption by working with *thin* films (<300 nm) coupled with the fact that photoluminescence signals have been observed to be approximately linear at low concentration regimes (at higher concentrations they show non-linear effects)[129]. We also discuss how to deal with situations in which the photoluminescence signal is nonlinear to the concentration of PPV.

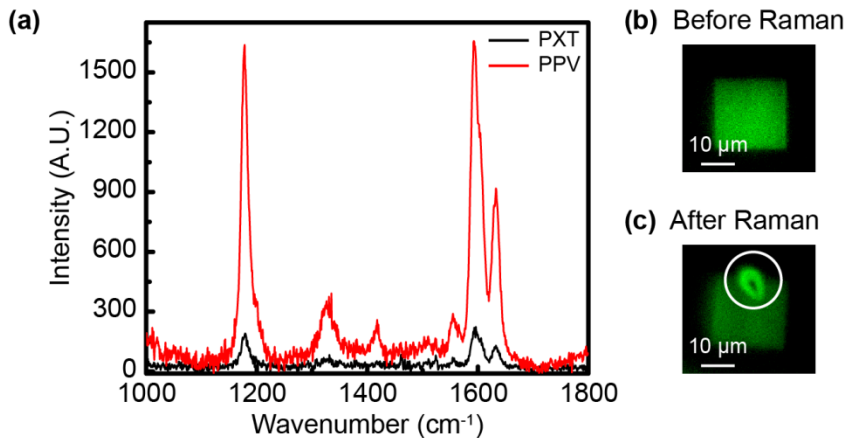


Figure 4.3.2 (a) Raman measurements indicated an increase in the 1180 cm⁻¹ and 1600 cm⁻¹ peaks; this indicates the transformation from PXT to PPV. (b) Fluorescent image of PPV patterns before Raman measurements. (c) Fluorescent image of the same PPV pattern after Raman measurement. The circled region indicates the invasive nature of the Raman probing laser.

4.3.2 Film Preparation

Silicon substrates were cut into 1 in by 1 in squares. Select samples were sonicated for 30 minutes each in a 5 % (v/v) solution of Micro-90 detergent in deionized (DI) water, DI water, and ethanol. These samples were then rinsed with ethanol and dried under a flow of nitrogen. All samples were then immersed in Piranha (3:1 sulfuric acid:hydrogen peroxide) for 30 minutes with a subsequent 30 minute immersion in DI water. Samples were then washed with DI water followed by ethanol and dried under a flow of nitrogen. The freshly cleaned samples were spin-coated at different speeds with a 25 % (ppv precursor name here) in water solution to achieve the desired thicknesses. In the case of samples for Raman measurements, PPV precursor was drop-casted and allowed to dry under ambient conditions. The best results were from film thickness of about 100-300 nm which were obtained from spinning speeds of 300-625 RPM using an acceleration value of 330 rpm.

4.4 Measurements of PXT/PPV Transformation

To test how the photoluminescence varied with tip-surface temperature, two sets of squares were patterned on the PPV-precursor. One set was written at 1 $\mu\text{m/s}$, while the other was written at 10 $\mu\text{m/s}$. The heater temperature was fixed for each square pair but increased from $\sim 100^\circ\text{C}$ to 550°C across the array in temperature steps of $\sim 20^\circ\text{C}$. The experiment is depicted in Figure 4.4.1a.

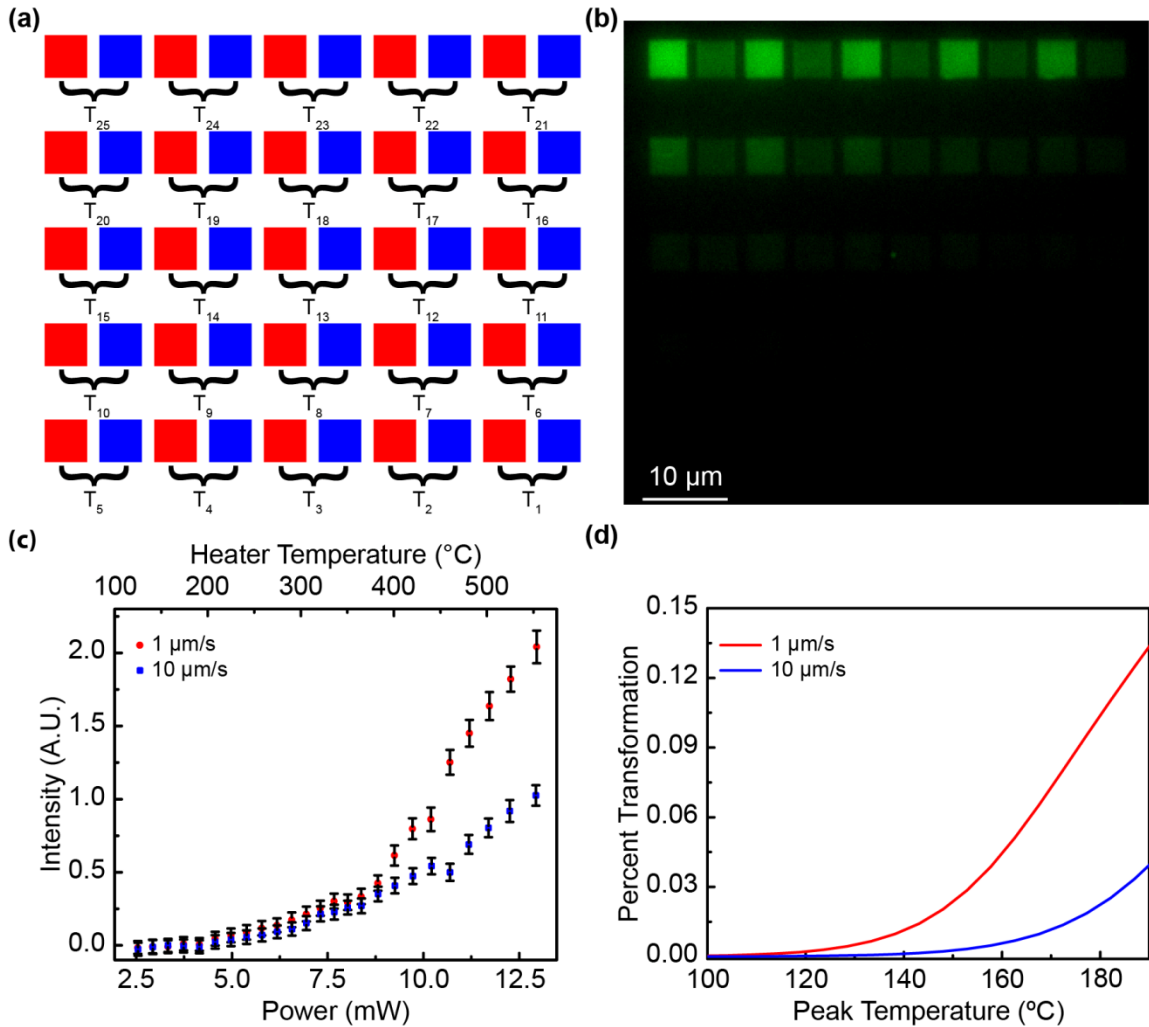


Figure 4.4.1 (a) Experimental schematic for the measuring the change in the photoluminescence signal with changing heater temperature. Red squares indicate patterns written at 1 μm/s, while blue squares are at 10 μm/s. (b) Photoluminescent image of the pattern corresponding to the experiment in (a). (c) Semi-quantitative measurements of the signals in (b). (d) Zoomed in version of Figure 4.2.1 (d) to indicate that the at low peak temperatures, the data forms agree. (Lambda = 25 nm, film thickness = 50 nm).

Figure 4.4.1b shows the corresponding photoluminescent signal for the described experiment. Qualitatively, we observe that the signal increases with heater temperature for both speeds; this agrees with previous results[70], as well as the predictions made in section 4.2. The squares written at slower speeds show an enhanced photoluminescent

response as compared to their higher speed counterparts. This agrees with the shift of the S-curve to the right as mentioned in section 4.2.

Semi-quantitative measurements are shown in Figure 4.4.1c. The processing is similar to that discussed in chapter 3. Background images corrected for any uneven illumination. The key difference between the analysis here and that done in chapter 3 is that our plotted intensities, I , are not normalized, but instead are given by:

$$I = I_{measured} - I_{background} \quad (4.4.1)$$

where $I_{measured}$ is the average intensity of a square and $I_{background}$ is an average background intensity levels. The normalization factor was removed to prevent any misconception that a 1 value represented full conversion. Here, I represents more than just the surface effects we measured in chapter 3, but also the effects of the entire body since the z-resolution of the microscope is larger than the film thickness (even methods such as TIRF or confocal microscopy will not work for these film thicknesses around 100 nm[130-131]).

The plots shown in Figure 4.4.1c show that as the heat temperature increases, the photoluminescent signal increases slowly at first, and then it appears to increase at an approximately linear rate at a heater temperature of about 400°C. At first glance, these trends do not seem to agree with the discussion in section 4.2; however, close inspection of Figure 4.4.1d, which is a zoomed in version of Figure 4.2.1d, shows that for small peak temperatures, the simulations are similar to those seen in Figure 4.4.1c. These results are suggestive that the temperature profile is not penetrating far enough into the sample to transform the entire film.

The results shown in Figure 4.4.1 are suggestive that a chemical kinetics model applies, but in order to provide additional evidence, we want to show other predictions made in section 4.2 are also true. One of the key observations reported in section 4.2 is that the surface undergoes the transformation before the film body does. In chapter 3, we

discussed how FFM can detect changes in a substrate's chemistry. Specifically, FFM is capable of detecting changes in hydrophilicity/hydrophobicity because of the change in capillary forces at the tip-substrate interface[112, 121]. Comparisons of the pre-cursor chemical structure to PPV's chemical structure suggest the pre-cursor is more hydrophilic than PPV. FFM should be able to detect this change, and by its very nature as a surface technique, it would only measure the surface's transformation. The results of an experiment in which the heater temperature was varied across an array of squares is shown in Figure 4.4.2. While the exact relationship between the measured friction signals and the concentration of PPV to PXT is not known, certain things should be expected. At low concentrations of PPV the friction signal should be approximately the same as the precursor film; at higher temperatures, once the local surface has been fully converted, the friction signals should level off to measure a fixed PPV only signal. Figure 4.4.2 shows how the friction signal varies with heater temperature; the trend in the FFM agrees with our discussed prediction in the friction signal. At lower temperatures, the friction signal is not much different than the precursor, while at higher temperatures, the patterns show a contrast in the friction signal from the substrate. Plots of the friction signal versus heater temperature show that the friction signals plateau above a heater temperature of 400°C.⁹ While the data is noisy, we interpret the leveling off as indication that the *surface* has fully undergone the reaction.

⁹This heater temperature should not be confused with the previous heater temperature of 400°C for Figure 4.4.1; these experiments were done on separate films and with different tips.

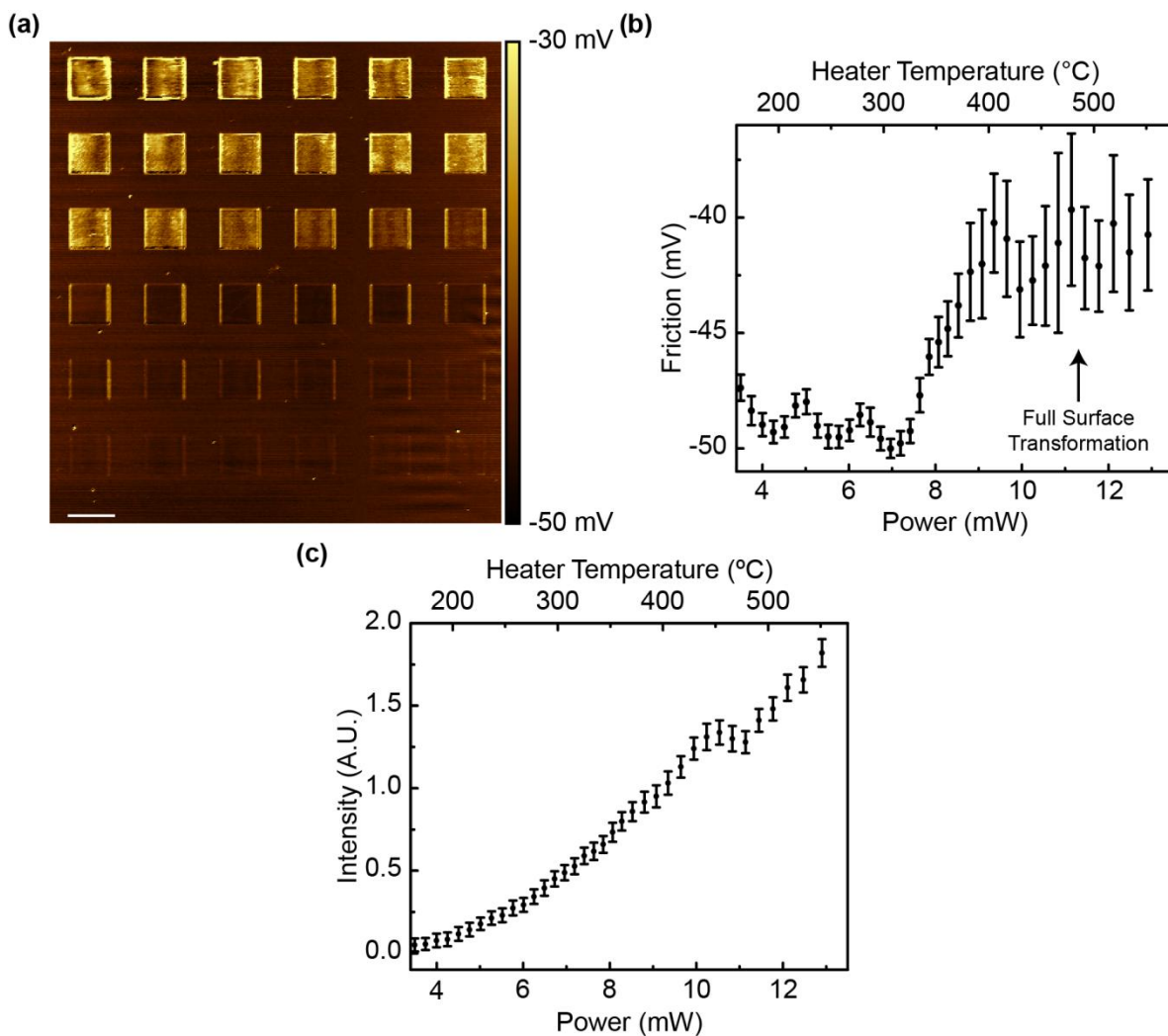


Figure 4.4.2 (a) Friction measurement for a series of squares written at heater temperatures of $\sim 150^{\circ}\text{C}$ up to $\sim 550^{\circ}\text{C}$. (b) Plots of the friction signal versus heater temperature seen in (a). Above 400°C the friction signal is seen to level off; this is indicative the surface transformation has completely taken place. (c) Plot of the fluorescence signal for the pattern in (a). The signal continues to increase pass the 400°C heater temperature; this suggests the body has not undergone the complete transformation, while the surface has.

Comparing the results against the pattern's photoluminescent signals show that the signal is still increasing past a heater temperature of 400°C (Figure 4.4.2c). This suggests that the entire film has not undergone the reaction, but the surface has.

AFM measurements also indicate that when the precursor undergoes the transformation to PPV from a localized temperature profile, the patterned areas show a reproducible change in the surface topography. Figure 4.4.3 shows an example in which an array of squares at increasing temperatures was thermally patterned. Figure 4.4.3a shows that for low temperatures, the drop in topography is smaller when compared to the drop at higher temperatures. The measured depth drop in topography ranges for this sample from about 2 nm to about 30 nm. While it is tempting to relate the change in topography to the loss of the side group from the chemical reaction, there is no direct evidence to prove that this is the only cause of the change in topography. This change in topography has been observed previously, and it is suggested in the literature that this drop may come from polymer confinement[59] or from the loss of water and the THT side chain[59, 132]. This shrinking results from the polymer being able to closely pack on itself. It is likely that the drop in topography results from a combination of loss of side group and polymer shrinking.

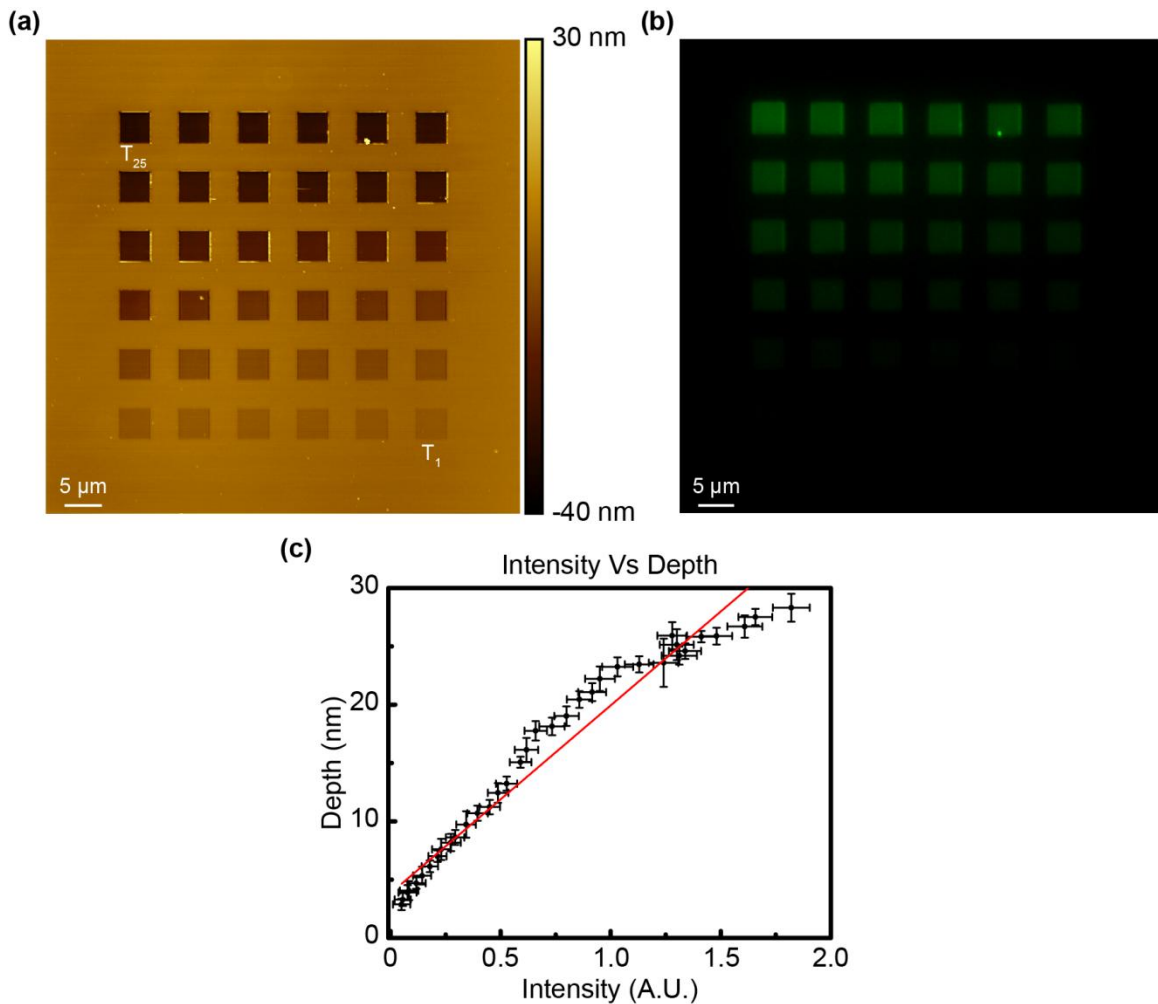


Figure 4.4.3 (a) AFM measurements of squares patterned into PPV. The heater temperature range is $T_1 \sim 160^\circ\text{C}$ (lower right) up to $T_{25} \sim 550^\circ\text{C}$ (upper left). (b) Fluorescence signal of the pattern in (a). (c) Comparison of the change in PPV height (depth) (a) versus the intensity signal in (b). The two are approximately linear.

Figure 4.4.3b shows the fluorescent images of the patterned areas, and again, we observe the intensity increasing with heater temperature. There are similar trends between the change in topography and the change in intensity: as the heater temperature goes up, the resulting change is amplified. Plotting the two values against each other reveals a close to linear relationship between the measured depth profile and the intensity signal. To compare the two signals, the surface height is measured with an inscribed square and the difference is averaged between unpatterned to the left and the right of the

square. The averaging is done to reduce possible artifact introduced from the large scan range of the image[133-134]. The intensity signals undergo the same processing as described above. The relationship between the topography change and the intensity signal is close to linear as seen in Figure 4.4.3c.

The above analysis suggests the change in height is linear to the photoluminescence, and because we have assumed the photoluminescence is linear to the chemical change, this implies that the change in height to be linear with the chemical transformation. By measuring the change in topography to the something comparable to the change in PPV concentration, we have essentially measured another physically parameter with which we can gauge the reaction process. For other systems, the relationship between the new parameter and the reaction need not necessarily be linear, but as long as there is a measureable or theoretically computed relationship between the concentration and a measureable parameter, the analysis developed in this and the previous chapters hold.

4.5 Using Topography to Demonstrate Extensions of TCNL

One of the goals we set out for this chapter was to use other physical parameters to measure the chemical kinetics model. FFM measurements and the correlation between the height and the intensity demonstrate two techniques which show measureable changes in the substrate chemistry. In particular, FFM measured qualitatively demonstrated the full conversion of the surface chemistry, while topographic measured the effect through the entire film. Figure 4.4.3 related the topography changes to the photoluminescence, and since our assumption was that photoluminescence is linearly related to the concentration of PPV, we can now assume the height is also linear to the PPV concentration. If other measurements indicate that photoluminescence followed some other functional dependence on PPV concentration, the height could still be used as a gauge for the reaction by composing the PPV-Photoluminescence dependence with the

linear relationship between height and photoluminescence. This section takes advantage of the observed linear height-photoluminescence relationship and the new linear PPV reaction to height relationship to demonstrate two concepts: 1) the proof of TCNL's control down to the nano-scale and 2) to approximate the z-decay length.

4.5.1 Nano-Scale Control

The results shown in chapter 3 for surface reactions show a nice predictable way to create and design patterns. As mentioned in chapter 3, we could not reproducibly alter topographic variations in the cinnamate polymer, and therefore we relied on fluorescent microscopy to analyze our data. Fluorescent microscopy, however, is diffraction limited, and because of this limitation, it is tough to scale the relationships down to the nano-scale without resorting to super-resolution techniques[130, 135]. For example, even though the pixels for the *Mona Lisa* depiction are spaced by 125 nm, for our current setup, there is no *easy* way to show that the model accurately predicted each pixel or if the point spread function[136] of the microscope effectively averaged the pixels to produce an approximately correct image.

PPV overcomes this requirement because the reproducible relationship between the change in height and the photoluminescence allows us to go beyond the diffraction limit by measuring the substrate with an AFM. An example of the improved imaging quality is shown in Figure 4.5.1 where another reproduction of the *Mona Lisa* down to $\sim 30 \mu\text{m} \times 40 \mu\text{m}$ is shown in PPV. The two key differences between this reproduction and the previous is that this is achieved empirically (hence why we show applied voltage instead of power), and rather than a pixel by pixel fabrication, the images seen here are fabricated with the tip moving continuously. Figure 4.5.2b shows the fluorescent image; the results show a similar diffraction limited reproduction of the *Mona Lisa* to that seen in Figure 3.3.10. Figure 4.5.1c shows the corresponding AFM image, and the extra detail not present in the fluorescent image can be seen with the higher resolution AFM image.

This result demonstrates that control of the chemical transformation continues down to the nano-scale (here the pixel resolution is $\sim 78\text{nm}$). Figure 4.5.1d shows the FFM measurement of the same pattern; this result is only qualitatively, and should not be interpreted quantitatively as we did with the squares because the rapidly varying topography prevents the friction signal's accuracy.

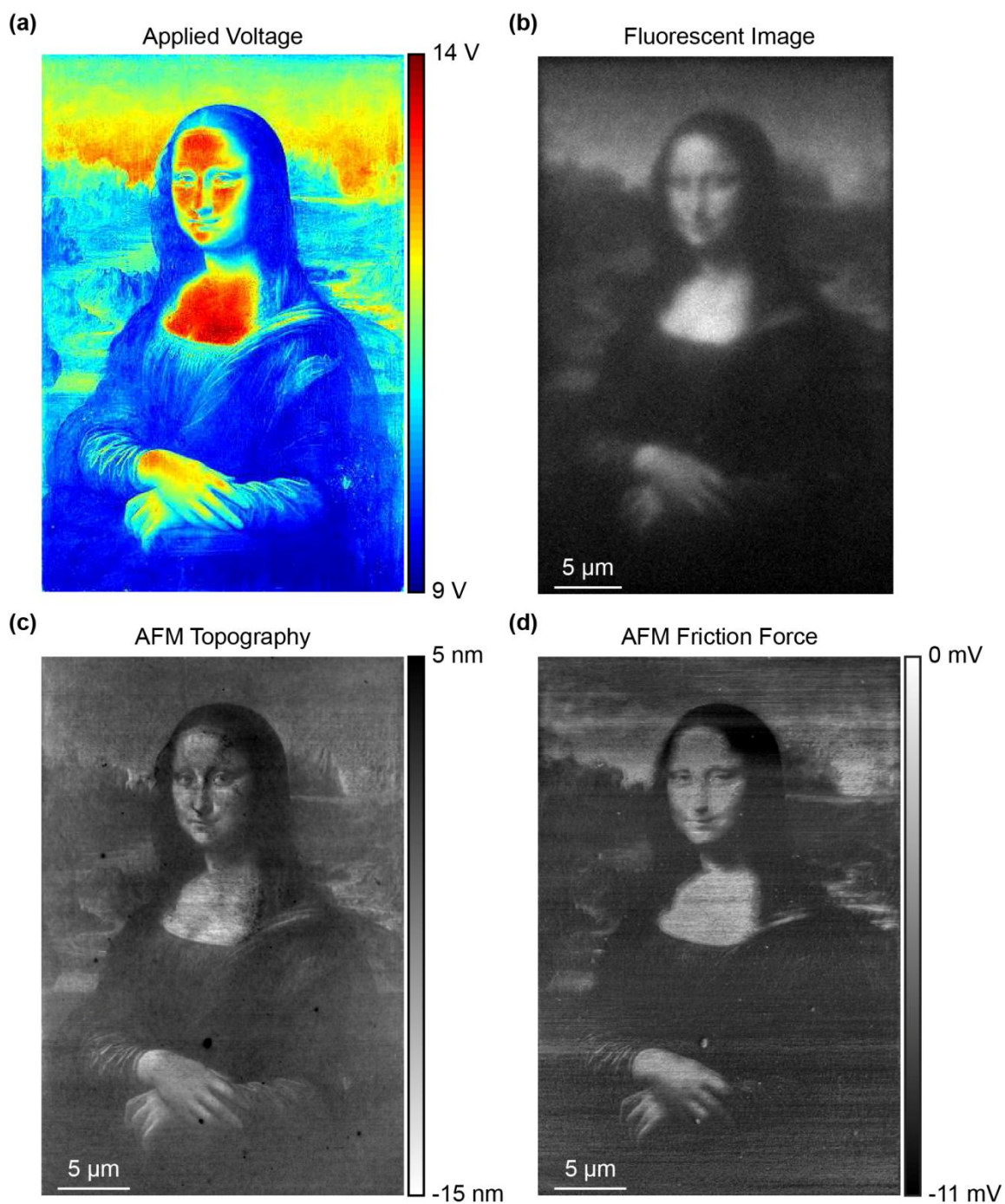


Figure 4.5.1 (a) Spatial distribution of applied voltage to create a 30 μm x 40 μm reproduction of the *Mona Lis`a*. (b) Fluorescent image of the patterned PPV. (c) AFM image of the patterned PXT/PPV film. Diffraction in (b) limits our ability to see the added details. (d) FFM measurements that qualitatively detail the reproduction.

To push the limits of this, a smaller version ($\sim 20 \mu\text{m} \times 33 \mu\text{m}$) is shown in Figure 4.5.2. The pixel spacing was $\sim 60 \text{ nm}$, and the topography reveals the same amount of detail as seen in Figure 4.5.1. The fluorescent image seen in Figure 4.5.2b, however, suffers further from diffraction, and the *Mona Lisa* blurs more, though it is still decipherable.

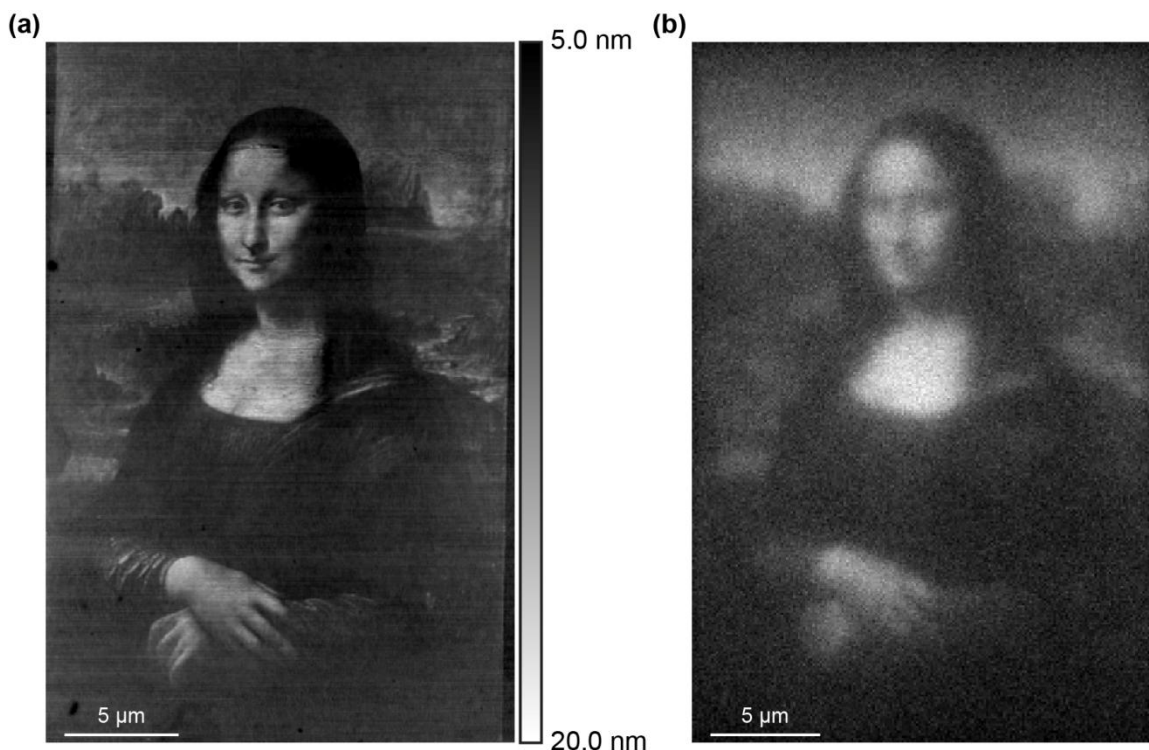


Figure 4.5.2 (a) AFM image showing $\sim 20 \mu\text{m} \times 33 \mu\text{m}$ reproduction of the *Mona Lisa* in PXT/PPV film (Mina Lisa 2.0). (b) Fluorescent image corresponding to the pattern in (a). Diffraction makes the image look blurry as compared with the high resolution AFM image.

The pixel resolution ($\sim 60 \text{ nm}$) shown in Figure 4.5.2 is slightly lower than previously measured FWHM of lines ($\sim 70 \text{ nm}$). Since the sample preparation was different for these two studies, a series of lines were written at different heater temperatures (see Figure 4.5.3). The measured resolutions are slightly above 60 nm , and

agree with previous results. The measured FWHM suggest that if the *Mona Lisa* were shrunk even further, one would expect to start seeing the topography image blur. Figure 4.5.2 is approaching those length scales, and it would be instructive to know if the length scales for blurring are different from the FWHM. This type of study could suggest that the FWHM is not an appropriate measure for the resolution, but we leave this for future work.

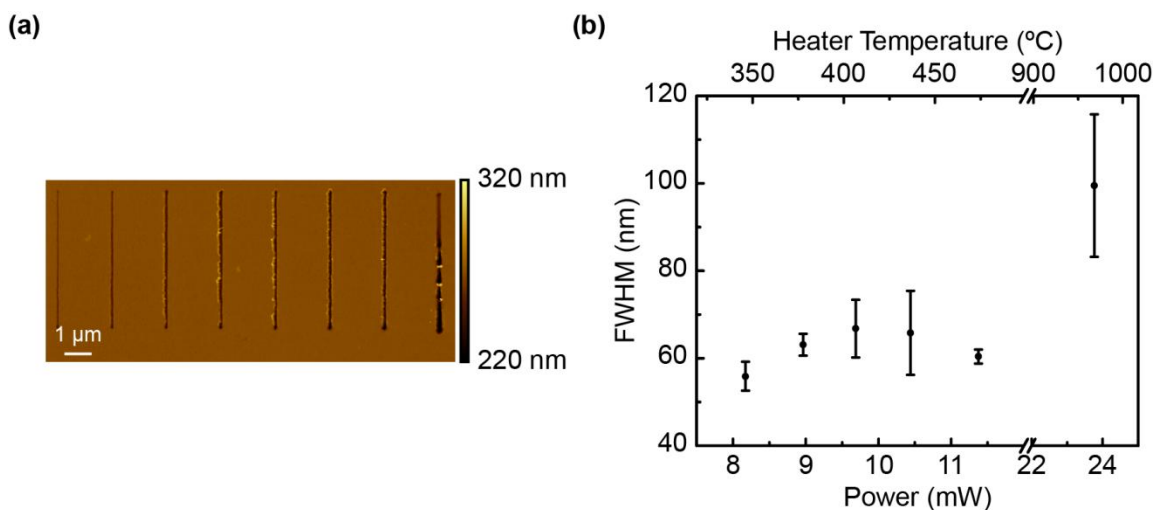


Figure 4.5.3 Measurements of FWHM of lines made in PXT/PPV film (a) AFM image of lines at different temperatures. (b) Measurements of the FWHM as a function of power and heater temperature.

4.5.2 Z-Dependence

Figure 4.4.1 and Figure 4.4.3 show that the depth and photoluminescent signals continue to increase with increasing temperature. The results from section 4.2 are suggestive that under appropriate conditions an S-curve should manifest. Those conditions are that the peak surface temperature reaches a high enough temperature to penetrate through the entire thickness to thermally induce a chemical reaction throughout the film. The thermal cantilevers, however, have certain limitations; for example their

optimal working range is below the thermal runaway ($\sim 600^{\circ}\text{C}$)[51]. Clearly the heater temperature cannot reach temperatures of 2000°C since the melting temperature of silicon is about 1500°C [137]; as a result, the tip-surface interface temperatures cannot approach those values (recall that the tip-surface temperature is less than the heater temperature[69, 108] as described in chapter 3 section 3.2.2). The limitations on the thermal cantilever may hinder the ability to induce the reaction throughout the entire film.

It is instructive to wonder to which depths the reaction does penetrate. The relationships developed in section 4.2 can at least suggest an approximate answer; specifically, using the relationship developed for the z-decay length and the effective decay length from eq. 4.2.10 and eq. 4.2.11. Figure 4.5.4a shows the experimental setup for measuring the z-decay length. Each rectangle is run at a fixed temperature, and as the tip continues up the pattern, the tip's speed decays exponential. Figure 4.5.4b shows the resulting AFM image corresponding to the experiment in Figure 4.5.4a. The topographic profiles show that at low speeds, the change in topography is greater than at fast speeds. This relationship agrees with the chemical kinetics model and the results seen in section 4.2. Figure 4.5.4c shows the corresponding plot of the fluorescent image (shown as an inset) of the patterned PPV. The signals indicate the same trend discussed for the drop in height.

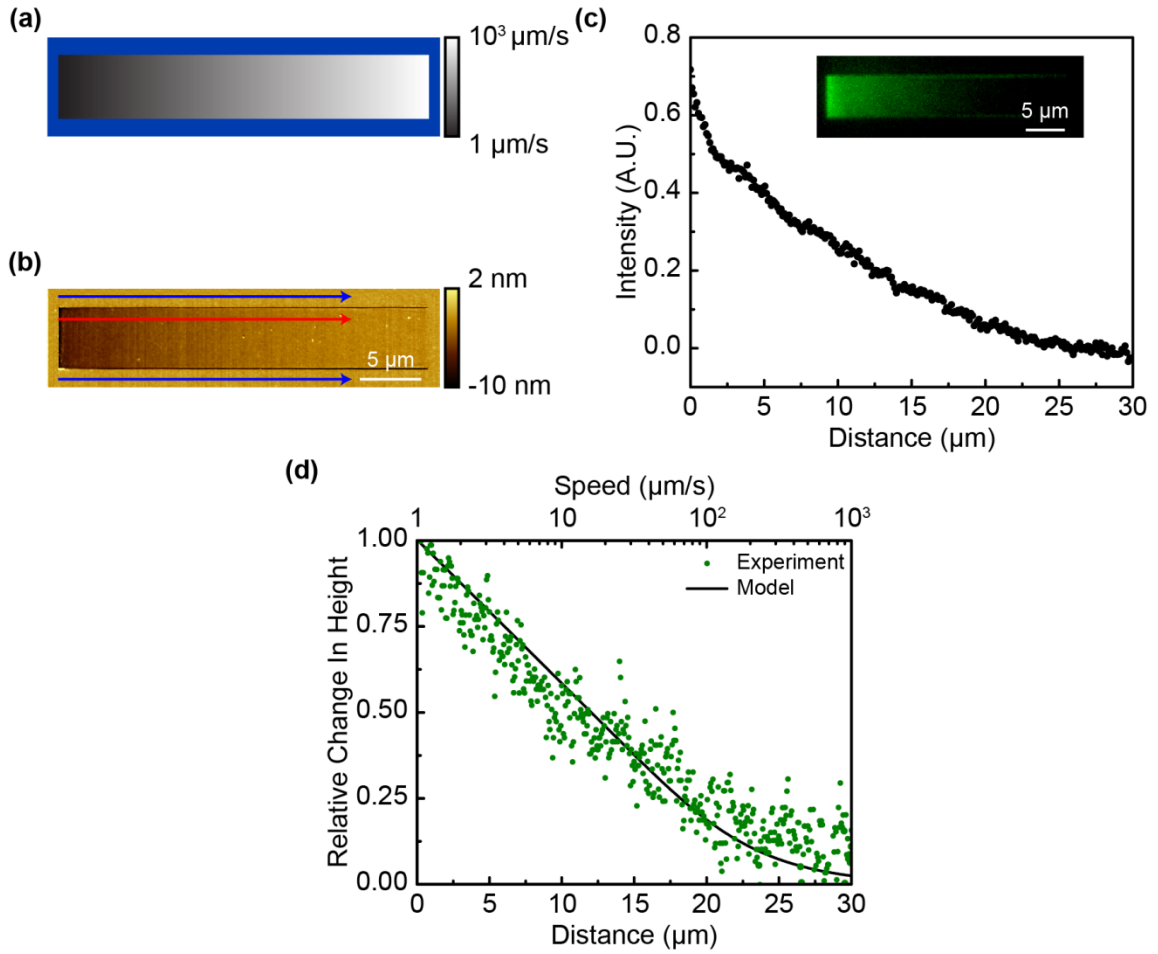


Figure 4.5.4 (a) Schematic showing an experiment in which the heater temperature is kept constant and the speed is varied as a function of position. (b) AFM image corresponding to the experiment in (a). (c) Plot of the fluorescent signal of the PXT/PPV pattern. (d) Fit of eq. 4.2.11 with experimental results in (b). The measured effective decay length is ~ 3.0 ; we approximate the temperature decay length as ~ 40 nm.

Comparing the fluorescent image with eq. 4.2.11 is difficult since diffraction makes edge detection difficult. Instead, the AFM data will act as a substitute since edge detection will not be such an issue. The normalized values are compared against a *normalized* version of eq. 4.2.11. The normalized depth values come from:

$$H_{rel} = |H_{pattern} - H_{surface}|$$

where H_{rel} is the absolute relative depth, $H_{pattern}$ is the profile of the pattern (red line in Figure 4.5.4b), and $H_{surface}$ is the average profile of the surface (average of the blue

lines in fig 4.5.4b). Finally, the absolute depth values are normalized by the maximal depth value.

Figure 4.5.4d shows the comparison between the measured AFM profiles and eq. 4.2.11. The measured effective decay length is about 3 (2.96). Assuming the decay length is approximately 13 times larger than the effective decay length, the temperature decay length in the z-direction is approximately ~40 nm . Given that the film thickness is about 100 nm for this substrate, in order for the transformation to fully penetrate through the entire sample, the peak temperature range needs to scale up to approximately 2500°C! This is well beyond the optimal working range of the thermal cantilevers. This result suggests that the reason we never obtained the full S-curve is that the temperature decays too rapidly into the sample. This result, however, needs to be taken with some care. The fits from eq. 4.2.11 are not that good, but this result does at least agree with our previously discussed experimental results. This is an on-going study, but the fact that the approximate z-decay length is also near the measured FWHM hints that at least this value is in the same range as the lateral decay.

4.6 Final Word

In this chapter, we set out to extend TCNL beyond the limitations of measuring surface reactions and started to make some observations on the penetration of the chemical reaction into the sample. We strived to define a methodical way to relate a physical manifestation of a chemical reaction into quantitative information about the chemical transformation rather than rely directly on fluorescence. Even though we assumed that the photoluminescence signal of PPV is linearly proportional to the PPV concentration, we described how to overcome any complications introduced if this assumption failed after some point. We also showed a unique method for creating topographic gradients and demonstrated control down to the nano-scale. The long term impacts of this chapter are describing the translation from one physically measurable

parameter to a chemical concentration and using that new relationship to show other features of TCNL and the chemical kinetics model.

CHAPTER 5

PARALLELIZATION OF TCNL

5.1 Introduction

Essential to the development of any lithographic technique for research and industrial applications is the ability to implement high-throughput patterning. In particular, SPM techniques have garnered significant focus and have made impressive advancements towards parallelization; parallelization here refers to any process which implements simultaneously use of multiple SPM probes with a single instrument. The emphasis on parallelization of SPM techniques derives from the fact that many SPM techniques are capable of achieving nano-scale resolutions but many are slow[138].

Parallelization of SPM techniques, however, introduces two major complications: the ability to read and to write. Traditionally, AFM techniques use an optical feedback for measuring surface properties, but parallelizing optical feedback would be tedious and grow in complexity with larger numbers of tips in use. A number of unique and interesting solutions have been developed to remove traditional optical feedback requirement; such solutions have included complementary metal oxide semi-conducting (CMOS) technologies employing piezo-resistive/strain effects[139-140], interferometric optical measurements[141], or thermal interactions between a thermal cantilever and a substrate[53]. There have also been some attempts to control individual cantilever z-actuation through contrasting thermal expansion coefficients[142], an effect often referred to in the literature as the bi-morphic effect¹⁰.

¹⁰ The bi-morphic effect also appears in the thermal cantilever used in TCNL, but in a less controlled manner

While many techniques have focused on reading and measuring surfaces, the ability to parallel write is relatively infantile in its development compared with the advancements made for single tips. There have been limited attempts for SPM based patterning parallelization. Parallelization of 50 tips produced 100 mm² patterned areas with electro-oxidizing lines in a silicon substrate[143]. DipPen Nanolithography (DPN) has employed the use of both passive and active cantilever arrays, which use the bimorphic effect to lift individual tips off the substrate[144]. The DPN community has also introduced 55,000 parallel cantilevers to pattern substrates down to 80 nm[50]. Thermo-mechanical lithography is of particular fame because of the IBM millipede, where near 1000 cantilevers were brought into contact with a polymer substrate and actively used to indent a surface with high resolution[52]. The “millipede” work was not limited to patterning, but also extended to imaging; moreover, that work introduced a cheaper alternative to the traditional expensive piezo-scanner[52].

This chapter is dedicated to the description and implementation of thermal cantilever arrays for TCNL parallelization. The focus is more on the implementation, as opposed to the more exact treatment in previous chapters. As with all SPM techniques, parallelization of TCNL still requires the ability to read and write; the ability to read is well described for thermal cantilevers throughout the literature, but it is briefly reviewed and demonstrated here. Most of this chapter, however, is focused on parallelization of TCNL patterning.

5. 2 Description of Thermal Arrays

The thermal arrays are composed of 5 tips as seen in Figure 5.2.1. All arrays were fabricated by the Professor William P. King’s lab at the University of Illinois at Urbana Champaign. For convenience, the tips are numbered 1-5. Each tip is individually addressable which means that tip 1 can be heated to one temperature while tips 2-5 are each maintained at different, unique temperatures. The electronic and thermal responses

of the tips are the same as those described in chapter 3 for a single cantilever. Since the arrays are manufactured simultaneously and under the same conditions, the thermal runaway point is similar for all five cantilevers[145].

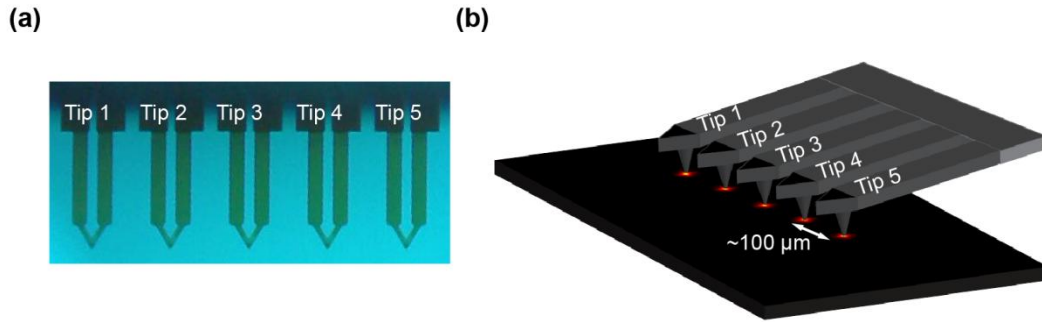


Figure 5.2.1 (a) Optical image of thermal cantilever array with numbering. (b) Schematic showing a thermal cantilever array inducing a temperature profile in a substrate.

5.3 Leveling

Arrays present an additional challenge not present with a single cantilever: leveling. With multiple tips, it is important to ensure all the tips are brought into contact with the surface simultaneously. By measuring the interaction between the thermal tips and a substrate, the arrays can externally be aligned with a substrate. To demonstrate these thermal interactions, we start with a single tip.

5.3.1 Interaction between a Thermal Tip and a Substrate

Analogous to other AFM modes, thermal cantilevers interact more with a substrate as distance between the tip and substrate decreases. For thermal cantilevers, some of interactions result from the increased air conduction between the cantilever legs and the substrate. As the gap between the tip and substrate decreases, there is a greater flux of heat out of the thermal cantilever's legs causing the integrated heater's temperature to go down (hereto referred to as the “cooling” effect). This effect is well

reported[91, 146]. The substrate induced cooling leads to a measureable change in the thermal cantilever's electronic properties since they are closely connected to temperature (see discussion in chapter 3). Although there have been other suggested routes, we measure this electronic change through the cantilever's electrical resistance for this work. An example and schematic are displayed in Figure 5.3.1. Figure 5.3.1a shows a force displacement curve[147] and the cantilever's change in resistance as a function of z-position. The resistance monotonically decreases as the tip approaches contact with the substrate; Figure 5.3.1b and c show a schematic of this process. Far from the substrate, there is less heat transfer between the cantilever and the substrate, resulting in a higher temperature; these higher temperatures cause a larger resistance. As the tip is lowered, there is a greater heat flux out of the cantilever's legs, and this leads to a lower temperature and a lower resistance[146]. Once contact is reached between the tip and the substrate (as indicated through the blue force-displacement curve), the inset to Figure 5.3.1 indicates that the resistance continues to decrease monotonically, but at a slower rate. It is likely that this comes from the fact that even though the tip is in contact with the surface, the cantilever legs still approach the surface both as a result of cantilever's increased bending and the elastic response of the surface[148].

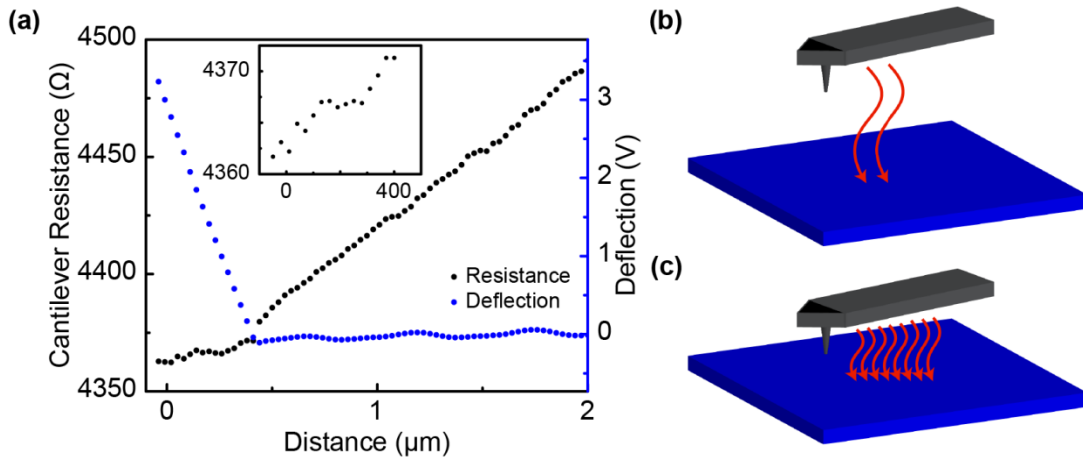


Figure 5.3.1 (a) Resistance measurement as a thermal tip is brought into contact with a surface; also shown in blue is the optical measured force displacement curve. (b) and (c) Schematics showing that at far distance from a substrate (a) the thermal cantilever transfers less heat than close to the surface (b).

5.3.2 Array Leveling

Coupling the “cooling” effect with a leveling device alleviates this issue. An optical leveling mount was integrated with the AFM to tilt the substrate in order to level the tips. The cooling effect indicates and measures which tips first contact the substrate; iterative adjustments of the leveling mount align the tips with the substrate. An example is shown in Figure 5.3.2, where tip 1 first reaches contact with the surface first (Figure 5.3.2a). After an adjusting the leveling mount, as indicated, all five tips are *approximately* in contact at the same time (Figure 5.3.2b). Variations in tip heights and cantilever bending prevent perfect alignment between the tips and the surface, and so a working range is about 200-300 nm for all tips to be in contact simultaneously.

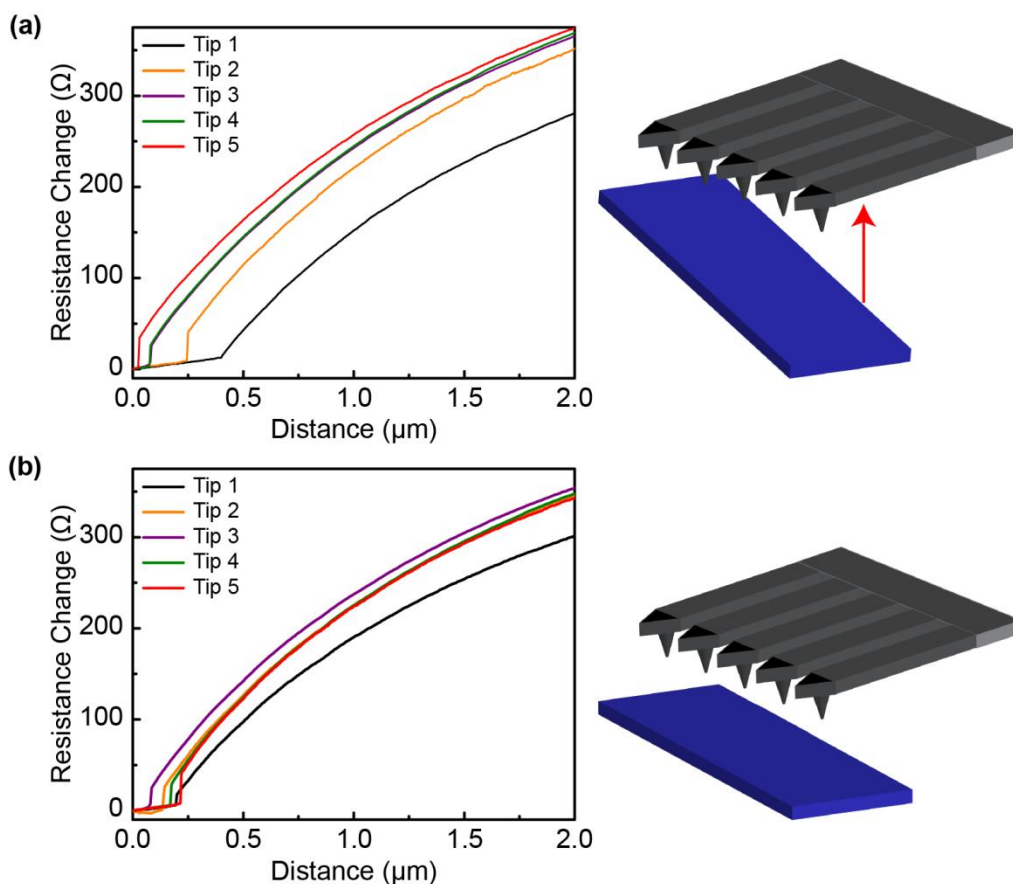


Figure 5.3.2 Resistance measurements of individual cantilever's in an array versus distance. (a) Measurement and schematic showing misalignment between the thermal cantilever array and the substrate. (b) Measurement and schematic showing all five tips in contact with the substrate near simultaneously after indicated correction made (a).

5.4 Thermal Patterning with Arrays

Having resolved issues with leveling, we return to parallelization of TCNL. Figure 5.4.1 and 5.4.2 show two examples of patterns made in the same PPV-precursor (poly(p-xylene tetrahydrothiophenium chloride)) described in chapter 4. For Figure 5.4.1, all five tips were brought into contact with the substrate simultaneously and patterned the same 3 by 3 array of pentagons at increasing temperatures. In agreement with the results shown and described in chapter 4, the corresponding fluorescent measurements suggest the conversion from the pre-cursor film to the semi-conducting

PPV polymer. As the temperature increases, so too does the photoluminescence of the PPV. Figure 5.4.1a, shows a Raman spectroscopy measurement of an array patterned area (fluorescence inset); the increased signal in the 1160-1180 cm^{-1} and 1580-1600 cm^{-1} wavenumber range are indicative of the chemical transformation[70].

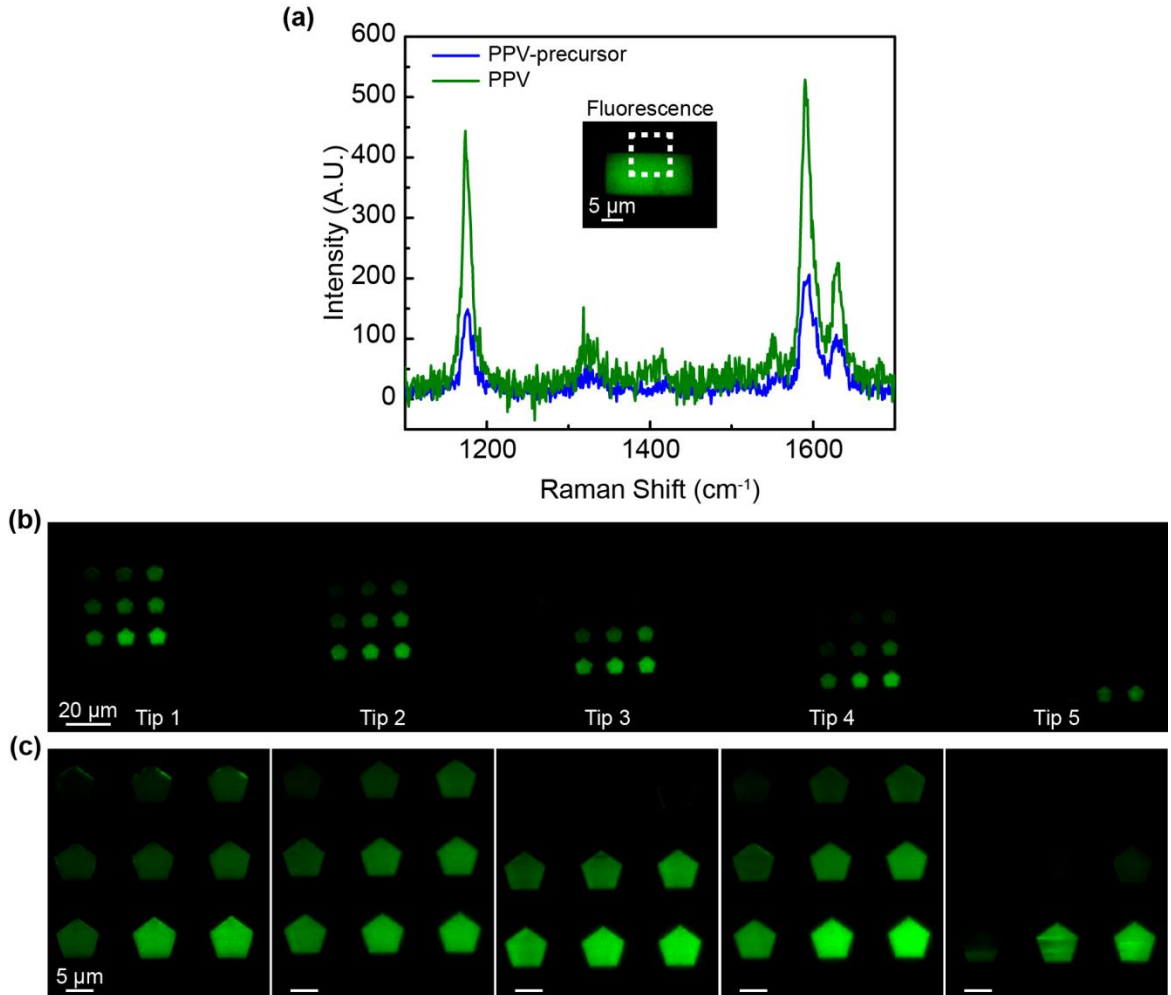


Figure 5.4.1 Thermal patterning in a PPV-precursor film made with thermal cantilever array. (a) Raman measurements indicating the transformation from precursor to PPV. (b) Fluorescent image of pentagon PPV patterns made with thermal array. (c) Zoom-in version of patterns from (b).

Figure 5.4.2 shows a PPV-precursor substrate patterned with a set of lines at increasing temperatures with the thermal cantilever array. The fluorescent images indicate the presence of the photolumescent PPV polymer, and AFM measurements indicate a change in the height that was described and measured in chapter 4. Finally Figure 5.4.2c, shows a profile of the lines; the inset indicates a resolution of 68 nm; this measurement is on par with values measured in chapter 4 and described in the literature[70].

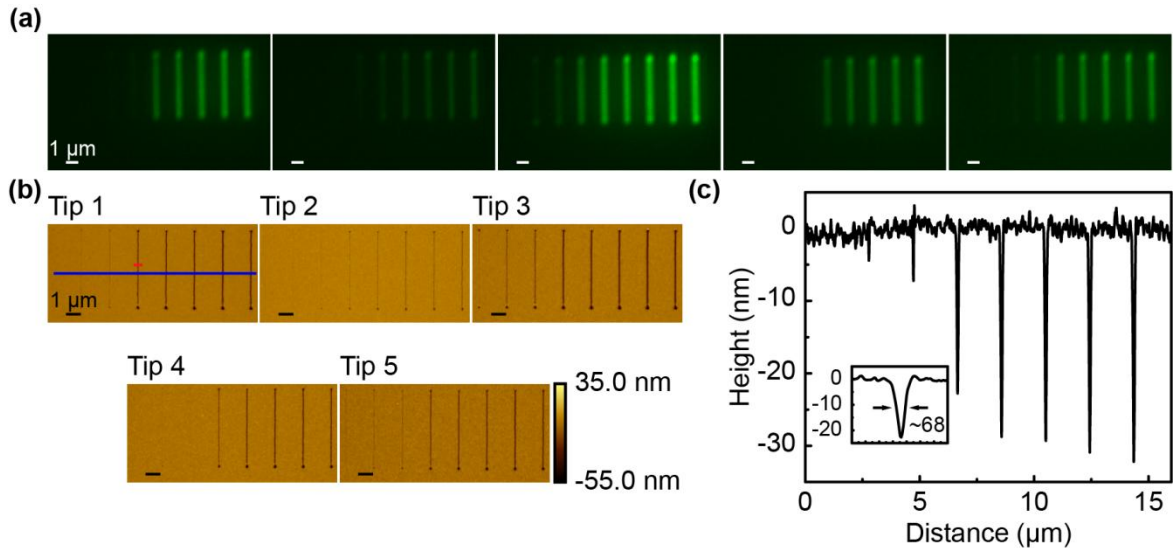


Figure 5.4.2 Measurements of lines made in PPV-precursor film made with thermal cantilever array (a) Fluorescent image of patterns of lines made with thermal cantilever array. (b) AFM image of patterns imaged in (a). (c) Topography profile for Tip 1 (indicated in blue in (a)), inset indicates a resolution of about 68 nm.

5.5 Thermal Imaging

Thermal cantilevers have the unique ability to both write and read the surface through the integrated heater. Metrology of surface variation is useful to verify thermal lithography and make alterations as needed[57]. While we have described and present the mechanisms for TCNL writing, central to thermal imaging is the energy transfer

between tip and substrate. This transfer induces a measureable effect based on the substrate composition and topography. More specifically, the tip-substrate interaction manifests as a change in the thermal cantilevers electronic properties, namely the cantilever's resistance. Small changes in the resistance register variations in the surface topography, and while the mapping is not perfect, thermal topography imaging provides a qualitative method to confirm lithographic patterning. To understand the mechanisms and principles of thermal imaging, we start with a single cantilever to display the most important features, and then expand the concept to arrays.

5.5.1 Thermal Imaging with a Single Tip

To demonstrate thermal imaging, a single cantilever is brought into contact with an AFM z-calibration grating. While in principle we could pattern a substrate and measure the change, the materials presented in this work are not conducive for this since they are thermally reactive; in place we use an AFM z-calibration grating. A z-calibration grating is a repetitive square corrugated substrate, which simplifies the analysis and interpretation of thermal imaging. By biasing the tip with a constant voltage and measuring the resistance as the tip rasters the surface, the change in resistance maps out changes in the topography. The results are shown in Figure 5.5.1, where the relative changes in the resistance are shown. Also shown in Figure 5.5.1 is a contact mode image of the same area. The changes in resistance correspond to the changes in topography. The troughs of the calibration grating have a lower resistance than the peaks; in the valleys, there is an increased heat transfer between the cantilever and the substrate. With an increased heat flux out of the cantilever, the temperature in the heater region lowers, and as explained in chapter 3, a lower temperature corresponds to a lower resistance. The effect is reversed for the peaks, where there is less heat transfer and correspondingly a higher temperature and resistance. Interestingly, this thermal imaging mode, also measures the speck of dust seen in the topographic figure. The resistance is highest on

the dust since the tip is furthest away from the substrate. Using this technique, resistance, R , sensitivities ($\Delta R/R$) in vertical resolutions down to 10^{-6} - 10^{-5} /nm have been reported[54]; with a modified version, vertical resolutions less than 1 nm have been shown[149].

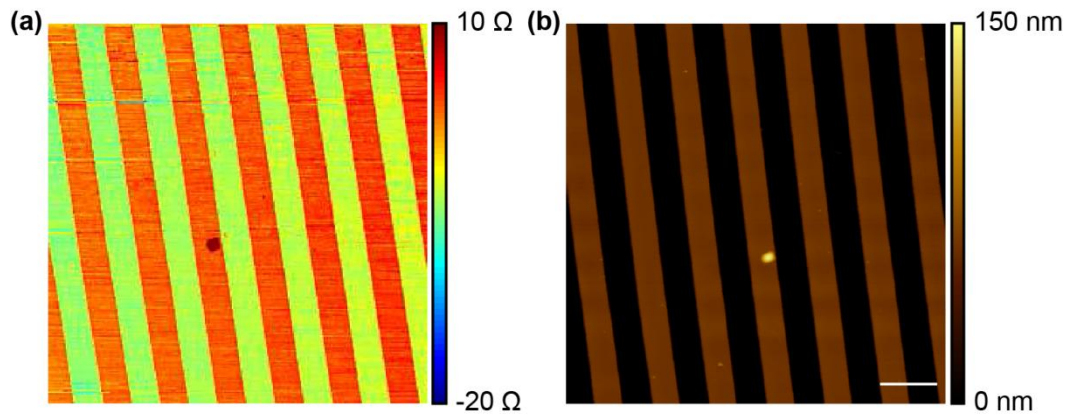


Figure 5.5.1 (a) Thermal imaging of a z-calibration grating with a single tip (b) AFM image of the same area measured in (a).

5.5.2 Thermal Imaging with Arrays

The same mechanisms to do thermal imaging with a single tip apply to the cantilever arrays. After aligning the tips with substrate, all five tips are simultaneously rastered across a z-calibration, and because each tip is individually addressable, the changes in resistance map out the local tip's topography. The results are shown in Figure 5.5.2. The sharp edges seen in the optical feedback AFM image and the thermal image for a single tip seen in Figure 5.5.1 are present in Figure 5.5.2. It should be noted that in Figure 5.5.2, although the images look contiguous and connected, this is purely coincidental. In fact there is about 110 μm between each cantilever as can be measured from Figure 5.4.1a. Techniques and methods for image stitching do exist[150], but since

the intent is to demonstrate simultaneous imaging, this suffices. Metrology of surfaces is especially valuable for situations in which corrections to lithographic patterning may be needed[57].

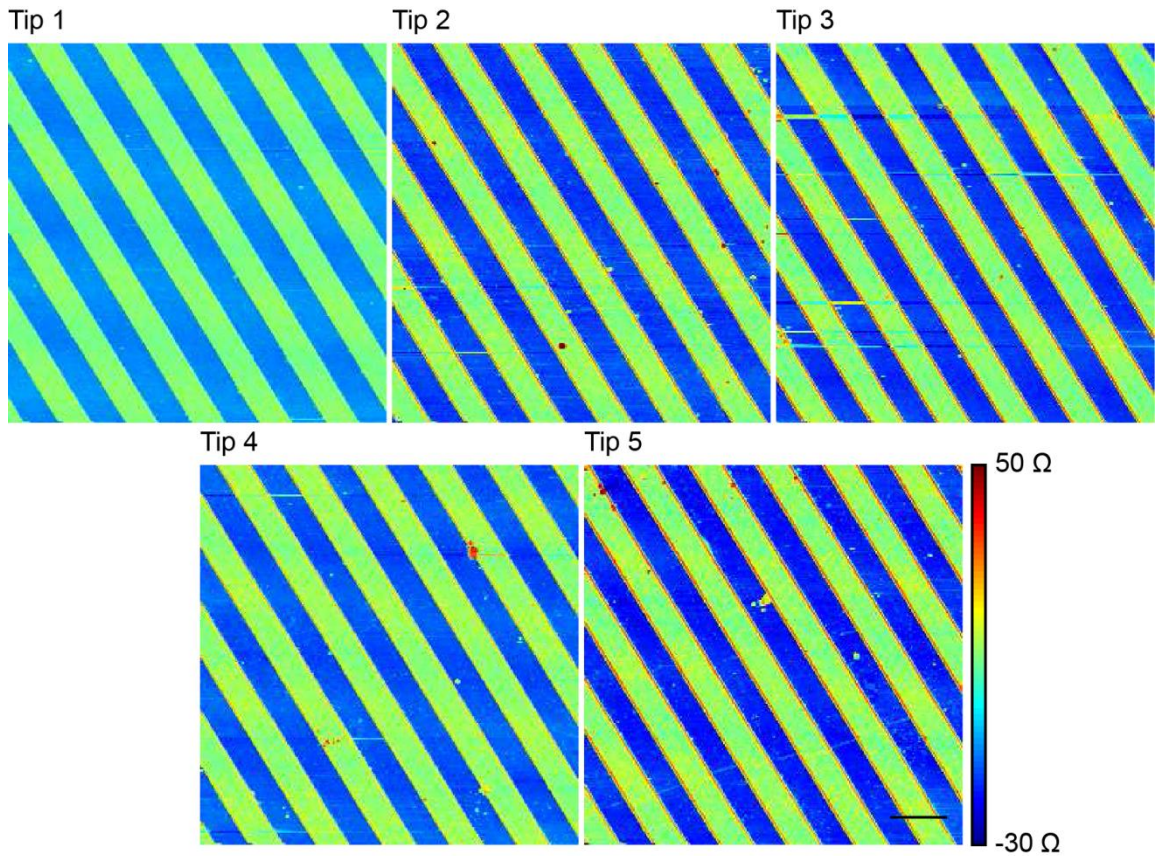


Figure 5.5.2 Thermal image obtained from a z-calibration grating with a thermal cantilever array.

5.6 Complications with Arrays

Despite the nice results discussed and displayed in this section, there are several unavoidable complications associated with the current thermal array setup. While leveling does a lot to maintain the tips being in contact with the surface concurrently, there are still situations in which one tip may lose contact with the surface. The

mechanism used in this chapter to overcome this limitation was to increase the load to insure all tips maintained contact; however, this can have adverse effects such as a worsening of the resolution or faster tip wear. The inability to control the loading force also makes controlled chemical reactions difficult since increased loads increase the efficiency parameter[108]; this leads to a less effective control as to how heater temperature will transformation a substrate. More work needs to be done to alleviate these issues, and possible solutions include coupling a second heater (such as those used by IBM[151]) with the Lorenz magnetic force[105].

The second issue is that there is some cross-talk between the cantilevers[145]. Experimental measurements have shown that the cross-talk is close to linear and the cross-talk seems to follow a superposition rule when multiple cantilevers are activated. In order to alleviate these issues, the thermal cantilevers could be run in a closed loop operation[149].

5.7 Final Word

This chapter set out to describe and show proof of principle parallelization of TCNL patterning. Using an array of thermal cantilevers, the ability to read and write to a surface were demonstrated. While little work was done to demonstrate the concepts in discussed in chapter 2-4, complex patterning with individually addressable cantilevers indicates that similar principles could be adapted and modified for thermal arrays. Future works with arrays may include taking into account the complications discussed.

CHAPTER 6

CONCLUSIONS AND FUTURE WORKS

6.1 Introduction

The goal of this thesis was to develop TCNL to fabricate controlled chemical and topographic gradients that span from the nano-scale to the micro-scale. In order to do this, we started described and applied a chemical kinetics model to TCNL, and then we exploited the model to control chemical reactions down to the nano-scale. In this thesis, we developed a systematic approach to study and demonstrate how temperature and speed affect the localized, TCNL induced chemical reaction both on the surface and into the body of the substrate. In this chapter, we summarize chapters 2-5, emphasize areas needing improvement, and discuss applications for chemical and topographic gradients.

6.2 Review

In chapter 2, we identified and adapted a chemical kinetics model to explain the key physical principles of TCNL. Our modified model accounted for tip motion and we derived a probability equation to predict the evolution of a thermally induced chemical reaction. The model showed that the essential component to TCNL's high resolution was the coupling between the temperature profile and the solution of the chemical kinetics equation. While the temperature profile is difficult to compute, we assumed a decaying profile and approximated a decay length with previous empirical data.

In chapter 3, we apply the results derived in chapter 2 to surface reaction. We combined a thermally activated polymer substrate with quantitative fluorescent microscopy to measure TCNL induced surface concentration. We compared the fluorescent results against the model, and we showed excellent agreement to our predictions in chapter 2. The dependencies on temperature and speed were exploited to

create and design spatially extended patterns of varying chemical concentrations, and the designed patterns demonstrated high levels accuracy on short length scales (sub micron).

Chapter 4 moved away from studying surface only effects and expanded the model to account for 3-D effects. This is a meaningful contribution to TCNL since patterning of other material properties requires control beyond the surface. The chemical kinetics equations from chapter 2 were modified versions to account for 3-D effects, and using a film of a semi-conducting precursor, z-dependence was semi-quantified using two physically different but measureable effects manifesting from the TCNL process. The long term impact of this work was the ability to expand the developed analysis to other material properties and this would be useful for situations where the techniques impart patterns not easily translated to fluorescent microscopy.

Finally, in chapter 5, we showed proof of principle parallelization of TCNL. The work in that chapter indicated that despite some of the complications associated with working with arrays (such as leveling or parallel reading), parallelization of TCNL works without much loss in the high resolutions. Though there is work to be done, parallelization is a powerful tool to make TCNL an attractive candidate for large scale applications.

6.3 Future Works and Improvements

The results shown throughout this work showed good agreement and an impressive amount of control over such short length scales. Future works on chemical kinetics modeling should look to expand alleviate some of the assumptions and exploit some of the extra factors that were ignored. There would be much to gain from finding or computing a better approximation to the temperature profile. The y/z dependence or the exact speed dependence, for example, could be derived. Verification of the computed temperature profile could be done by comparing against empirical investigations of individual points[96] or against line resolutions. These studies should

also include comparing different conditions such as film thickness or the thermal conductivity of the underlying substrate, and these studies could be applied to be surface and 3-D effects.

Future works on surface reactions include taking into account polymer motion. In chapter 3, we ignored polymer melting because of the increased glass transition temperature from the polymer's self-crosslinking. There has been some work done in connection with thermomechanical lithography regarding glass transition of polymer films[52, 96]. Coupling these results and studies with chemical kinetics works could effectively be used to predict an average polymer motion. This type of study, however, would be difficult since the exact relationship between the surface and 3-D effects would be needed.

For chapter 3 (and 4) we ignore the dependence in the y-direction because our patterning technique wrote consecutive lines smaller than the measured FWHM from FFM. By accounting for the y-direction, future works could improve upon designing profiles of chemical concentration. In those chapters, we also worked at speeds lower than 10 mm/s to assume an instantaneous temperature profile for the given the time scales[91], but future works could try to exploit time dependence to improve spatial resolutions.

Other factors that were not varied in this work are film thickness[152], surrounding medium[102, 153], substrate conductivity[94], and load dependent phenomena[108]. Film thickness studies should be studied in relation with 3-D effects and the temperature profile. Using vacuum chambers or changing the medium from air to another form such as liquids or a more conductive gas may change the resolutions or even some of the dynamics since medium effects enhance or dampen reactions such as in catalytic processes[154]. Throughout this work, load effects were ignored, but there is some evidence that increasing the load alters the dynamics at the tip-surface interface. The efficiency parameter, for example, has been shown to increase with increased

load[108]. Nano-shaving and nano-grafting techniques have also shown that shearing forces can selectively cleave bonds[155-156], and it is conceivable that by varying load, the effect may manifest in a way analogous to a catalyst, which raises or lowers a reaction's activation energy.

6.4 Applications of Chemical Gradients

The ability to create controlled chemical concentration profiles down to the mesoscopic scales offers a number of new applications[15]. Several applications are discussed in this section, and while some of these studies have been done on the micro-scale or larger, the ability to controllably shrink these phenomena down may offer new results.

6.4.1 Surface Energy Gradients

There have been several studies dedicated to examining how gradients in surface concentrations have induced droplet motion. For example, water has been observed to run “uphill” because of gradient profiles in the hydrophobicity/hydrophilicity of the surface[12]. Inclines up to about 15° have been demonstrated. Some of these works have been done with geometric arrangements in material properties[11], but there has been some work done with chemical concentration gradients[15]. By introducing profiles with linear gradients, motion of water droplets could be controlled[157]. The length scales usually associated with these types of studies are on the order of centimeters or larger.

TCNL is a well suited candidate to fulfill this niche, since it can reach small length scales and has been demonstrated to achieve controllable profiles. Additionally, with the demonstrated 2-D control, TCNL could introduce chemical gradients that alter droplet motion, and interesting studies could include how colloidal droplets combine.

6.4.2 Biophysical Applications

Chemical gradients have been shown to induce cellular activity and directional growth. For example, surface chemical gradients of fibronectin increase cellular migration, and increasing the magnitude of the gradient increased migration speed[158]. The one drawback to these studies, however, is the inability to extend towards sharp enough gradients to see if cellular migration was bound[159]. Due to the achievable length scales, TCNL could pattern substrates with sharp enough gradients to observe these effects.

Neuronal axon growth shows preference to gradients in the protein laminin[10, 31]. Gradients of laminin are obvious candidates for creating neural networks to study inter-neural responses. TCNL is an interesting candidate for this type of study, since gradients at different length scales and with different magnitudes could be made to see how the axons are affected. Some preliminary work is currently underway in collaboration with several labs.

Polymers exhibit different properties dependent on their grafting densities[160]. Chemical gradients have been used to study the transition from the mushroom regime to polymer brush regime[15, 160]; the transition is estimated to take place around the radius of gyration of the polymer[161]. Due to the small scale TCNL is capable of, it is possible to experimentally measure and vary the length scales down to which this transition occurs; a study of this form could also take into account the effects from solvents.

6.5 Applications of Topographic Gradients

Topographic gradients are valuable for a number of different interesting applications and studies. Most of the applications suggested here involve water or another solvents, and for these particular applications, the precursor film is not optimal since it is soluble in water and some organic solvents, such as methanol. To alleviate this

issue, we first discuss and demonstrated a technique similar to one used in microcontact printing[20].

6.5.1 Transfer PPV Patterns to PDMS

While the work done in chapter 4 showed the ability to create topographic gradients, the precursor film is not very conducive for some applications since it is easily dissolved in water and some organic solvents (particularly methanol). Moreover, the films were observed to have a short shelf life, presumably because the polymer film undergoes the chemical transformation slowly at room temperature.

To prolong the lifetime of the topographic gradients, a process used in microcontact and nano-contact printing was developed. The steps are shown in figure 6.5.1. First a substrate is patterned with a desired topographic gradient. Next an uncured elastomeric material (polydimethylsiloxane, PDMS, as labeled in the figure) filled in the mold formed in the precursor film. The sample was placed in a vacuum chamber to remove all air bubbles and then placed in an oven ($\sim 60^{\circ}$ C) for about an hour (steps not shown). The temperature was kept low to prevent the transformation of the PPV-precursor to PPV. Finally the cured elastomeric material was removed from the sample, leaving an impression of the substrate's topographic patterns. It should be noted that the process, just as in microcontact printing, inverts the patterns in the mold.

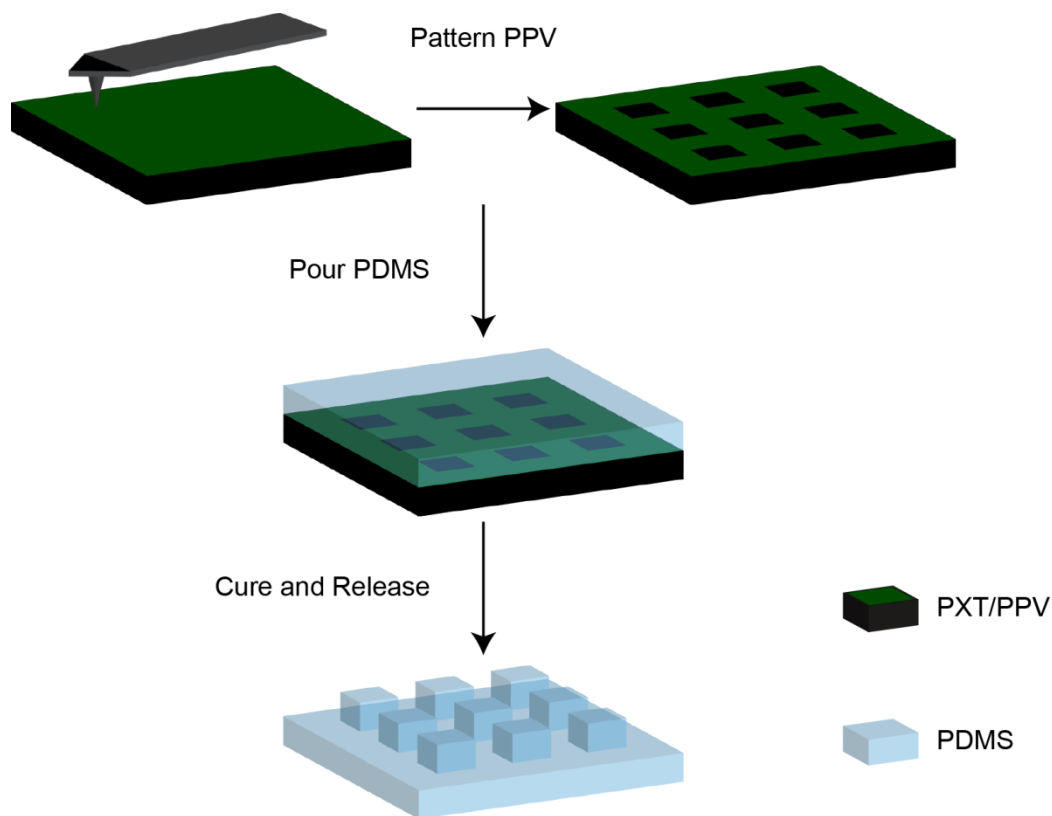


Figure 6.5.1 Schematic showing transfer of PPV topographic pattern to PDMS.

Figure 6.5.2 shows some preliminary evidence of this process. The initial PPV film is shown in Figure 6.5.2a patterned with an array of squares. After the transfer process is completed, the elastomeric material was imaged with an AFM. The imprinted patterns are shown in Figure 6.5.2b, and as expected, the square pattern is now inverted. This is a proof of principle demonstration, but it shows promise since some interesting features, such as the edges are present. While this technique requires some optimization, this demonstrates the ability to replicate topographic patterns for other applications.

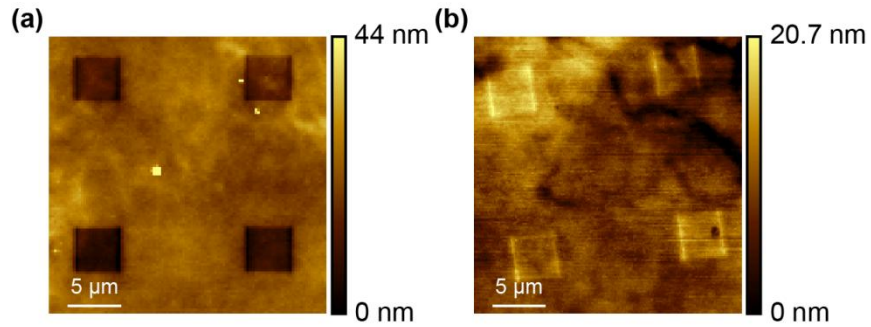


Figure 6.5.2 Experimental evidence showing the transfer of (a) PXT/PPV topographic patterns to (b) PDMS.

6.5.2 Colloidal Patterning

The ability to strategically place colloids holds promise for a number of fields such as photonic crystals[162-163]. There are several studies that use topographic variations to site specifically place colloids[164]. In these studies, researchers take a substrate patterned with grooves and pits and incubate the substrate with a colloidal solution[165]. The colloids stick everywhere, but by spinning the surface, colloids not trapped in the grooves or pits fly off. The trapped colloids remain in the forms of the pits and grooves. Interestingly, at different speeds and heights, colloids of different sizes can be trapped. Other interesting applications come from using directed interactions between colloids[166-167].

6.5.3 Nano-Fluidics

Nano-fluidic devices hold a promise for a variety of fields. Studies on the electrokinetic effects are fascinating since the small scales associated with the nano-channels are approaching the Debye length for the electric double layer[168]. Because of this, nano-fluidic devices have different conductivities than microfluidic devices at similar ionic concentrations[169]. One of the issues, however, with nano-channels is the ability to *affordably*[169] produce 1-D and 2-D nano-channels, but with the ability to

replicate topographic patterns, TCNL is formidable candidate for these types of studies and applications.

6.6 Final Word

We highlight various improvements and applications for TCNL fabricated gradients. While there remains much to do to optimize the technique, the ability to control various material properties down to nano-scale lengths holds promise for a number of interesting areas.

We set out to develop a systematic approach to control TCNL to alter material transformations down to nano-scale. While the work was demonstrated on two different organic polymer materials, the techniques and systematic approach developed caters to the plethora of materials which are suitable candidates for TCNL. By knowing how material properties vary with a chemical transformation, a chemical kinetics model can be applied to predict and control the substrate reaction, and because of this versatility and compatibility with other materials, TCNL is a unique and powerful lithographic technique.

APPENDIX A

DERIVATION OF EQ. 4.2.11

We start with by plugging eq. 4.2.10 into eq. 4.2.8:

$$Pr(z) = 1 - e^{-\frac{k_o \cdot s \cdot z}{v \cdot \kappa}}$$
(A.1)

We plug eq. A.1 into the modified body eq. 4.2.3:

$$Pr_{body} = \frac{N}{N_{tot}} = \frac{\int Pr dz}{\int dz} = \frac{\int Pr(z) dz}{L} = \frac{\int_0^L 1 - e^{-\frac{k_o \cdot s \cdot z}{v \cdot \kappa}} dz}{L}$$
(A.2)

where the integral is over the film thickness. Writing out the Taylor expansion for an exponential series:

$$e^x = \sum_{n=0}^{\infty} \frac{x^n}{n!}$$

We use this form for A.2:

$$Pr_{body} = 1 - \frac{\int_0^L \sum \frac{\left(-\frac{k_o \cdot s \cdot z}{v \cdot \kappa}\right)^n}{n!} dz}{L} = 1 - \sum_{n=0}^{\infty} \frac{\int_0^L \left(-\frac{k_o \cdot s \cdot z}{v \cdot \kappa}\right)^n dz}{n!}$$
(A.3)

Eq. A.3 can be integrated to:

$$Pr_{body} = \frac{\kappa}{L} \left(\sum_{n=1}^{\infty} \frac{\left(-\frac{k_o \cdot s \cdot L}{v \cdot \kappa}\right)^n}{n \cdot n!} - \sum_{n=1}^{\infty} \frac{\left(-\frac{k_o \cdot s}{v}\right)^n}{n \cdot n!} \right)$$
(A.4)

The definition of the exponential integral is given as [170]:

$$Ei(x) = \int_x^\infty \frac{e^{-x}}{x} dx = -\gamma - \ln|x| - \sum_{n=1}^{\infty} \frac{(-x)^n}{n \cdot n!} \quad (\text{A.5})$$

where gamma is the Euler-Mascheroni constant. Using this form, we can reduce eq. A.4 to:

$$Pr = \left(Ei\left(\frac{k_0}{v} e^{-\frac{L}{\kappa}}\right) + \ln\left(\frac{k_0}{v} e^{-\frac{L}{\kappa}}\right) - Ei\left(\frac{k_0}{v}\right) - \ln\left(\frac{k_0}{v}\right) \right) \cdot \frac{\kappa}{L} \quad (4.2.11)$$

REFERENCES

- [1] Gil, D.; Brunner, T. A.; Fonseca, C.; Seong, N.; Streefkerk, B.; Wagner, C.; Stavenga, M. In *Immersion Lithography: New Opportunities for Semiconductor Manufacturing*, San Diego, California (USA), AVS: San Diego, California (USA), 2004; pp 3431-3438.
- [2] Mendes, P.; Yeung, C.; Preece, J., Bio-Nanopatterning of Surfaces. *Nanoscale Research Letters* **2007**, *2*, 373-384.
- [3] Füstner, R.; Barthlott, W.; Neinhuis, C.; Walzel, P., Wetting and Self-Cleaning Properties of Artificial Superhydrophobic Surfaces. *Langmuir* **2005**, *21*, 956-961.
- [4] Allara, D. L., A Perspective on Surfaces and Interfaces. *Nature* **2005**, *437*, 638-639.
- [5] Hullmann, A.; Meyer, M., Publications and Patents in Nanotechnology. *Scientometrics* **2003**, *58*, 507-527.
- [6] Son, Y.-W.; Cohen, M. L.; Louie, S. G., Energy Gaps in Graphene Nanoribbons. *Physical Review Letters* **2006**, *97*, 216803.
- [7] Falconnet, D.; Pasqui, D.; Park, S.; Eckert, R.; Schiff, H.; Gobrecht, J.; Barbucci, R.; Textor, M., A Novel Approach to Produce Protein Nanopatterns by Combining Nanoimprint Lithography and Molecular Self-Assembly. *Nano Lett.* **2004**, *4*, 1909-1914.
- [8] Xia, Y.; Whitesides, G. M., Soft Lithography. *Annual review of materials science* **1998**, *28*, 153-184.
- [9] Belisle, J. M.; Correia, J. P.; Wiseman, P. W.; Kennedy, T. E.; Costantino, S., Patterning Protein Concentration Using Laser-Assisted Adsorption by Photobleaching, Lapap. *Lab Chip* **2008**, *8*, 2164-2167.
- [10] Dertinger, S. K. W.; Jiang, X.; Li, Z.; Murthy, V. N.; Whitesides, G. M., Gradients of Substrate-Bound Laminin Orient Axonal Specification of Neurons. *Proceedings of the National Academy of Sciences* **2002**, *99*, 12542-12547.
- [11] Zhang, J.; Han, Y., Shape-Gradient Composite Surfaces: Water Droplets Move Uphill. *Langmuir* **2007**, *23*, 6136-6141.
- [12] Chaudhury, M. K.; Whitesides, G. M., How to Make Water Run Uphill. *Science* **1992**, *256*, 1539-1541.
- [13] Lafuma, A.; Quéré, D., Superhydrophobic States. *Nat Mater* **2003**, *2*, 457-460.

- [14] Chu, R. C.; Simons, R. E.; Ellsworth, M. J.; Schmidt, R. R.; Cozzolino, V., Review of Cooling Technologies for Computer Products. *Device and Materials Reliability, IEEE Transactions on* **2004**, *4*, 568-585.
- [15] Morgenthaler, S.; Zink, C.; Spencer, N. D., Surface-Chemical and -Morphological Gradients. *Soft Matter* **2008**, *4*, 419-434.
- [16] Zhou, X.; Boey, F.; Huo, F.; Huang, L.; Zhang, H., Chemically Functionalized Surface Patterning. *Small* **2011**, *7*, 2273-2289.
- [17] Bernard, A.; Renault, J. P.; Michel, B.; Bosshard, H. R.; Delamarche, E., Microcontact Printing of Proteins. *Adv. Mater.* **2000**, *12*, 1067-1070.
- [18] Rozkiewicz, D. I.; Gierlich, J.; Burley, G. A.; Gutmiedl, K.; Carell, T.; Ravoo, B. J.; Reinhoudt, D. N., Transfer Printing of DNA by “Click” Chemistry. *ChemBioChem* **2007**, *8*, 1997-2002.
- [19] Mrksich, M.; Whitesides, G. M., Patterning Self-Assembled Monolayers Using Microcontact Printing: A New Technology for Biosensors? *Trends in Biotechnology* **1995**, *13*, 228-235.
- [20] Mrksich, M.; Dike, L. E.; Tien, J.; Ingber, D. E.; Whitesides, G. M., Using Microcontact Printing to Pattern the Attachment of Mammalian Cells to Self-Assembled Monolayers of Alkanethiolates on Transparent Films of Gold and Silver. *Experimental Cell Research* **1997**, *235*, 305-313.
- [21] Lange, S. A.; Benes, V.; Kern, D. P.; Hörber, J. K. H.; Bernard, A., Microcontact Printing of DNA Molecules. *Anal. Chem.* **2004**, *76*, 1641-1647.
- [22] Hui, C. Y.; Jagota, A.; Lin, Y. Y.; Kramer, E. J., Constraints on Microcontact Printing Imposed by Stamp Deformation. *Langmuir* **2002**, *18*, 1394-1407.
- [23] Li, H.-W.; Muir, B. V. O.; Fichet, G.; Huck, W. T. S., Nanocontact Printing: A Route to Sub-50-Nm-Scale Chemical and Biological Patterning. *Langmuir* **2003**, *19*, 1963-1965.
- [24] Kraus, T.; Stutz, R.; Balmer, T. E.; Schmid, H.; Malaquin, L.; Spencer, N. D.; Wolf, H., Printing Chemical Gradients. *Langmuir* **2005**, *21*, 7796-7804.
- [25] Shaw, J. M.; Gelorme, J. D.; LaBianca, N. C.; Conley, W. E.; Holmes, S. J., Negative Photoresists for Optical Lithography. *IBM Journal of Research and Development* **1997**, *41*, 81-94.
- [26] Wu, B.; Kumar, A., Extreme Ultraviolet Lithography: A Review. *Journal of Vacuum Science & Technology B: Microelectronics and Nanometer Structures* **2007**, *25*, 1743-1761.

- [27] Switkes, M.; Rothschild, M. In *Immersion Lithography at 157 Nm*, Washington, DC (USA), AVS: Washington, DC (USA), 2001; pp 2353-2356.
- [28] Scrimgeour, J.; Kodali, V. K.; Kovari, D. T.; Curtis, J. E., Photobleaching-Activated Micropatterning on Self-Assembled Monolayers. *J. Phys.: Condens. Matter* **2010**, *22*, 194103.
- [29] Holden, M. A.; Cremer, P. S., Light Activated Patterning of Dye-Labeled Molecules on Surfaces. *J. Am. Chem. Soc.* **2003**, *125*, 8074-8075.
- [30] Waldbaur, A.; Waterkotte, B.; Schmitz, K.; Rapp, B. E., Maskless Projection Lithography for the Fast and Flexible Generation of Grayscale Protein Patterns. *Small* **2012**, *8*, 1570-1578.
- [31] Dertinger, S. K. W.; Chiu, D. T.; Jeon, N. L.; Whitesides, G. M., Generation of Gradients Having Complex Shapes Using Microfluidic Networks. *Anal. Chem.* **2001**, *73*, 1240-1246.
- [32] Mendes, P. M.; Jacke, S.; Critchley, K.; Plaza, J.; Chen, Y.; Nikitin, K.; Palmer, R. E.; Preece, J. A.; Evans, S. D.; Fitzmaurice, D., Gold Nanoparticle Patterning of Silicon Wafers Using Chemical E-Beam Lithography. *Langmuir* **2004**, *20*, 3766-3768.
- [33] Zhang, G.-J.; Tanii, T.; Zako, T.; Hosaka, T.; Miyake, T.; Kanari, Y.; Funatsu, T.; Ohdomari, I., Nanoscale Patterning of Protein Using Electron Beam Lithography of Organosilane Self-Assembled Monolayers. *Small* **2005**, *1*, 833-837.
- [34] Broers, A. N.; Hoole, A. C. F.; Ryan, J. M., Electron Beam Lithography—Resolution Limits. *Microelectronic Engineering* **1996**, *32*, 131-142.
- [35] Christman, K. L.; Enriquez-Rios, V. D.; Maynard, H. D., Nanopatterning Proteins and Peptides. *Soft Matter* **2006**, *2*, 928-939.
- [36] Vieu, C.; Carcenac, F.; Pépin, A.; Chen, Y.; Mejias, M.; Lebib, A.; Manin-Ferlazzo, L.; Couraud, L.; Launois, H., Electron Beam Lithography: Resolution Limits and Applications. *Applied Surface Science* **2000**, *164*, 111-117.
- [37] Fujita, J.; Ohnishi, Y.; Ochiai, Y.; Matsui, S., Ultrahigh Resolution of Calixarene Negative Resist in Electron Beam Lithography. *Appl. Phys. Lett.* **1996**, *68*, 1297-1299.
- [38] Grigorescu, A. E.; Hagen, C. W., Resists for Sub-20-Nm Electron Beam Lithography with a Focus on Hsq: State of the Art. *Nanotechnol.* **2009**, *20*, 292001.
- [39] Shi, J.; Chen, J.; Cremer, P. S., Sub-100 Nm Patterning of Supported Bilayers by Nanoshaving Lithography. *J. Am. Chem. Soc.* **2008**, *130*, 2718-2719.

- [40] Liu, M.; Amro, N. A.; Chow, C. S.; Liu, G.-y., Production of Nanostructures of DNA on Surfaces. *Nano Lett.* **2002**, *2*, 863-867.
- [41] Tinazli, A.; Piehler, J.; Beuttler, M.; Guckenberger, R.; Tampé, R., Native Protein Nanolithography That Can Write, Read and Erase. *Nature Nanotechnol.* **2007**, *2*, 220-225.
- [42] Fresco, Z. M.; Suez, I.; Backer, S. A.; Fréchet, J. M. J., Afm-Induced Amine Deprotection: Triggering Localized Bond Cleavage by Application of Tip/Substrate Voltage Bias for the Surface Self-Assembly of Nanosized Dendritic Objects. *J. Am. Chem. Soc.* **2004**, *126*, 8374-8375.
- [43] Maoz, R.; Cohen, S. R.; Sagiv, J., Nanoelectrochemical Patterning of Monolayer Surfaces: Toward Spatially Defined Self-Assembly of Nanostructures. *Adv. Mater.* **1999**, *11*, 55-61.
- [44] Fuierer, R. R.; Carroll, R. L.; Feldheim, D. L.; Gorman, C. B., Patterning Mesoscale Gradient Structures with Self-Assembled Monolayers and Scanning Tunneling Microscopy Based Replacement Lithography. *Adv. Mater.* **2002**, *14*, 154-157.
- [45] Piner, R. D.; Zhu, J.; Xu, F.; Hong, S.; Mirkin, C. A., "Dip-Pen" Nanolithography. *Science* **1999**, *283*, 661-663.
- [46] Lee, K.-B.; Park, S.-J.; Mirkin, C. A.; Smith, J. C.; Mrksich, M., Protein Nanoarrays Generated by Dip-Pen Nanolithography. *Science* **2002**, *295*, 1702-1705.
- [47] Ginger, D. S.; Zhang, H.; Mirkin, C. A., The Evolution of Dip-Pen Nanolithography. *Angew. Chem. Int. Edn* **2004**, *43*, 30-45.
- [48] Mirkin, C. A., The Power of the Pen: Development of Massively Parallel Dip-Pen Nanolithography. *ACS Nano* **2007**, *1*, 79-83.
- [49] Hong, S.; Zhu, J.; Mirkin, C. A., Multiple Ink Nanolithography: Toward a Multiple-Pen Nano-Plotter. *Science* **1999**, *286*, 523-525.
- [50] Salaita, K.; Wang, Y.; Fragala, J.; Vega, R. A.; Liu, C.; Mirkin, C. A., Massively Parallel Dip-Pen Nanolithography with 55 000-Pen Two-Dimensional Arrays. *Angewandte Chemie* **2006**, *118*, 7378-7381.
- [51] Nelson, B. A.; King, W. P., Temperature Calibration of Heated Silicon Atomic Force Microscope Cantilevers. *Sens. Actuators, A* **2007**, *140*, 51-59.
- [52] Vettiger, P.; Cross, G.; Despont, M.; Drechsler, U.; Durig, U.; Gotsmann, B.; Haberle, W.; Lantz, M. A.; Rothuizen, H. E.; Stutz, R., et al., The "Millipede" - Nanotechnology Entering Data Storage. *Nanotechnology, IEEE Transactions on* **2002**, *1*, 39-55.

- [53] Vettiger, P.; Despont, M.; Drechsler, U.; Durig, U.; Haberle, W.; Lutwyche, M. I.; Rothuizen, H. E.; Stutz, R.; Widmer, R.; Binnig, G. K., The "Millipede"-More Than Thousand Tips for Future Afm Storage. *IBM Journal of Research and Development* **2000**, *44*, 323-340.
- [54] Binnig, G.; Despont, M.; Drechsler, U.; Haberle, W.; Lutwyche, M.; Vettiger, P.; Mamin, H. J.; Chui, B. W.; Kenny, T. W., Ultrahigh-Density Atomic Force Microscopy Data Storage with Erase Capability. *Appl. Phys. Lett.* **1999**, *74*, 1329-1331.
- [55] Pires, D.; Hedrick, J. L.; De Silva, A.; Frommer, J.; Gotsmann, B.; Wolf, H.; Despont, M.; Duerig, U.; Knoll, A. W., Nanoscale Three-Dimensional Patterning of Molecular Resists by Scanning Probes. *Science* **2010**, *328*, 732-735.
- [56] Knoll, A. W.; Pires, D.; Coulembier, O.; Dubois, P.; Hedrick, J. L.; Frommer, J.; Duerig, U., Probe-Based 3-D Nanolithography Using Self-Amplified Depolymerization Polymers. *Adv. Mater.* **2010**, *22*, 3361-3365.
- [57] Hua, Y.; Saxena, S.; Henderson, C. L.; King, W. P., Nanoscale Thermal Lithography by Local Polymer Decomposition Using a Heated Atomic Force Microscope Cantilever Tip. *Journal of Micro/Nanolithography, MEMS, and MOEMS* **2007**, *6*, 023012-023012.
- [58] Carroll, K. M.; Giordano, A. J.; Wang, D.; Kodali, V. K.; Scrimgeour, J.; King, W. P.; Marder, S. R.; Riedo, E.; Curtis, J. E., Fabricating Nanoscale Chemical Gradients with Thermochemical Nanolithography. *Langmuir* **2013**, *29*, 8675-8682.
- [59] Fenwick, O.; Bozec, L.; Credginton, D.; Hammiche, A.; Lazzerini, G. M.; Silberberg, Y. R.; Cacialli, F., Thermochemical Nanopatterning of Organic Semiconductors. *Nature Nanotechnol.* **2009**, *4*, 664-668.
- [60] Fletcher, P. C.; Felts, J. R.; Dai, Z.; Jacobs, T. D.; Zeng, H.; Lee, W.; Sheehan, P. E.; Carlisle, J. A.; Carpick, R. W.; King, W. P., Wear-Resistant Diamond Nanoprobe Tips with Integrated Silicon Heater for Tip-Based Nanomanufacturing. *ACS Nano* **2010**, *4*, 3338-3344.
- [61] Nelson, B. A.; King, W. P.; Laracuate, A. R.; Sheehan, P. E.; Whitman, L. J., Direct Deposition of Continuous Metal Nanostructures by Thermal Dip-Pen Nanolithography. *Appl. Phys. Lett.* **2006**, *88*, 033104-3.
- [62] Sheehan, P. E.; Whitman, L. J.; King, W. P.; Nelson, B. A., Nanoscale Deposition of Solid Inks Via Thermal Dip Pen Nanolithography. *Appl. Phys. Lett.* **2004**, *85*, 1589-1591.
- [63] Lee, W. K.; Dai, Z.; King, W. P.; Sheehan, P. E., Maskless Nanoscale Writing of Nanoparticle-Polymer Composites and Nanoparticle Assemblies Using Thermal Nanoprobes. *Nano Lett.* **2009**, *10*, 129-133.

- [64] Wang, D.; Kodali, V. K.; Underwood, W. D., II; Jarvholm, J. E.; Okada, T.; Jones, S. C.; Rumi, M.; Dai, Z.; King, W. P.; Marder, S. R., et al., Thermochemical Nanolithography of Multifunctional Nanotemplates for Assembling Nano-Objects. *Adv. Funct. Mater.* **2009**, *19*, 3696-3702.
- [65] Wei, Z.; Wang, D.; Kim, S.; Kim, S.-Y.; Hu, Y.; Yakes, M. K.; Laracuate, A. R.; Dai, Z.; Marder, S. R.; Berger, C., et al., Nanoscale Tunable Reduction of Graphene Oxide for Graphene Electronics. *Science* **2010**, *328*, 1373-1376.
- [66] Lee, W.-K.; Haydell, M.; Robinson, J. T.; Laracuate, A. R.; Cimpoiasu, E.; King, W. P.; Sheehan, P. E., Nanoscale Reduction of Graphene Fluoride Via Thermochemical Nanolithography. *ACS Nano* **2013**, *7*, 6219-6224.
- [67] Kim, S.; Bastani, Y.; Lu, H.; King, W. P.; Marder, S.; Sandhage, K. H.; Gruverman, A.; Riedo, E.; Bassiri-Gharb, N., Direct Fabrication of Arbitrary-Shaped Ferroelectric Nanostructures on Plastic, Glass, and Silicon Substrates. *Adv. Mater.* **2011**, *23*, 3786-3790.
- [68] Szoszkiewicz, R.; Okada, T.; Jones, S. C.; Li, T.-D.; King, W. P.; Marder, S. R.; Riedo, E., High-Speed, Sub-15 Nm Feature Size Thermochemical Nanolithography. *Nano Lett.* **2007**, *7*, 1064-1069.
- [69] Wang, D. B.; Szoszkiewicz, R.; Lucas, M.; Riedo, E.; Okada, T.; Jones, S. C.; Marder, S. R.; Lee, J.; King, W. P., Local Wettability Modification by Thermochemical Nanolithography with Write-Read-Overwrite Capability. *Appl. Phys. Lett.* **2007**, *91*, 243104-3.
- [70] Wang, D.; Kim, S.; Underwood II, W. D.; Giordano, A. J.; Henderson, C. L.; Dai, Z.; King, W. P.; Marder, S. R.; Riedo, E., Direct Writing and Characterization of Poly(P-Phenylene Vinylene) Nanostructures. *Appl. Phys. Lett.* **2009**, *95*, 233108-3.
- [71] Gotsmann, B.; Duerig, U.; Frommer, J.; Hawker, C. J., Exploiting Chemical Switching in a Diels–Alder Polymer for Nanoscale Probe Lithography and Data Storage. *Adv. Funct. Mater.* **2006**, *16*, 1499-1505.
- [72] Paul, P. C.; Knoll, A. W.; Holzner, F.; Despont, M.; Duerig, U., Rapid Turnaround Scanning Probe Nanolithography. *Nanotechnol.* **2011**, *22*, 275306.
- [73] Chimmalgi, A.; Grigoropoulos, C. P.; Komvopoulos, K., Surface Nanostructuring by Nano-/Femtosecond Laser-Assisted Scanning Force Microscopy. *J. Appl. Phys.* **2005**, *97*, 104319-12.
- [74] Eigler, D. M.; Schweizer, E. K., Positioning Single Atoms with a Scanning Tunnelling Microscope. *Nature* **1990**, *344*, 524-526.
- [75] Milner, A. A.; Zhang, K.; Prior, Y., Floating Tip Nanolithography. *Nano Lett.* **2008**, *8*, 2017-2022.

- [76] Riehn, R.; Charas, A.; Morgado, J.; Cacialli, F., Near-Field Optical Lithography of a Conjugated Polymer. *Appl. Phys. Lett.* **2003**, *82*, 526-528.
- [77] Arnold, M.; Hirschfeld-Warneken, V. C.; Lohmüller, T.; Heil, P.; Blümmel, J.; Cavalcanti-Adam, E. A.; López-García, M. n.; Walther, P.; Kessler, H.; Geiger, B., et al., Induction of Cell Polarization and Migration by a Gradient of Nanoscale Variations in Adhesive Ligand Spacing. *Nano Lett.* **2008**, *8*, 2063-2069.
- [78] Spatz, J. P., Nano- and Micropatterning by Organic–Inorganic Templating of Hierarchical Self-Assembled Structures. *Angew. Chem. Int. Edn* **2002**, *41*, 3359-3362.
- [79] Zhu, X.; Mills, K. L.; Peters, P. R.; Bahng, J. H.; Liu, E. H.; Shim, J.; Naruse, K.; Csete, M. E.; Thouless, M. D.; Takayama, S., Fabrication of Reconfigurable Protein Matrices by Cracking. *Nature Materials* **2005**, *4*, 403-406.
- [80] Morgenthaler, S.; Lee, S.; Zürcher, S.; Spencer, N. D., A Simple, Reproducible Approach to the Preparation of Surface-Chemical Gradients. *Langmuir* **2003**, *19*, 10459-10462.
- [81] Huo, F.; Zheng, G.; Liao, X.; Giam, L. R.; Chai, J.; Chen, X.; Shim, W.; Mirkin, C. A., Beam Pen Lithography. *Nature Nanotechnol.* **2010**, *5*, 637-640.
- [82] Wu, E.-S.; Strickler, J. H.; Harrell, W. R.; Webb, W. W. In *Two-Photon Lithography for Microelectronic Application*, Optical/Laser Microlithography V, International Society for Optics and Photonics: 1992; pp 776-782.
- [83] Ito, T.; Okazaki, S., Pushing the Limits of Lithography. *Nature* **2000**, *406*, 1027-1031.
- [84] Marder, S. R.; Brédas, J.-L.; Perry, J. W., Materials for Multiphoton 3d Microfabrication. *MRS Bulletin* **2007**, *32*, 561-565.
- [85] Maalouf, A.; Gadonna, M.; Bosc, D., An Improvement in Standard Photolithography Resolution Based on Kirchhoff Diffraction Studies. *Journal of Physics D: Applied Physics* **2009**, *42*, 015106.
- [86] Hulett, J., Deviations from the Arrhenius Equation. *Quarterly Reviews, Chemical Society* **1964**, *18*, 227-242.
- [87] Laidler, K. J.; King, M. C., Development of Transition-State Theory. *The Journal of Physical Chemistry* **1983**, *87*, 2657-2664.
- [88] Laidler, K. J., The Development of the Arrhenius Equation. *Journal of Chemical Education* **1984**, *61*, 494.
- [89] Gardiner, W. C., Temperature Dependence of Bimolecular Gas Reaction Rates. *Accounts of Chemical Research* **1977**, *10*, 326-331.

- [90] Wang, D., *Thermochemical Nanolithography Fabrication and Atomic Force Microscopy Characterization of Functional Nanostructures [Electronic Resource]* / by Debin Wang. Atlanta, Ga. : Georgia Institute of Technology, 2010.: 2010.
- [91] King, W. P.; Goodson, K. E., Thermomechanical Formation of Nanoscale Polymer Indents with a Heated Silicon Tip. *Journal of Heat Transfer* **2007**, *129*, 1600-1604.
- [92] Lee, J.; Beechem, T.; Wright, T. L.; Nelson, B. A.; Graham, S.; King, W. P., Electrical, Thermal, and Mechanical Characterization of Silicon Microcantilever Heaters. *J. Microelectromechan. Sys.* **2006**, *15*, 1644-1655.
- [93] Chen, G., Ballistic-Diffusive Heat-Conduction Equations. *Physical Review Letters* **2001**, *86*, 2297-2300.
- [94] Nelson, B. A.; King, W. P., Modeling and Simulation of the Interface Temperature between a Heated Silicon Tip and a Substrate. *Nanoscale and Microscale Thermophysical Engineering* **2008**, *12*, 98-115.
- [95] Cahill, D. G.; Ford, W. K.; Goodson, K. E.; Mahan, G. D.; Majumdar, A.; Maris, H. J.; Merlin, R.; Phillpot, S. R., Nanoscale Thermal Transport. *J. Appl. Phys.* **2003**, *93*, 793-818.
- [96] DuVigneau, J.; Schönherr, H.; Vancso, G. J., Nanoscale Thermal Afm of Polymers: Transient Heat Flow Effects. *ACS Nano* **2010**, *4*, 6932-6940.
- [97] Escobar, R. A.; Ghai, S. S.; Jhon, M. S.; Amon, C. H., Multi-Length and Time Scale Thermal Transport Using the Lattice Boltzmann Method with Application to Electronics Cooling. *International Journal of Heat and Mass Transfer* **2006**, *49*, 97-107.
- [98] King, W. P.; Kenny, T. W.; Goodson, K. E.; Cross, G.; Despont, M.; Durig, U.; Rothuizen, H.; Binnig, G. K.; Vettiger, P., Atomic Force Microscope Cantilevers for Combined Thermomechanical Data Writing and Reading. *Appl. Phys. Lett.* **2001**, *78*, 1300-1302.
- [99] Chapuis, P.-O.; et al., Heat Transfer between a Nano-Tip and a Surface. *Nanotechnol.* **2006**, *17*, 2978.
- [100] Chui, B. W.; Stowe, T. D.; Yongho Sungtaek, J.; Goodson, K. E.; Kenny, T. W.; Mamin, H. J.; Terris, B. D.; Ried, R. P.; Rugar, D., Low-Stiffness Silicon Cantilevers with Integrated Heaters and Piezoresistive Sensors for High-Density Afm Thermomechanical Data Storage. *Microelectromechanical Systems, Journal of* **1998**, *7*, 69-78.

- [101] King, W. P., Design Analysis of Heated Atomic Force Microscope Cantilevers for Nanotopography Measurements. *Journal of Micromechanics and Microengineering* **2005**, *15*, 2441.
- [102] Lee, J.; Wright, T. L.; Abel, M. R.; Sunden, E. O.; Marchenkov, A.; Graham, S.; King, W. P., Thermal Conduction from Microcantilever Heaters in Partial Vacuum. *J. Appl. Phys.* **2007**, *101*, 014906-6.
- [103] Ravi, T. S.; Marcus, R. B.; Liu, D., Oxidation Sharpening of Silicon Tips. *Journal of Vacuum Science & Technology B: Microelectronics and Nanometer Structures* **1991**, *9*, 2733-2737.
- [104] Nafday, O. A.; Weeks, B. L.; King, W. P.; Lee, J., Inducing Nanoscale Morphology Changes of Pentaerythritol Tetranitrate Using a Heated Atomic Force Microscope Cantilever. *Journal of Energetic Materials* **2008**, *27*, 1-16.
- [105] Lee, B.; Prater, C. B.; King, W. P., Lorentz Force Actuation of a Heated Atomic Force Microscope Cantilever. *Nanotechnol.* **2012**, *23*, 055709.
- [106] Sernelius, B. E., Temperature-Dependent Resistivity of Heavily Doped Silicon and Germanium. *Physical Review B* **1990**, *41*, 3060-3068.
- [107] Chui, B. W.; Asheghi, M.; Ju, Y. S.; Goodson, K. E.; Kenny, T. W.; Mamin, H. J., Intrinsic-Carrier Thermal Runaway in Silicon Microcantilevers. *Microscale Thermophysical Engineering* **1999**, *3*, 217-228.
- [108] Lantz, M. A.; Gotsmann, B.; Durig, U. T.; Vettiger, P.; Nakayama, Y.; Shimizu, T.; Tokumoto, H., Carbon Nanotube Tips for Thermomechanical Data Storage. *Appl. Phys. Lett.* **2003**, *83*, 1266-1268.
- [109] Underwood, W. D., *A Thin Film Polymer System for the Patterning of Amines through Thermochemical Nanolithography [Electronic Resource] / by William David Underwood*. Atlanta, Ga. : Georgia Institute of Technology, 2009.: 2009.
- [110] King, W. P.; Kenny, T. W.; Goodson, K. E., Comparison of Thermal and Piezoresistive Sensing Approaches for Atomic Force Microscopy Topography Measurements. *Appl. Phys. Lett.* **2004**, *85*, 2086-2088.
- [111] McCafferty, E.; Wightman, J. P., Determination of the Concentration of Surface Hydroxyl Groups on Metal Oxide Films by a Quantitative Xps Method. *Surface and Interface Analysis* **1998**, *26*, 549-564.
- [112] Leggett, G. J.; Brewer, N. J.; Chong, K. S. L., Friction Force Microscopy: Towards Quantitative Analysis of Molecular Organisation with Nanometre Spatial Resolution. *Phys. Chem. Chem. Phys.* **2005**, *7*, 1107-1120.
- [113] Jares-Erijman, E. A.; Jovin, T. M., Fret Imaging. *Nat Biotech* **2003**, *21*, 1387-1395.

- [114] Stabley, D. R.; Jurchenko, C.; Marshall, S. S.; Salaita, K. S., Visualizing Mechanical Tension across Membrane Receptors with a Fluorescent Sensor. *Nat Meth* **2012**, *9*, 64-67.
- [115] Waters, J. C., Accuracy and Precision in Quantitative Fluorescence Microscopy. *The Journal of Cell Biology* **2009**, *185*, 1135-1148.
- [116] Doyle, C. D., Kinetic Analysis of Thermogravimetric Data. *J. Appl. Polym. Sci.* **1961**, *5*, 285-292.
- [117] Freeman, E. S.; Carroll, B., The Application of Thermoanalytical Techniques to Reaction Kinetics: The Thermogravimetric Evaluation of the Kinetics of the Decomposition of Calcium Oxalate Monohydrate. *The Journal of Physical Chemistry* **1958**, *62*, 394-397.
- [118] Zsako, J., Kinetic Analysis of Thermogravimetric Data. *The Journal of Physical Chemistry* **1968**, *72*, 2406-2411.
- [119] Kim, S.; Mundra, M. K.; Roth, C. B.; Torkelson, J. M., Suppression of the Tg-Nanoconfinement Effect in Thin Poly(Vinyl Acetate) Films by Sorbed Water. *Macromolecules* **2010**, *43*, 5158-5161.
- [120] Kim, S.; Roth, C. B.; Torkelson, J. M., Effect of Nanoscale Confinement on the Glass Transition Temperature of Free-Standing Polymer Films: Novel, Self-Referencing Fluorescence Method. *Journal of Polymer Science Part B: Polymer Physics* **2008**, *46*, 2754-2764.
- [121] Riedo, E.; Lévy, F.; Brune, H., Kinetics of Capillary Condensation in Nanoscopic Sliding Friction. *Physical Review Letters* **2002**, *88*, 185505.
- [122] Shaw, T.; Trolier-McKinstry, S.; McIntyre, P., The Properties of Ferroelectric Films at Small Dimensions. *Annual review of materials science* **2000**, *30*, 263-298.
- [123] Li, S.; Eastman, J. A.; Li, Z.; Foster, C. M.; Newnham, R. E.; Cross, L. E., Size Effects in Nanostructured Ferroelectrics. *Physics Letters A* **1996**, *212*, 341-346.
- [124] Burroughes, J.; Bradley, D.; Brown, A.; Marks, R.; Mackay, K.; Friend, R.; Burns, P.; Holmes, A., Light-Emitting Diodes Based on Conjugated Polymers. *Nature* **1990**, *347*, 539-541.
- [125] Olver, F. W. J., Uniform, Exponentially Improved, Asymptotic Expansions for the Generalized Exponential Integral. *SIAM Journal on Mathematical Analysis* **1991**, *22*, 1460-1474.
- [126] Senum, G. I.; Yang, R. T., Rational Approximations of the Integral of the Arrhenius Function. *Journal of Thermal Analysis* **1977**, *11*, 445-447.

- [127] Cacialli, F.; Riehn, R.; Downes, A.; Latini, G.; Charas, A.; Morgado, J., Fabrication of Conjugated Polymers Nanostructures Via Direct near-Field Optical Lithography. *Ultramicroscopy* **2004**, *100*, 449-455.
- [128] Pelletier, M. J., Quantitative Analysis Using Raman Spectrometry. *Applied Spectroscopy* **2003**, *57*, 20A-42A.
- [129] Rickard, D.; Giordani, S.; Blau, W. J.; Coleman, J. N., Quantifying the Contributions of Inner-Filter, Re-Absorption and Aggregation Effects in the Photoluminescence of High-Concentration Conjugated Polymer Solutions. *Journal of Luminescence* **2008**, *128*, 31-40.
- [130] Schermelleh, L.; Heintzmann, R.; Leonhardt, H., A Guide to Super-Resolution Fluorescence Microscopy. *The Journal of Cell Biology* **2010**, *190*, 165-175.
- [131] Gell, C.; Berndt, M.; Enderlein, J.; Diez, S., TIRF Microscopy Evanescent Field Calibration Using Tilted Fluorescent Microtubules. *Journal of Microscopy* **2009**, *234*, 38-46.
- [132] Wéry, J.; Dulieu, B.; Baïtoul, M.; Paniez, P.; Froyer, G.; Lefrant, S., Thermal Conversion of Ppv Precursor: Characterization at Different Stages of the Process. *Synthetic Metals* **1999**, *101*, 194-195.
- [133] Fang, S. J.; Haplepete, S.; Chen, W.; Helms, C. R.; Edwards, H., Analyzing Atomic Force Microscopy Images Using Spectral Methods. *J. Appl. Phys.* **1997**, *82*, 5891-5898.
- [134] Li, G.; Xi, N.; Yu, M.; Fung, W. K. In *3d Nanomanipulation Using Atomic Force Microscopy*, Robotics and Automation, 2003. Proceedings. ICRA '03. IEEE International Conference on, 14-19 Sept. 2003; 2003; pp 3642-3647 vol.3.
- [135] Huang, B.; Bates, M.; Zhuang, X., Super Resolution Fluorescence Microscopy. *Annual review of biochemistry* **2009**, *78*, 993.
- [136] Hell, S., Increasing the Resolution of Far-Field Fluorescence Light Microscopy by Point-Spread-Function Engineering. *Topics in fluorescence spectroscopy* **2002**, 361-426.
- [137] Glassbrenner, C. J.; Slack, G. A., Thermal Conductivity of Silicon and Germanium from 3°K to the Melting Point. *Physical Review* **1964**, *134*, A1058-A1069.
- [138] Tran, H.; Killops, K. L.; Campos, L. M., Advancements and Challenges of Patterning Biomolecules with Sub-50 Nm Features. *Soft Matter* **2013**, *9*, 6578-6586.

- [139] Minne, S. C.; Yaralioglu, G.; Manalis, S. R.; Adams, J. D.; Zesch, J.; Atalar, A.; Quate, C. F., Automated Parallel High-Speed Atomic Force Microscopy. *Appl. Phys. Lett.* **1998**, *72*, 2340-2342.
- [140] Barrettino, D.; Hafizovic, S.; Volden, T.; Sedivy, J.; Kirstein, K. U.; Hierlemann, A., Cmos Monolithic Mechatronic Microsystem for Surface Imaging and Force Response Studies. *Solid-State Circuits, IEEE Journal of* **2005**, *40*, 951-959.
- [141] Sulchek, T.; Grow, R. J.; Yaralioglu, G. G.; Minne, S. C.; Quate, C. F.; Manalis, S. R.; Kiraz, A.; Aydine, A.; Atalar, A., Parallel Atomic Force Microscopy with Optical Interferometric Detection. *Appl. Phys. Lett.* **2001**, *78*, 1787-1789.
- [142] Hafizovic, S.; Barrettino, D.; Volden, T.; Sedivy, J.; Kirstein, K.-U.; Brand, O.; Hierlemann, A., Single-Chip Mechatronic Microsystem for Surface Imaging and Force Response Studies. *Proceedings of the National Academy of Sciences of the United States of America* **2004**, *101*, 17011-17015.
- [143] Minne, S. C.; Adams, J. D.; Yaralioglu, G.; Manalis, S. R.; Atalar, A.; Quate, C. F., Centimeter Scale Atomic Force Microscope Imaging and Lithography. *Appl. Phys. Lett.* **1998**, *73*, 1742-1744.
- [144] Bullen, D.; Xuefeng, W.; Zou, J.; Seunghun, H.; Chung, S.-W.; Ryu, K.; Zhifang, F.; Mirkin, C.; Chang, L. In *Micromachined Arrayed Dip Pen Nanolithography Probes for Sub-100 Nm Direct Chemistry Patterning*, Micro Electro Mechanical Systems, 2003. MEMS-03 Kyoto. IEEE The Sixteenth Annual International Conference on, 19-23 Jan. 2003; 2003; pp 4-7.
- [145] Kim, H. J.; Dai, Z.; King, W. P., Thermal Crosstalk in Heated Microcantilever Arrays. *Journal of Micromechanics and Microengineering* **2013**, *23*, 025001.
- [146] King, W. P.; Kenny, T. W.; Goodson, K. E.; Cross, G. L. W.; Despont, M.; Durig, U. T.; Rothuizen, H.; Binnig, G.; Vettiger, P., Design of Atomic Force Microscope Cantilevers for Combined Thermomechanical Writing and Thermal Reading in Array Operation. *Microelectromechanical Systems, Journal of* **2002**, *11*, 765-774.
- [147] Cappella, B.; Dietler, G., Force-Distance Curves by Atomic Force Microscopy. *Surface Science Reports* **1999**, *34*, 1-104.
- [148] Kovalev, A.; Shulha, H.; Lemieux, M.; Myshkin, N.; Tsukruk, V. V., Nanomechanical Probing of Layered Nanoscale Polymer Films with Atomic Force Microscopy. *Journal of Materials Research* **2004**, *19*, 716-728.
- [149] Somnath, S.; King, W. P., Heated Atomic Force Cantilever Closed Loop Temperature Control and Application to High Speed Nanotopography Imaging. *Sens. Actuators, A* **2013**, *192*, 27-33.

- [150] Paul, P.; Knoll, A. W.; Holzner, F.; Duerig, U., Field Stitching in Thermal Probe Lithography by Means of Surface Roughness Correlation. *Nanotechnol.* **2012**, *23*, 385307.
- [151] Holzner, F.; Kuemin, C.; Paul, P.; Hedrick, J. L.; Wolf, H.; Spencer, N. D.; Duerig, U.; Knoll, A. W., Directed Placement of Gold Nanorods Using a Removable Template for Guided Assembly. *Nano Lett.* **2011**, *11*, 3957-3962.
- [152] Fryer, D. S.; Nealey, P. F.; de Pablo, J. J., Thermal Probe Measurements of the Glass Transition Temperature for Ultrathin Polymer Films as a Function of Thickness. *Macromolecules* **2000**, *33*, 6439-6447.
- [153] Lee, J.; King, W. P., Liquid Operation of Silicon Microcantilever Heaters. *Sensors Journal, IEEE* **2008**, *8*, 1805-1806.
- [154] Zhang, K.; Fu, Q.; Pan, N.; Yu, X.; Liu, J.; Luo, Y.; Wang, X.; Yang, J.; Hou, J., Direct Writing of Electronic Devices on Graphene Oxide by Catalytic Scanning Probe Lithography. *Nat Commun* **2012**, *3*.
- [155] Liu, M.; Amro, N. A.; Liu, G.-y., Nanografting for Surface Physical Chemistry. *Annu. Rev. Phys. Chem.* **2008**, *59*, 367-386.
- [156] Rosa, L. G.; Liang, J., Atomic Force Microscope Nanolithography: Dip-Pen, Nanoshaving, Nanografting, Tapping Mode, Electrochemical and Thermal Nanolithography. *J. Phys.: Condens. Matter* **2009**, *21*, 483001.
- [157] Suda, H.; Yamada, S., Force Measurements for the Movement of a Water Drop on a Surface with a Surface Tension Gradient. *Langmuir* **2002**, *19*, 529-531.
- [158] Smith, J. T.; Tomfohr, J. K.; Wells, M. C.; Beebe, T. P.; Kepler, T. B.; Reichert, W. M., Measurement of Cell Migration on Surface-Bound Fibronectin Gradients. *Langmuir* **2004**, *20*, 8279-8286.
- [159] Smith, J. T.; Elkin, J. T.; Reichert, W. M., Directed Cell Migration on Fibronectin Gradients: Effect of Gradient Slope. *Experimental Cell Research* **2006**, *312*, 2424-2432.
- [160] Wu, T.; Efimenko, K.; Genzer, J., Combinatorial Study of the Mushroom-to-Brush Crossover in Surface Anchored Polyacrylamide. *J. Am. Chem. Soc.* **2002**, *124*, 9394-9395.
- [161] Moh, L. C. H.; Losego, M. D.; Braun, P. V., Solvent Quality Effects on Scaling Behavior of Poly(Methyl Methacrylate) Brushes in the Moderate- and High-Density Regimes. *Langmuir* **2011**, *27*, 3698-3702.
- [162] Vlasov, Y. A.; Bo, X.-Z.; Sturm, J. C.; Norris, D. J., On-Chip Natural Assembly of Silicon Photonic Bandgap Crystals. *Nature* **2001**, *414*, 289-293.

- [163] Lee, I.; Zheng, H.; Rubner, M. F.; Hammond, P. T., Controlled Cluster Size in Patterned Particle Arrays Via Directed Adsorption on Confined Surfaces. *Adv. Mater.* **2002**, *14*, 572-577.
- [164] Dziomkina, N. V.; Vancso, G. J., Colloidal Crystal Assembly on Topologically Patterned Templates. *Soft Matter* **2005**, *1*, 265-279.
- [165] Varghese, B.; Cheong, F. C.; Sindhu, S.; Yu, T.; Lim, C.-T.; Valiyaveetil, S.; Sow, C.-H., Size Selective Assembly of Colloidal Particles on a Template by Directed Self-Assembly Technique. *Langmuir* **2006**, *22*, 8248-8252.
- [166] Zhang, C.; Macfarlane, R. J.; Young, K. L.; Choi, C. H. J.; Hao, L.; Auyeung, E.; Liu, G.; Zhou, X.; Mirkin, C. A., A General Approach to DNA-Programmable Atom Equivalents. *Nat Mater* **2013**, *12*, 741-746.
- [167] Wang, Y.; Wang, Y.; Breed, D. R.; Manoharan, V. N.; Feng, L.; Hollingsworth, A. D.; Weck, M.; Pine, D. J., Colloids with Valence and Specific Directional Bonding. *Nature* **2012**, *491*, 51-55.
- [168] Schoch, R. B.; Han, J.; Renaud, P., Transport Phenomena in Nanofluidics. *Reviews of Modern Physics* **2008**, *80*, 839-883.
- [169] Abgrall, P.; Nguyen, N. T., Nanofluidic Devices and Their Applications. *Anal. Chem.* **2008**, *80*, 2326-2341.
- [170] Weber, H. J.; Harris, F. E.; Arfken, G. B., *Essential Mathematical Methods for Physicists, Ise*. Access Online via Elsevier: 2003.